Dissertation

submitted to the

Combined Faculty of Natural Sciences and Mathematics

of Heidelberg University, Germany

for the degree of

Doctor of Natural Sciences

Put forward by

Maximilian Schmidt

born in: Darmstadt

Oral examination: 17.11.2021

ii

Investigations of Lake Kivu with

^{39}Ar Atom Trap Trace Analysis

Referees: Prof. Werner Aeschbach

              Prof. André Butz

Zusammenfassung

^{39}*Ar Atom Trap Trace Analysis* (ATTA – dt.: Argon^{39} Atomfallen-Spurenstoffanalyse) ist eine neuartige Datierungsmethode mit Anwendungen in den Umweltwissenschaften. Mit einer Halbwertszeit von 269 Jahren und einem möglichen Datierungszeitraum zwischen 50 und 1000 Jahren schließt ^{39}Ar eine Lücke im Spekrum der zuvor vorhandenen Datierungsmethoden. In dieser Arbeit wird die erste Anwendung von ^{39}Ar ATTA an einem See-System, dem Kivu See in Ruanda, sowie eine aufwändige Analysemethode unter Anwendung einer 1D Simulation vorgestellt. Mit Hilfe von ^{39}Ar ATTA konnten extreme Konzentration von ^{39}Ar in einigen stark lokalisierten Wasserschichten im Kivu See gefunden werden. Durch die 1D Simulationsanalyse konnten diese hohen Konzentrationen auf Grundwasserzuflüsse zurückgeführt werden, welche wiederum die höchsten ^{39}Ar Konzentrationen aufweisen, die bisher beschrieben wurden. Weiterhin werden verschiedene methodische Verbesserungen vorgestellt, welche nötig waren, um diese ^{39}Ar ATTA Studie am Kivu See durchzuführen.

Des Weiteren werden in dieser Arbeit Möglichkeiten untersucht und vorgestellt, die Anwendbarkeit eines *total dissolved gas sensors* (TDG – dt.: Sensor für den Gesamtgasdruck gelöster Gase) zu erweitern, um neben dem Gesamtgasdruck im Kivu See auch die Partialdrücke der verschiedenen Gaskomponenten messen zu können. Dafür wird ein experimenteller Aufbau zur Simulation ähnlicher Bedingungen zum Kivu See im Labor beschrieben. Messdaten dieses Experiments zeigen die Komplexität des gekoppelten Systems aus gelöstem CO_2 und Methan, Wasser und einer PTFE Membran. Ebenso wird eine Methode zur Ableitung von Partialdrücken aus dem TDG Datensatz vom Kivu See präsentiert.

Schließlich zeigt eine kurze Zusammenfassung zusätzlich durchgeführter ^{39}Ar ATTA Messungen von Proben aus verschiedenen Umweltsystemen die Vielseitigkeit der ^{39}Ar Datierung mit ATTA.

Abstract

[39]Ar Atom Trap Trace Analysis (ATTA) is a new dating method for the environmental sciences. With its half-life of 269 years and a dating range of 50 to 1000 years, it closes a gap in the set of the previously available dating methods. This thesis provides the first application of [39]Ar ATTA on a lake system, i.e. Lake Kivu in Rwanda, including an elaborate data analysis routine using a 1D simulation tool. With [39]Ar ATTA, extreme concentrations of [39]Ar were found in some distinctly localised water layers in Lake Kivu and using the 1D simulation analysis, this effect could be traced to groundwater inflow springs featuring the highest [39]Ar concentrations described so far. Several methodological improvements are presented as well which were necessary to achieve feasibility for this [39]Ar ATTA study on Lake Kivu.

Additionally, the potential of a total dissolved gas sensor (TDG) is explored with the aim of expanding its capabilities to measure the dissolved gasses in Lake Kivu and their partial pressures. An experimental setup to this end that simulates a pressure environment comparable to Lake Kivu is presented. Data from this experiment show the complexity of the coupled system of dissolved CH_4 and CO_2, water and a PTFE membrane. Moreover, a method to achieve a good partial pressure resolution from the TDG measurements of Lake Kivu is presented.

Finally, a brief summary of the application of [39]Ar ATTA on several environmental systems further demonstrates the versatility of [39]Ar dating with ATTA for different environmental research contexts.

TABLE OF CONTENTS

1. Introduction

1.1. The dating problem in hydrology

Hydrologic systems are all around us and affect our everyday life in many different ways. Everything that flows, everything that can be described as a fluid continuum can be assessed by the principles of fluid dynamics, be it e.g. large scale ocean circulations such as the Gulf Stream (Kwon et al. 2010; Oey et al. 2013), microscopic cellular membrane mechanisms (Um et al. 2000) or catchment scale assessments of precipitation and flooding (Apel et al. 2004).

Although the concept is applicable to a multitude of systems, this introduction will focus on water fluxes through various environmental systems. These environmental systems can vary a lot regarding scales of time and space. Figure 1 provides an overview of relevant timescales for freshwater systems and thus, provides an impression of the complexity in trying to simulate a large hydrologic system (Sprenger et al. 2019).
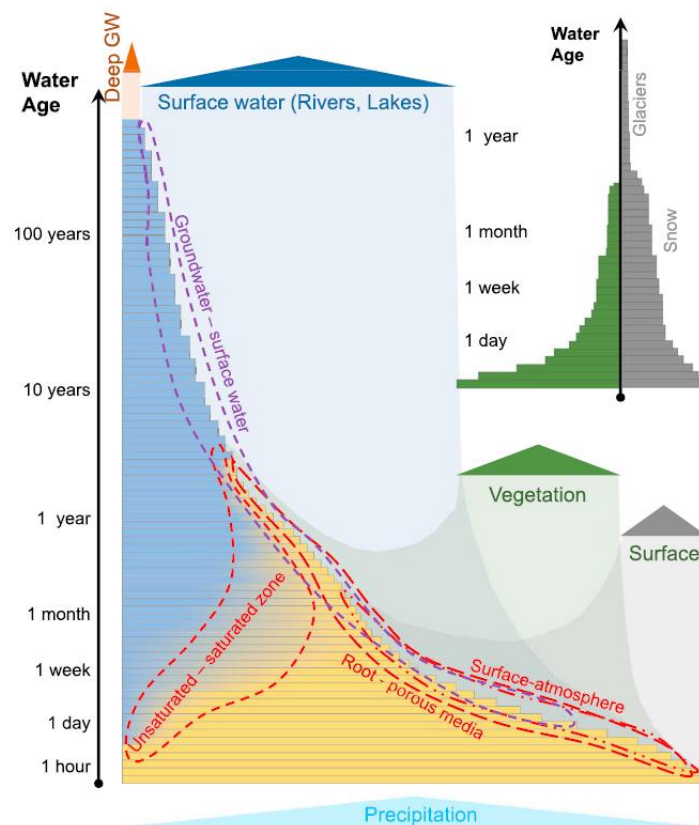
Figure 1: Age distribution and localization of the earth's freshwater. Similar to the age structures of human societies, this type of figure presents the demographics of water. Figure from (Sprenger et al. 2019), a review to which contributions were made during this project.

Many different concepts were developed to calculate the flow through a system and to connect observable properties of the system to its dynamics. One of these concepts

is the Transit Time Distribution (TTD), a very powerful concept that will be introduced in the following.

Figure 2 shows two highly simplified flow models which are often used, e.g. in analyzing dynamics of groundwater formation and flow. Figure 2 a) shows the piston flow model. Here, the flow of a fluid parcel is modelled analogous to the flow through a pipe. The time for the input to reach the output is simply a function of the conductivity of the medium and the difference in potential energy. This transit time of the fluid is often referred to as the age (mean age: $\bar{\alpha}$). The piston flow model can be used to simulate the flow of groundwater through a confined aquifer. Figure 2 b) shows the exponential flow model. Here, a constant input flows through a continuous and uniform medium into a mixed reservoir. The shape of the age distribution follows an exponential function $\propto \exp(-\alpha/\bar{\alpha})$. The exponential flow model can be applied to e.g. non-confined aquifers or surface run-off accumulating into a river.

In both cases, the age of the outflow follows a distribution. This distribution can be referred to as the transit time distribution (TTD).
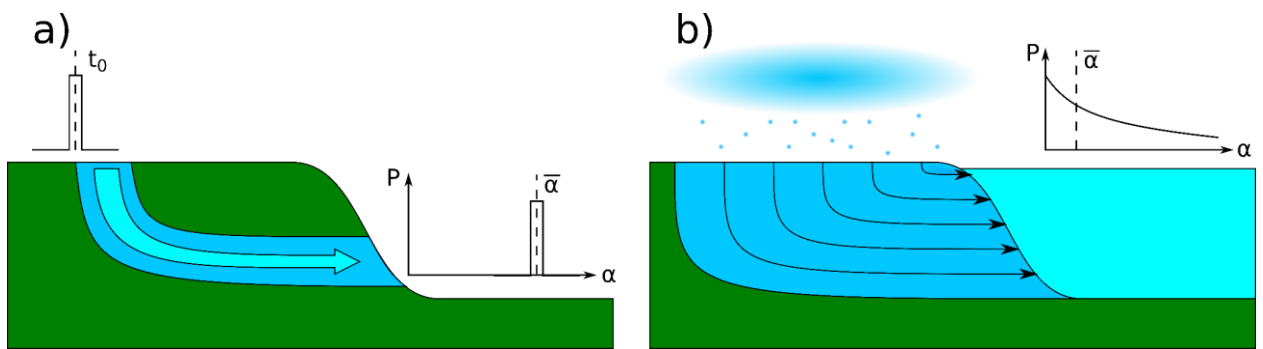
Figure 2: Two simple models describing the flow through a system and the age (α) distribution P(α) of its output. a) Piston flow model. A water parcel with a Dirac-δ-like input at $t_0 = 0$ exits after the time α. b) Exponential flow model. A continuous input flows through a continuous uniform medium and accumulates into a mixed reservoir. The age distribution P(α) of the water in the reservoir follows an exponential shape.

In reality, environmental systems are far more complicated and another way to infer the hydrological properties of such a system will be outlined in the following.

In general, one can describe the output j_{out} of a system S as a function of the operator $\mathcal{S}$ with the argument j_{in}. The following calculus is mainly based on (Roth 2016).

$$j_{out} = \mathcal{S}(j_{in}) \qquad \text{Equation 1}$$

Let S be a linear and stationary system with:

$$K \cdot j_{out} = \mathcal{S}(K \cdot j_{in}) \text{ and } j_{out}(t - t_0) = \mathcal{S}(j_{in}(t - t_0)) \qquad \text{Equation 2}$$

When looking at the flow through a system, there are two different perspectives that can be taken (see Figure 3). From the input perspective, a water parcel is considered at an entry point into a system and its development over time is looked at. The mathematical description of this perspective is the one of the point spread function corresponding to the response function of the system on a Dirac-δ input:

$$p_t(t, l) = \mathcal{S}(\delta(t))$$ Equation 3

Where $p_t(t, l)$ is the probability density function of the water parcel exiting at an outflow point at position l after the infinitesimal water parcel (δ) has passed the system S. When decomposing the input function in Dirac-δ functions and inserting into Equation 1, one gets:

$$j_{in}(t, l = 0) = \int j_{in}(\tau, 0)\delta(t - \tau)d\tau$$

$$j_{out}(t, l) = \mathcal{S}(j_{in}) = \mathcal{S}\left(\int j_{in}(\tau, 0)\delta(t - \tau)d\tau\right)$$ Equation 4

$$= \int j_{in}(\tau, 0)\mathcal{S}(\delta(t - \tau))d\tau$$

And hence:

$$j_{out}(t, l) = \int j_{in}(\tau, 0)p_t(t - \tau, l)d\tau$$ Equation 5

In a system with a known point spread function p_t, Equation 5 can be used to determine any output from any input. Hence knowing the point spread function is equivalent to knowing all properties of system S.

For the examples shown in Figure 2, the point spread functions are very simple and given by:

Piston Flow: $j_{out}(t, l) = \int j_{in}(\tau, 0)\delta(\tau - \bar{\alpha}, l)d\tau$

Exponential Flow: $j_{out}(t, l) = \int j_{in}(\tau, 0) \frac{1}{\bar{\alpha}}\exp(-\tau/\bar{\alpha})d\tau$ Equation 6

Both with the parameter $\bar{\alpha}$ being the mean age.

Looking at the output of a system is the other perspective depicted in Figure 3 b). Naturally, this is the point of view most often employed when investigating a sample taken from an environmental system. The age of the sample results from the previous trajectories of the individual particles and is described by the TTD which directly follows from the description of the outflow $j_{out}(t, l)$ in Equation 5.
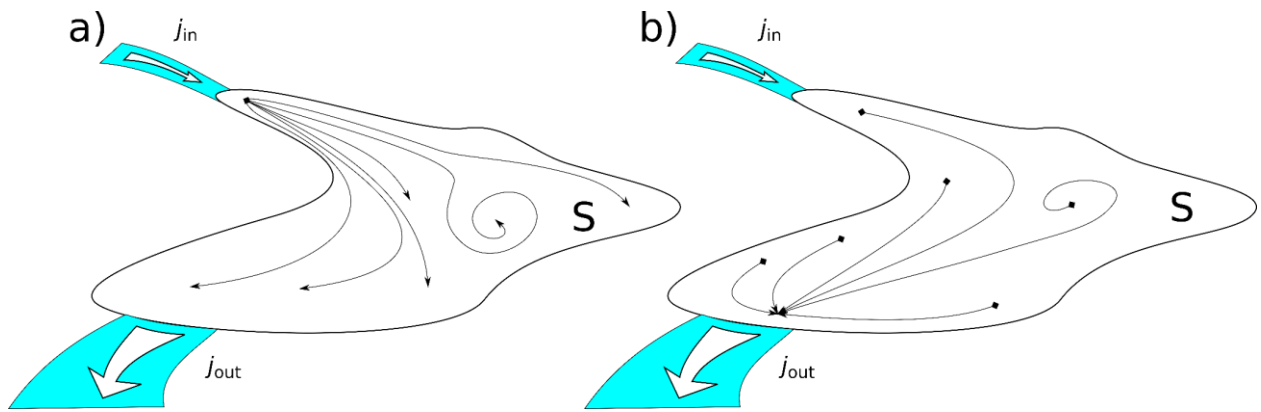
Figure 3: Perspectives on flow j through the system S: a) Inflow perspective. Looking at a water parcel upon entering the system and its development over time. Equivalent to this view is the point spread function of the system S, as also shown in Figure 2a). b) Outflow perspective. Looking at a water parcel e.g. at a sampling point or at a natural outflow and considering all trajectories of particles and their properties towards this point. The age distribution of a sample is usually described from this perspective, as also shown in Figure 2 b).

Consequently, the TTD is a direct result of the input coupled with the point spread function and is, thus, a way to describe the system S. Inferring the TTD from measurement data is therefore the aim of many studies investigating complex hydrological systems. In chapter 4.6.4 in this work, an attempt to determine a TTD for Lake Kivu will be presented.

One experimental approach to determine a TTD is dating water samples, i.e. determining the concentrations of certain tracers carrying an intrinsic age information to determine the samples' age. Several dating tracers are presented in chapter 1.2. When investigating the age of a sample with a dating tracer, a tracer or apparent age is inferred from the data, rather than a distribution of ages. The tracer/apparent age corresponds to the age $\bar{\alpha}$ resulting from the piston flow model. If the system is more complex, the tracer age usually deviates from the mean age in the model. But the measured tracer concentration can be used in combination with the system output concentration determined using different models in order to determine the TTD (see chapter 1.3).

For highly simplified models like the piston flow or the exponential model described above (Figure 2 and Equation 6), only one parameter (here: $\bar{\alpha}$) is necessary and thus, a single tracer would suffice. For more complicated point spread functions, every free parameter essentially requires the measurement of one more dating tracer. In an ocean ventilation study performed in our group in 2018 (Ebser et al. 2018b), for example, two dating tracers (CFC-12 and ^{39}Ar) were used to determine the two free parameters $\bar{\alpha}$ and δ of the point spread function, which was modelled by an advective dispersive model[1]:

$$p_t(t, \bar{\alpha}) = \sqrt{\frac{\bar{\alpha}}{4\pi\delta t^3}} \exp\left(-\frac{(t-\bar{\alpha})^2}{4\delta\bar{\alpha}t}\right)$$

Equation 7

In some cases, parameterized functions as point spread functions are simplifications that might be not sufficient to describe a system. An alternative approach would be the use of nonparametric models as shown, for example, in (Rädle et al. 2021). Those approaches work best with a multitude of dating tracers. The work of Viola Rädle, which this PhD project contributed to, will be presented briefly in chapter 6.3 as well.

---

[1] The advective dispersive model is (mainly in oceanography and also in Ebser et al. 2018b) also called inverse Gaussian function. A reparametrization with Δ describing the dispersivity and Γ describing the mean age one gets:

$$p_t(t) = \sqrt{\frac{\Gamma^3}{4\pi\Delta^2 t^3}} \exp\left(\frac{-\Gamma(t-\Gamma)^2}{4\Delta^2 t}\right)$$

1.2. Dating tracers
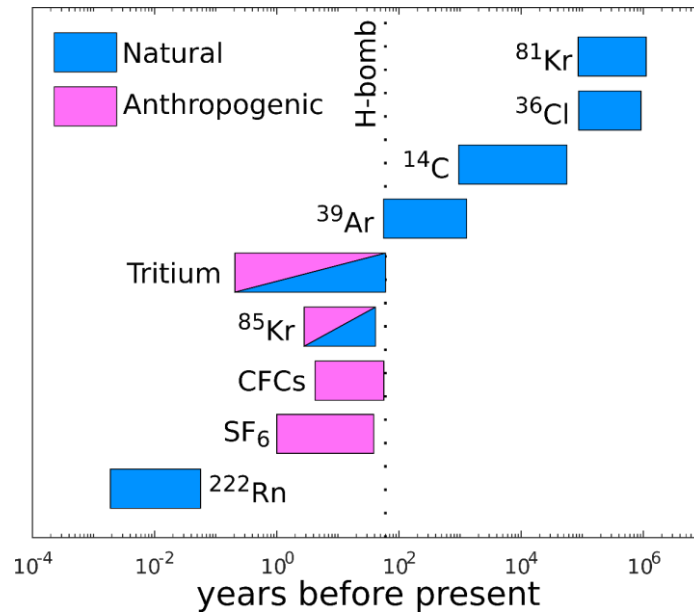
Figure 4: Selection of hydrospheric dating tracers used in environmental sciences with their respective dating ranges. One can distinguish between naturally occurring and anthropogenic tracers. The displayed tracers are suitable for different dating ranges depending on their time dependent input function and/or their radioactive decay constants. Figure modified from (Welte 2011).

The environmental sciences utilize different approaches to determine the ages of water samples, of which the determination of concentrations of substances that carry intrinsic time information is a very powerful one. Those substances are called dating tracers. In Figure 4, some dating tracers for application in the hydrosphere are listed. Regarding hydrospheric dating tracers, the age of a water parcel is mostly defined as the time for which this parcel has been isolated from the atmosphere, e.g. through freezing or entering the saturated zone in groundwater formation. The principle behind all of these methods is similar: A water parcel in equilibrium with the atmosphere carries the atmospheric gasses as solutes with their solute concentrations proportional to their partial pressure in the atmosphere (see below Henry's law Equation 10). An isolation event then stops this equilibration for some time. At sampling, the water parcel contains the tracers in concentrations dependent on their atmospheric concentration at the time of isolation. Additionally, in the case of radioactive tracers, the concentration has diminished according to its radioactive decay constant. Thus, there are mainly two different cases to discuss. For stable tracers (like SF_6 or chlorofluorocarbons(CFCs)), one can calculate the tracer's atmospheric concentration at the time of the water parcel's isolation. This atmospheric concentration, called input function, can be time dependent. If the input function is known well enough, one can directly derive the time of isolation, hence the age of the water parcel. The other main case concerns radioactive tracers with quasi constant input functions (as e.g. ^{39}Ar). Here, the concentration at equilibration is constant over time, but the age information can be obtained by calculating the concentration at sampling using the specific radioactive decay law. Radioactive tracers often do not

6

have a constant input function, so their use in water parcel dating requires a combination of the two aforementioned methods.

The dating range of each tracer is dependent on different factors. For tracers with a time-variable input function (the so called transient tracers), the dating range is limited to time periods with a changing atmospheric tracer concentration. Therefore, the use of tracers like SF_6 and CFCs is limited to time periods after the 1960s, when their industrial use and, hence, their atmospheric concentration increased. For tracers with a radioactive decay and a constant input function, the dating range is mainly defined by their respective decay constant. Concentration changes are very small for very young samples and measurable concentrations can be very low for very old samples. Hence, as a rule of thumb, a radioactive dating tracer is normally suitable for samples of an age > ¼ x $T_½$ and < 4 x $T_½$. This range can be extended by increasing measurement precision.

1.3. The apparent age problem

The non-linearity of the decay of radioactive dating tracers leads to a phenomenon called apparent age. It is best explained with a simple example: given two equally sized water bodies containing ^{39}Ar and ^{14}C. The water bodies are of the ages 0 years and 1000 years and are mixed together, thus having a mean age of $\bar{\alpha} = 500$ years. For the concentrations of the radioactive tracers in the mixture one gets:

$$\frac{\left[^{14}C\right]_{Mix}}{\left[^{14}C\right]_0} = \frac{1}{2} \cdot \left(\underbrace{\frac{\left[^{14}C\right]_0}{\left[^{14}C\right]_0}}_{=1} + \frac{\left[^{14}C\right]_{1000}}{\left[^{14}C\right]_0} \right) = \frac{1}{2} \cdot \left(1 + \exp\left(-\frac{1000\ y}{8270\ y} \right) \right)$$
$$= 0.943$$

$$\tau_{14C} = \frac{T_{1/2\ 14C}}{\ln(2)} = 8270\ y$$

$$\frac{\left[^{39}Ar\right]_{Mix}}{\left[^{39}Ar\right]_0} = \frac{1}{2} \cdot \left(\underbrace{\frac{\left[^{39}Ar\right]_0}{\left[^{39}Ar\right]_0}}_{=1} + \frac{\left[^{39}Ar\right]_{1000}}{\left[^{39}Ar\right]_0} \right) = \frac{1}{2} \cdot \left(1 + \exp\left(-\frac{1000\ y}{388\ y} \right) \right)$$
$$= 0.538$$

$$\tau_{39Ar} = \frac{T_{1/2\ 39Ar}}{\ln(2)} = 388\ y$$

When know calculating the age of the mixture straight from the isotope concentrations one gets the apparent age $\tilde{\alpha}$:

$$\tilde{\alpha}_{14C} = -\tau_{14C} \cdot \ln(0.943) = 485\ y$$

$$\tilde{\alpha}_{39Ar} = -\tau_{39Ar} \cdot \ln(0.538) = 241 \; y$$

The apparent age deviates more for the ^{39}Ar measurement, than for the ^{14}C measurement. This is, because the mean age in this example is much lower than the half-life of ^{14}C, thus the decay curve is still quite linear in this regime. For ^{39}Ar, the apparent age deviates extremely from the actual mean age. When looking at Equation 8 and Equation 9, one can infer, that in this case the apparent age has an upper boundary, the half-life T½[2]. In general, mixtures are described by the aforementioned TTDs. Figure 5 gives an overview the apparent age of a mixture and its dependency on the shape of the TTD and the mean age. Figure 5 a) shows an exponential TTD, comparable to Figure 2 b). Figure 5 b) shows a homogeneous age distribution, which is equivalent to the binary mixture discussed above[3]. Figure 5 c) shows the TTD of an advective/dispersive transport with the additional dimensionless parameter δ describing the diffusivity and here set to δ = 100. Figure 5 d) sums up the relation of the apparent age $\tilde{\alpha}$ and the mean age $\bar{\alpha}$. The apparent age of both the exponential and the homogenous model are limited by T½, as they both for $\bar{\alpha} \to \infty$ converge to a homogeneous distribution. The dispersive model does not lead to a limited apparent age. For all calculations and formulas for the TTDs, see Appendix 8.1.

---

[2] For a binary mixture of two equally large contributions of the ages 0 and ∞, the concentration of the mixture is C_{mix}/C_0 = ½. Due to the convex shape of the exponential function, the apparent age is always smaller (or equal for $p_t = \delta(t-\alpha)$), than the real age.

[3] The TTD of a homogeneous function is a step function, for the equal binary mixture a double δ function. For a comparison see Appendix 8.1.3.
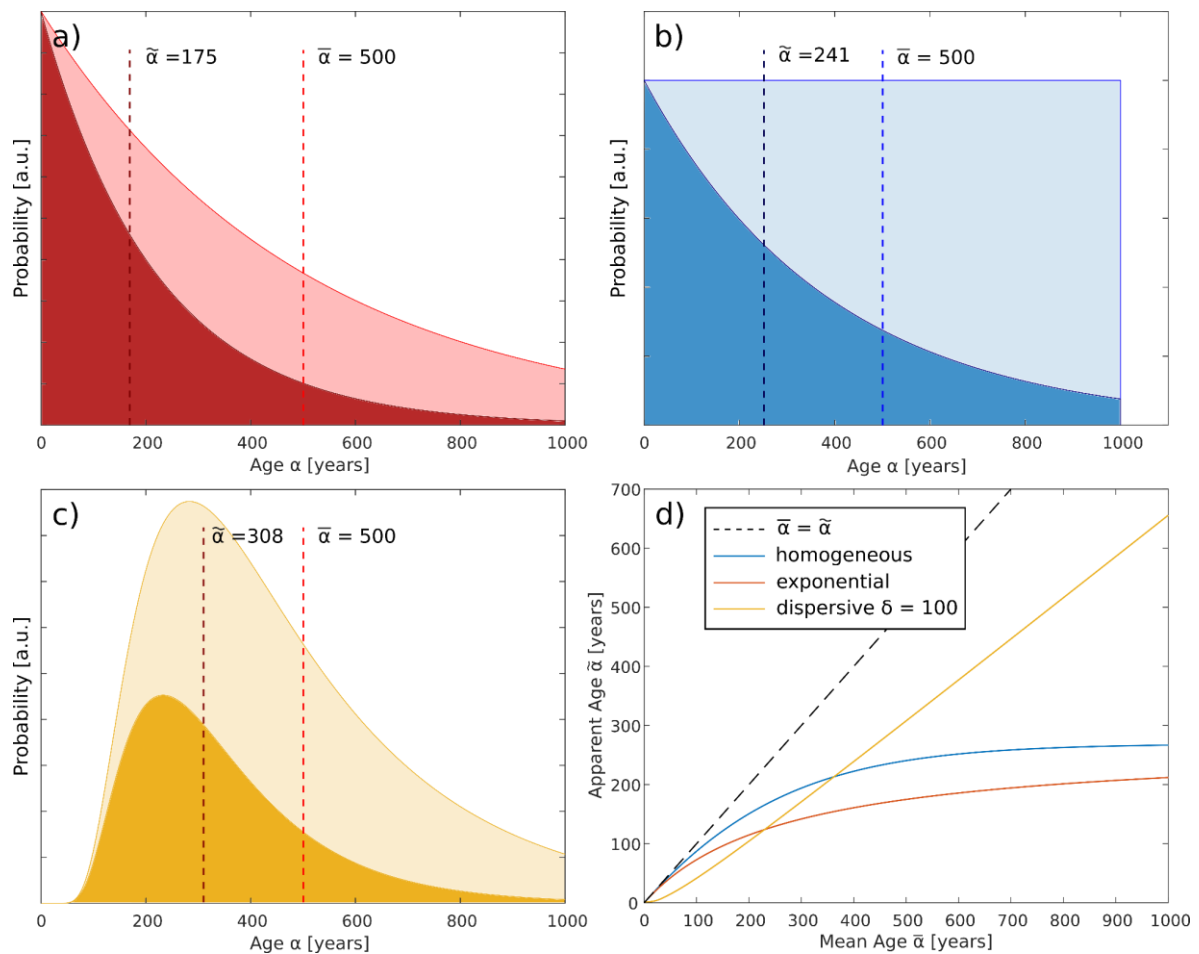
Figure 5: Different TTDs showing the relation between mean age $\bar{\alpha}$ and apparent mean age $\tilde{\alpha}$ for different age distributions. a) Exponential distribution (compare Figure 2 b) and Equation 6) b) Homogeneous distribution c) Advective dispersive model $\delta = 100$. a), b) & c): light color: The age distribution with a mean age of 500 years. Dark color: the same distribution now including a radioactive decay with $T\frac{1}{2} = 269$ years leading to a different apparent age. d)) Dependence of the apparent age $\tilde{\alpha}$ from the mean age $\bar{\alpha}$ and the shape of the age distribution. For calculations see Appendix 8.1.

To yield the real age from the apparent age, the TTD needs to be known. As the exponential model only carries one free parameter, one tracer measurement suffices. For more complicated TTDs like e.g. the advective/dispersive model, a second aging tracer needs to be used to infer the free parameter δ.

In chapter 4.6.4 an age distribution for Lake Kivu will be calculated. This distribution is in units of apparent age and also cannot be transposed into mean ages, as the mixing processes in the lake cannot be parametrized.

1.4. The radioisotope ^{39}Ar

^{39}Argon is a radioactive isotope of the noble gas argon and the main tracer used in this work, which is why it will be introduced in more detail in the following.

	Relative atmospheric abundance	Half-life $T_{\frac{1}{2}}$	Decay constant λ
^{36}Ar	0.336 %	Stable	0
^{37}Ar	0 (synthetic)	35 d	7.2 year^{-1}
^{38}Ar	0.063 %	Stable	0
^{39}Ar	8.1x10^{-16}	269 years	0.0026 year^{-1}
^{40}Ar	99.6 %	Stable	0

Table 1: Atmospheric argon isotopes.

Atmospheric argon is dominated by its main isotope ^{40}Ar with an atmospheric abundance of 99.6 %. ^{40}Ar is the product of the decay of ^{40}K in the earth's crust and thus slowly accumulates in the atmosphere over time with a rate of about 1.27 x10^8 mol ^{40}Ar/year (Stuart et al. 2016) with a current total ^{40}Ar amount of 1.78 x10^{18} mol. Thus, [^{40}Ar] can be assumed as constant on timescales << 10^{10} years. Atmospheric ^{39}Ar is generated in the atmosphere by neutron spallation processes of ^{40}Ar: ^{40}Ar(n,2n)^{39}Ar. The required neutrons are a part of the air shower created by high energy cosmic radiation. With this constant generation and a half-life of 269 years, an equilibrium atmospheric abundance of [^{39}Ar/Ar] = 8.1 x10^{-16} (Loosli 1983) is reached. With this extremely low isotopic abundance, the number of ^{39}Ar atoms a water sample also is extremely small. According to Henry's law of solute concentrations (Equation 10), c_i is proportional to the gas' respective partial pressure p_i in the gas phase. H_i is called the Henry constant and describes the solubility of a gas in water.

$$c_i = p_i \cdot H_i$$

Equation 10

Table 2 gives an overview over the solubility of different atmospheric gasses and the expected amount of that gas in 1 L atmosphere equilibrated water.

Gas	Relative Atmospheric Abundance	H^{cp} $\left[\frac{mol}{m^3 \cdot Pa}\right]$ at 25°C	Gas amount in 1 L atmosphere equilibrated water
N_2	0.781	6.4 x10^{-6}	11.4 ml$_{STP}$
O_2	0.209	1.2 x10^{-5}	5.7 ml$_{STP}$
Ar	9.34 x10^{-3}	1.4 x10^{-5}	0.28 ml$_{STP}$
^{39}Ar	7.57 x10^{-18}	1.4 x10^{-5}	6800 atoms
CO_2	4.15 x10^{-4}	3.3 x10^{-4}	0.31 ml$_{STP}$
Ne	1.82 x10^{-5}	4.5 x10^{-6}	0.19 µl$_{STP}$
He	5.24 x10^{-6}	3.9 x10^{-6}	0.046 µl$_{STP}$
CH_4	1.87 x10^{-6}	1.4 x10^{-5}	0.060 µl$_{STP}$
Kr	1.14 x10^{-6}	2.5 x10^{-5}	0.065 µl$_{STP}$

Table 2: Atmospheric abundance, Henry coefficients and gas volume in 1 L atmosphere equilibrated water (Sander 2015; NASA 1976).

As an atmospheric noble gas radio-nuclide, ^{39}Ar offers several advantages compared to other tracers. Its constant input function makes age calculations much easier, compared to, e.g. ^{14}C, where the input function is significantly affected by the hydrogen-bomb tests in the 1950s and early 60s. Unlike e.g. ^{14}C and CFCs, ^{39}Ar as a noble gas is not affected by chemical and biochemical processes. With its relatively low mass difference compared to the main isotope ^{40}Ar, ^{39}Ar is also not significantly affected by isotopic fractionation effects.

Besides the atmospheric generation, a geogenic production process is also known, the neutron spallation of ^{39}K: ^{39}K(n,p$^+$)^{39}Ar (Andrews et al. 1989; Loosli et al. 1989; Šrámek et al. 2017). In bedrock with high neutron fluxes, this process can be so prevalent that groundwater samples from such areas can be highly enhanced in ^{39}Ar isotopic abundance (Yokochi et al. 2013). This increase in ^{39}Ar could also be utilized as a dating method with the knowledge of surrounding hydrogeological parameters, as has been suggested by (Yokochi et al. 2012). Figure 6 shows both ^{39}Ar generation pathways, as well as its β$^-$ decay both on nuclear and sub-nuclear level.
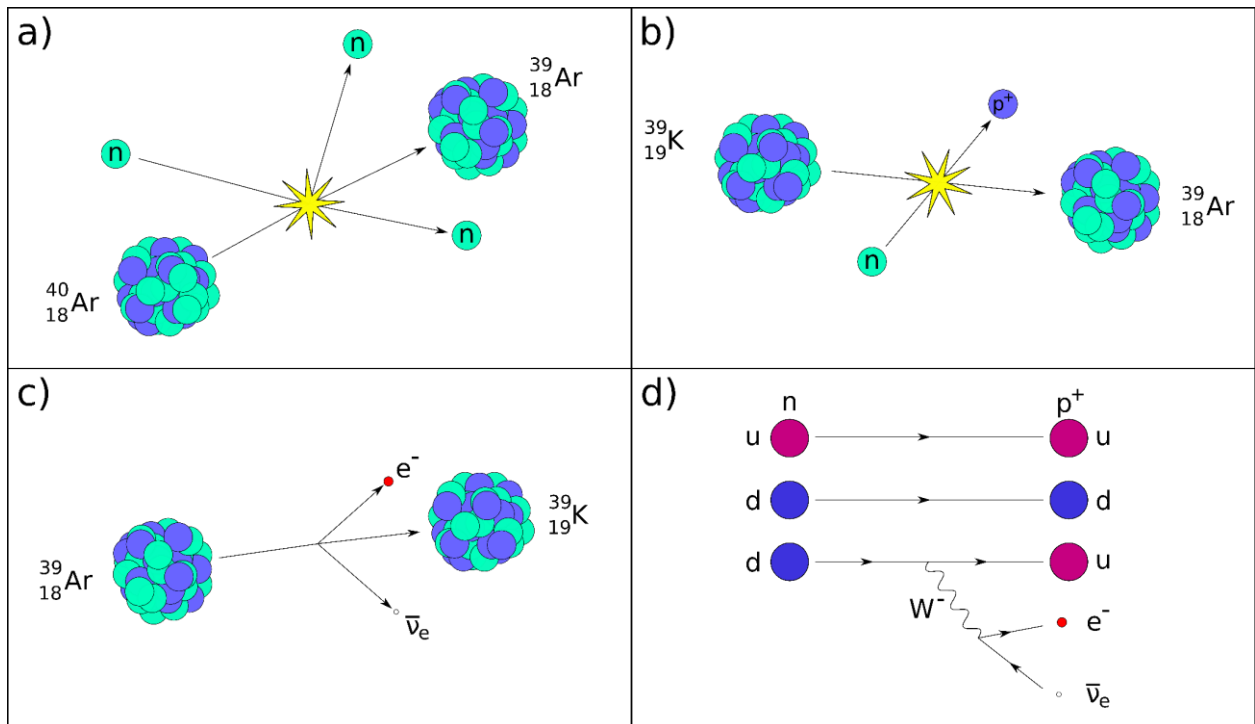
Figure 6: a) Atmospheric ^{39}Ar production due to neutron spallation of ^{40}Ar – ^{40}Ar(n,2n)^{39}Ar b) geogenic ^{39}Ar production due to neutron spallation of ^{39}K – ^{39}K(n,p$^+$)^{39}Ar c) β$^-$ decay of ^{39}Ar to ^{39}K d) Feynman diagram of the β$^-$ decay. The down-quark decays into an up-quark via the release of a W$^-$boson, which decays into an electron and an anti-electron-neutrino.

1.5. ^{39}Argon dating

With its half-life of 269 years, ^{39}Ar is suitable for dating environmental samples with ages between 50 and 1000 years (Loosli 1983). Very recent improvements in measurement precision extended this limit up to 1800 years (Jiang 7/5/2021). For

dating with this isotope, a precise way to measure its isotopic abundance $^{39}Ar/Ar$ is needed, which is done with two fundamentally different methods.

Low level counting (LLC): In order to determine the concentration of ^{39}Ar in the total extracted argon from an environmental sample, low level counting utilizes the radioactive properties of ^{39}Ar. The argon sample is transferred into a counting tube and the β- radiation from the ^{39}Ar decays is detected with e.g. a gas-ionization detector (Geiger counter) or a scintillation detector.

While LLC is a technically simple and thus a very robust method, several significant challenges arise from both the low isotopic abundance and the low radioactivity of ^{39}Ar. The activity of atmospheric Ar is solely due to ^{39}Ar decays and has been determined as 1.01 ± 0.08 Bq/kg (Benetti et al. 2007). With a typical sample size for LLC of 1 L pure argon (corresponding to about 3200 L water), this corresponds to about 6 decays per hour. In practice, the sample sizes vary between 0.5 and 2 L argon and measurement times between 8 to 60 d (Loosli et al. 1980; Loosli et al. 1986; Collon et al. 2004). Those long measurement times partially result from the statistical errors associated with measuring such a rare event. Such a mechanism follows the Poisson statistic, resulting in a statistical error associated with the detection of N events of $\Delta N = \sqrt{N}$; a correlation that will be considered several more times in this work. Another experimental problem resulting from the low activity and long measurement times is the influence of background radiation. Background radiation can result from e.g. cosmic radiation and radioactivity in building structures (especially concrete). In order to minimize those influences, LLC laboratories have to be built underground as e.g. the LLC underground laboratory in Bern (Loosli et al. 1980) or the Laboratori Nazionali del Gran Sasso underground laboratory (Benetti et al. 2007). The necessity of large sample sizes of >1000 L water (or >1 t ice), limits the applicability of LLC to systems allowing for such huge sample sizes, mostly groundwater sampling.

For remote sampling locations, volume-limited sampling (e.g. Niskin bottles) or small sample reservoirs (e.g. specific layers in glacial ice), a method is needed that works with much smaller sample sizes. This applies to the method of Atom Trap Trace Analysis (ATTA). ATTA is a method borrowing fundamental techniques from atom physics, developed by Zheng-Tian Lu in the 1990s at the Argonne National Lab (Chen et al. 1999). The fundamental principles and the experimental realization will be discussed in more detail in the next chapter. ATTA utilizes a magneto-optical trap (MOT) to both capture and detect single atoms. The capture rate in atoms/hour can then be compared to a known standard and thus an isotopic abundance of the sample can be determined. ATTA does not rely on the radioactive nature of the isotope and is hence not limited by its decay rate. The main challenging factor is rather the low count rates. ATTA has been applied to several different isotopes, with ^{39}Ar, ^{81}Kr and ^{85}Kr the most common ones (compare Figure 4). Krypton ATTA was developed first (Chen et al. 1999) and its application to environmental systems has first been proven by ^{81}Kr ATTA analyses of old Sahara groundwater (Sturchio et al. 2004). Due to its higher isotopic abundances, ^{85}Kr and ^{81}Kr ATTA was developed earlier than ^{39}Ar ATTA and has been demonstrated in various applications with groundwater (Visser et al. 2013; Gerber et al. 2017; Yechieli et al. 2019) and glacier ice (Buizert et al. 2014) samples.

The isotopic abundance of ^{39}Ar is much lower than the ones of ^{81}Kr and ^{85}Kr and, thus, poses the main challenge for precision in ^{39}Ar ATTA measurements. Following the aforementioned statistical error, the error of an atom count (the measurement) is proportional to the square root of the total counted atoms, so to achieve e.g. a statistical error of 10%, 100 atoms need to be detected, as $\Delta N / N = \sqrt{N}/N = 10/100 = 10\%$. To reduce measurement time and/or subsequently increase precision, the main parameter that needs to be optimized is the detection efficiency and thus the count rate. Therefore, the counting rate of an atmospheric ^{39}Ar abundant sample has been optimized successively since the first proof of principle:

- ▶ Proof of principle: 0.6 atoms/h (Jiang et al. 2011)
- ▶ First groundwater study: 3.58 atoms/h (Ritterbusch et al. 2014)
- ▶ First ocean water study: 6-7 atoms/h (Ebser 2018a)
- ▶ First glacier ice study: 5 atoms/h (Feng et al. 2019b)
- ▶ Improved precision in 2021: 10 atoms/h (Tong et al. 2021)

In the reduction of the ^{39}Ar count rate in the glacier ice study, one can clearly see, that improving the count rate does not always work as expected. As a matter of fact, the measurements in this work were performed with atmospheric count rates between 2.5 – 6 atoms/h. The ATTA method still contains many unknown influences on its efficiency, resulting in setbacks in performance due to e.g. external factors like defects and accidents.

Still, tuning the efficiency is crucial. The measurements presented in this work required measurement times of about 20 hours and reached precisions between about 10 – 25%. If it becomes possible in the future to increase the precision further, the sample size needs to be considered carefully as well. As an atmospherically equilibrated water parcel contains about 6800 atoms of ^{39}Ar per liter, the intrinsic error of a 1 L water sample (shot noise: $\sqrt{6800}/6800 = 1.2\%$) could already be in the same order of magnitude as the measurement error.

1.6. Lake systems and stratification

With an estimated total storage of 175000 km³ water, lakes contribute only to about 0.3% to the world's freshwater budget, when excluding Antarctica (Oki and Kanae 2006). However, they can influence their local surroundings massively by positively affecting e.g. the ecology and the microclimate of the respective region. The lake's water column can be stratified and thus create horizontal zones characterized by different physical and bio-chemical properties, influencing the lake's biochemistry significantly (Boehrer and Schultze 2008). Stratification occurs when the water column develops a density gradient.

The density of water is mainly influenced by temperature, salt and other solutes. The temperature dependency of water exhibits a density anomaly with a maximum density at 4°C. In first approximation, the density as a function of the temperature (T in °C) can be described with Equation 11:

$$\rho(T) = 1000 - 7 \cdot 10^{-3} \cdot (T - 4)^2 \quad \text{in g/L} \qquad \text{Equation 11}$$

The influence of salt and solutes on the density is highly specific. All salts and many solutes increase the density, while other solutes, e.g. many hydrophobic hydrocarbons, decrease the density. This has to do with the volume a molecule or ion occupies in the water matrix and the substance's mass. Is the displaced water mass heavier than the solute particle, the overall density decreases. The density as a function of temperature and solute concentrations $C = \{c_1, c_2, ..., c_n\}$ can be given by Equation 12:

$$\rho(T, C) = \rho(T) \cdot \sum_i (1 + \beta_i \cdot c_i) \quad \text{in g/L} \qquad \text{Equation 12}$$

The sign of the factors β_i are determining the sign of the density change due to the solutes' influence (seeTable 3).

Solute	β_i
NaCl	0.719×10^{-6} l/mg
$Na_2(SO_4)$	0.922×10^{-6} l/mg
$Ca(HCO_3)_2$	0.813×10^{-6} l/mg
$Mg(HCO_3)_2$	0.815×10^{-6} l/mg
$Na(HCO_3)_2$	0.728×10^{-6} l/mg
$K(HCO_3)$	0.669×10^{-6} l/mg
$Fe(HCO_3)_2$	0.838×10^{-6} l/mg
$NH_4(HCO_3)$	0.462×10^{-6} l/mg
CO_2	0.273×10^{-6} l/mg
CH_4	-1.25×10^{-6} l/mg

Table 3: Selected β_i values (Aeschbach 2015).

An equilibrated water column with a negative density gradient (z direction is upwards) is stratified. That means, that a water parcel with density ρ_0 after a z-displacement z' along such a gradient $\rho(z)$ is affected by a restoring force due to buoyancy. In first approximation and assuming adiabatic circumstances, this displacement-induced restoring force can be described by the movement of a harmonic oscillator:

$$\rho_0 \frac{\partial^2 z'}{\partial t^2} = -g[\rho(z) - \rho(z - z')] \qquad \text{Equation 13}$$

With small z' this reduces to:

$$\frac{\partial^2 z'}{\partial t^2} = \frac{g}{\rho_0} \frac{\partial \rho(z)}{\partial z} z' \qquad \text{Equation 14}$$

This equation has a straightforward solution with:

$$z'(t) = z'_0 e^{i\sqrt{N^2}t}$$

With N being the Brunt-Väisälä Frequency:

$$N = \sqrt{-\frac{g}{\rho_0}\frac{\partial \rho(z)}{\partial z}}$$

With a negative N^2, Equation 15 gives the hyperbolic trigonometric functions, thus the displacement is not reversed, but further enhanced. The water column is instable. With positive $N^2 \leftrightarrow$ negative density gradient, one gets a sine or cosine function, the water parcel oscillates harmonically. The magnitude of N^2 is a good quantitative measure for the water column stability.

1.7. Holomictic and meromictic lakes

During the annual cycle of seasons, lakes experience changing environmental influences such as change in temperature, solar irradiation, precipitation and wind stress. A lake experiencing strong seasonality and the effects of the seasons on its water column is sketched in Figure 7.
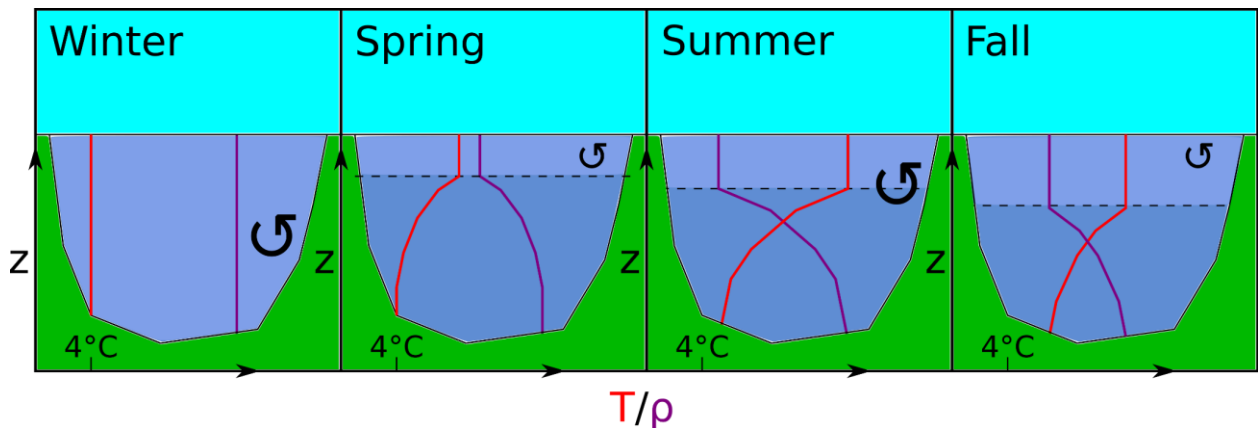
Figure 7: Annual cycle for holomictic lakes. During winter, wind forces are strong enough to mix the water column, which is not stabilized by a temperature gradient. During spring and summer, the upper layer warms up and is mixed. Below, a strong temperature gradient evolves, stabilizing this part of the water column. In fall, the upper layer cools down again and downwards diffusing heat weakens the temperature gradient. When the gradient is weakened enough, the wind forces can induce mixing again. During a cold winter e.g. with an ice sheet on top, a negative temperature gradient below 4°C can temporarily stabilize the water column again. In this case, the lake is called dimictic.

A lake experiencing annually or biannually mixing is called holomictic. This is the case for nearly all lakes in regions with notable summer/winter seasonality. A special case are lakes with high salt concentrations in the bottom layers. The high salt content may e.g. be the result of groundwater intrusions carrying high amounts of solutes, as can be observed, for example, in mine pit lakes (Horn et al. 2017). Those lakes with very briny bottom layers are often not able to mix fully in the cold season, as the strong

salt gradient remains, keeping the density gradient intact. Therefore, these lakes are called meromictic and the bottom layers are called hypolimnion.

Figure 8 shows what the vertical profiles of a holomictic freshwater lake and a meromictic lake with a briny hypolimnion might look like and how temperature and salinity can impact the vertical stratification.
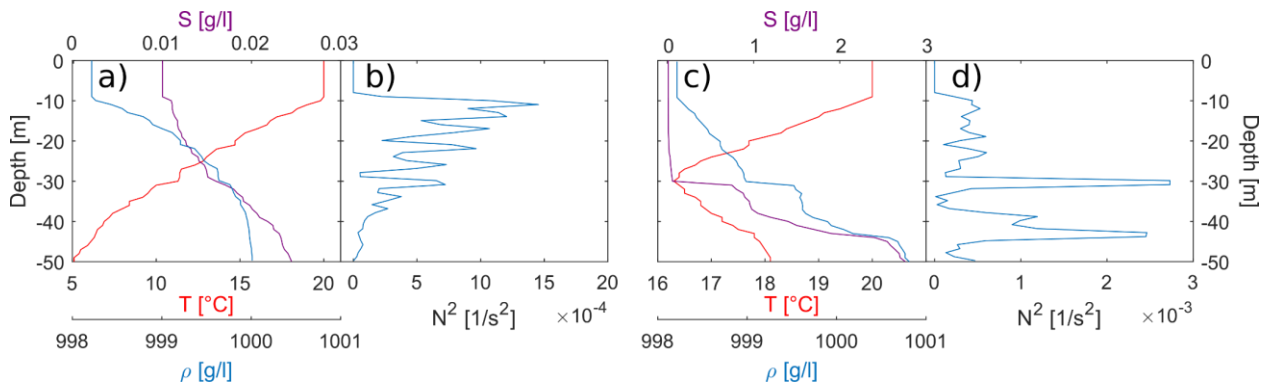
Figure 8: Sketches of hypothetical CTD profiles visualizing the impact of temperature and salinity on density. a) A subtropical lake in early summer with a week salt gradient. The density is dominated by the influence of the temperature. b) The Brunt-Väisälä frequency. The strong density gradient between 10 -35 m stabilizes the column. Below 45 m, the lake might be mixing again. c) A tropical lake with a briny hypolimnion. Below 30 m, the density is strongly dominated by salinity. Even negative temperature gradients can be stable in such regimes. d) The strong salt gradients form strong boundaries at 30 and 43 m depth.

1.8. Limnic eruptions

As the bottom layer of meromictic lakes is not mixed annually, it is possible for the hypolimnion to accumulate solutes. Those solutes can also include volcanic gasses like methane and CO_2. If those gasses are accumulating for a long time until the water column is (nearly) saturated, catastrophic events could occur. As soon as a strong enough disturbance in the stratified water column occurs (e.g. landslide, earthquake, volcanic eruption), water from a low layer can move up and the contained gas, now experiencing lower hydrostatic pressures, would start to form bubbles. Those bubbles would rise up and pull surrounding water with them. This pulled water is then itself positioned at lower hydrostatic pressure and, thus, more bubbles would form. This positive feedback loop is capable of degassing a whole lake in a very short time, i.e. a limnic eruption is happening.

On August 21st in 1986, the crater lake Nyos erupted in Cameroon (Kling et al. 1987). A subsurface landslide probably triggered this event, upon which CO_2 that had been accumulated in the hypolimnion was released very fast. The released CO_2, heavier than air and cooled upon expansion, spilled over the rim of the crater and into the adjacent valley, displacing air and thus breathable oxygen. Hours later, about 1700 people and 3000 cattle were dead.

After this shocking event, a lot of efforts were focussed on a better understanding of how such events can happen, which lakes could pose a similar danger and how limnic

eruptions can be prevented. For Lake Nyos, the danger was resolved by installing a simple degassing device, a vertical steel tube going from near the lake ground to the surface (Kling et al. 2005; Halbwachs et al. 2020), forming an air-lift pump. Through this tube, water is pre-pumped, and due to the same principle powering a limnic eruption, bubbles form, which then maintain the water flow so pumping can be stopped. So basically, a small and controlled limnic eruption confined to the tube is continuously removing the lake's gas in a safe manner. The speed the gas water mixture achieves in the tube is so high, it formed a naturally propelled fountain of a height of up to 46m (see Figure 9).

Figure 9: The Lake Nyos degassing facility with its highest recorded fountain height of 46m in February 2001 (Halbwachs et al. 2020).

1.9. Lake Kivu

Lake Kivu is a meromictic Lake lying on the border between the countries Rwanda and the Democratic Republic of the Congo (DRC). With its extreme gas content and the hazard it poses it is in the interest of researchers since decades (Peeters 1957; Pouclet 1975; Descy et al. 2012).

Lake Kivu is the main system of interest in this project. Hence Lake Kivu and its geologic history will be introduced shortly in the following. In the chapters 4 and 5 Lake Kivu will be introduced again, then focusing on the aspects important for the respective chapters.
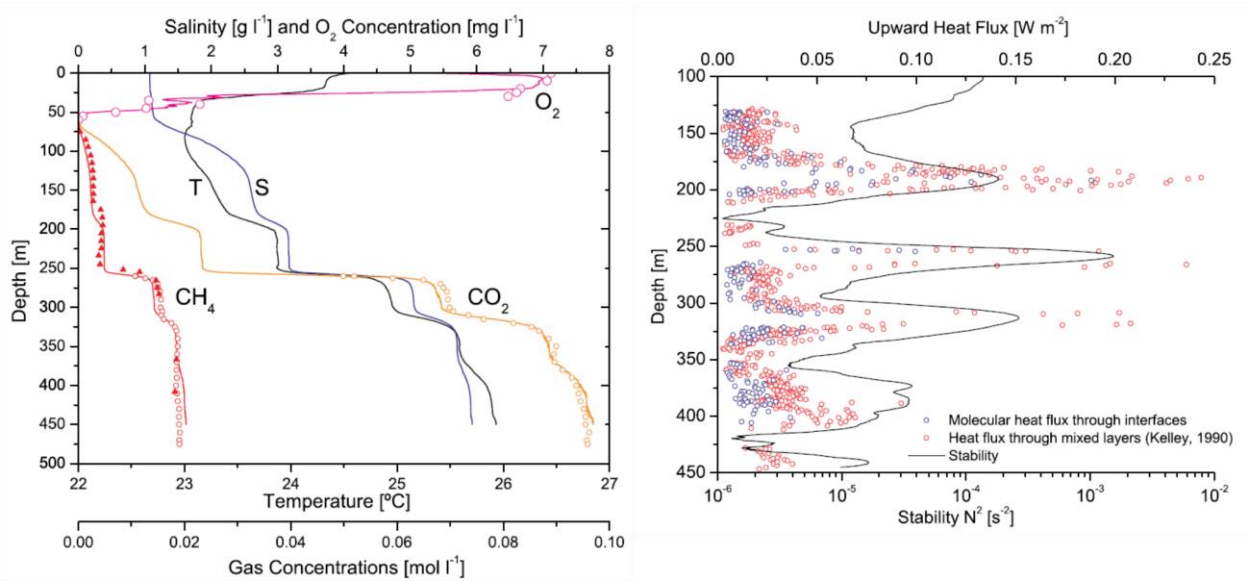
Figure 10: CTD Profile of Lake Kivu including O_2, CO_2 and CH_4 concentrations. At the depths of about 190, 250, 330 and 370 m, the water column shows very strong gradients, originating from salt-rich cold and warm subsurface groundwater discharges (Ross et al. 2015). On the right, the Brunt-Väisälä frequency shows strong boundaries at those depths. The density gradient of Lake Kivu below 70 m is dominated by salinity. Thus, the temperature can increase downwards due to geothermal influences without disturbing the stability of the water column. Both graphs originate from (Schmid et al. 2005) .

Figure 10 shows a CTD profile and the concentrations of O_2, CO_2 and CH_4 of Lake Kivu. The strong stratification of this lake is dominated by strong salt gradients maintained by several subsurface groundwater inflows (Schmid et al. 2005; Ross et al. 2015). The salt gradient is so strong that it is able to maintain the strong destabilizing temperature gradient caused by warm groundwater influxes and geothermal effects. The strong density gradient also causes a very distinct stratification below a mixed layer at a depth of about 50 m. The stratified layers are anoxic and contain an increasing amount of dissolved CO_2 and methane with increasing depth. The origin of the CO_2 is probably volcanic and the CH_4 might be of volcanic origin, a result of microbial methanogenesis or a combination of both (Descy et al. 2012). The concentration of the dissolved gasses is locally at about 60% of saturation (Boehrer et al. 2019). The danger of a limnic eruption, although not yet imminent, might increase in the future. Consequently, the gas accumulation rates of Lake Kivu are a subject of recent investigations. However surprisingly, the gas content seems not to have increased significantly over the past 50 years (Bärenbold et al. 2020b).

To decrease the risks of limnic eruptions at Lake Kivu, a modified variant of the air-lift pump is used to address the presence of the precious methane. Instead of letting the gas evade into the atmosphere, it is processed to increase methane concentrations to about 60-80 % (Gill 2019; Descy et al. 2012) so it becomes flammable. The gas can then be used in power plants to generate electricity and heat. With one running plant and several more in planning and construction, a total electric power generation of several 100's MW might be possible in the future (Symbion 2021; Contour Global 2021). With the border of Rwanda and DRC going through the lake, this resource is

shared and power generation is not only a source of electricity and safety, but could also be an anchor of diplomatic stability between both states (Doevenspeck 2007).

## 1.10. Lake Kivu – geology and geography
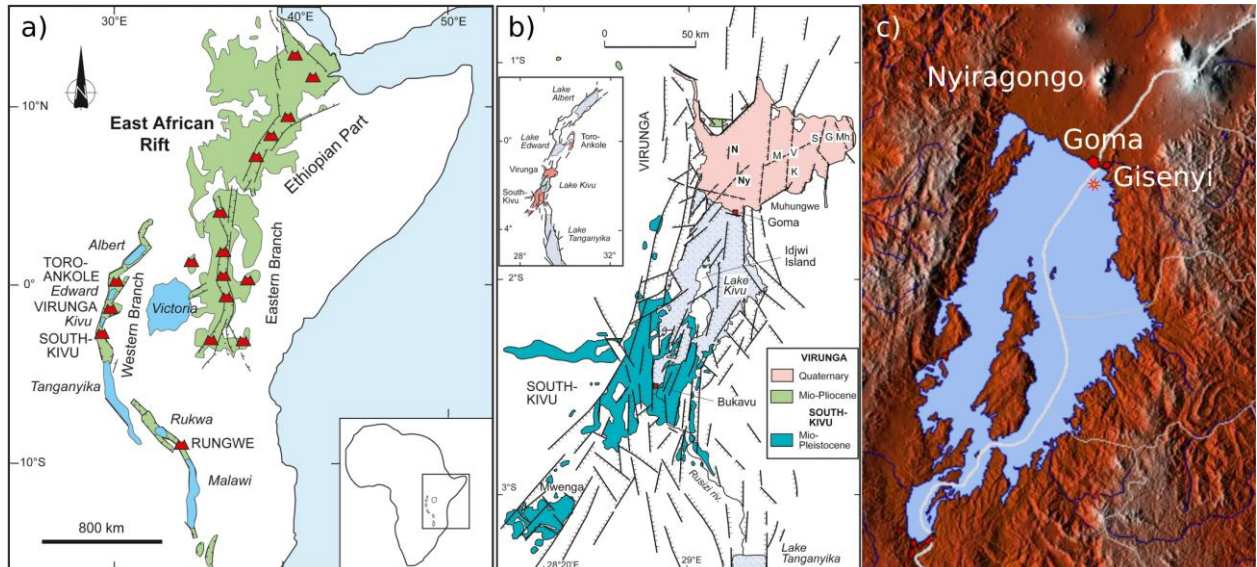
Figure 11: a) Geology of the East African Rift (EAR). The EAR is an active continental rift zone in East Africa, where the African Plate is splitting into the Somali- and the Nubian-Plate. Along the rift zones, the geology is characterized by strong volcanism and land subsidence. The depression zones include some of the largest lakes on earth, Lakes Victoria, Tanganyika and Malawi, as well as some smaller lakes like Lake Kivu. b) The rift system around Lake Kivu in between the Nubian Plate (west) and the Victoria microplate. The quaternary Nyiragongo magma field in the north created Lake Kivu in its current form ca. 12000 years ago. Both a) and b) from (Pouclet and Bram 2021). c) Physical map of Lake Kivu with the largest city Goma and the sampling point for the measurements presented here (red/yellow star near Gisenyi). The map was created using the free online tool 'maps-for-free.com'.

Lake Kivu is a rift lake located in the western branch of the East African Rift System (EAR). The western branch of the EAR extends from Lake Albert in the north to Lake Malawi in the south. Lake Kivu is centered on the rift axis and confined in the south by Miocene to Pleistocene eruptive rock. The northern closure of Lake Kivu is very young as it developed with the activity of the Virunga volcanism, especially Nyiragongo, around 14 – 10 kybp. Thus, the northern outflow to Lake Albert was interrupted and Lake Kivu's level raised to its current state with a southern outflow via the Ruzizi river to Lake Tanganyika. Over the period from 10 – 1 kybp, Lake Kivu showed several strong changes in hydrothermal activities, chemistry and stratification. The last critical event, probably a limnic eruption, happened around 1000 – 800 ybp. From this time until today, the current thermos-haline stratification has stabilized (Ross et al. 2014). The geological history of Lake Kivu is roughly summarized in Table 4.

Miocene	Pliocene	Pleistocene	Holcene
23 – 5.3 million ybp	5.3 – 2.6 million ybp	2.6 million – 12000 ybp	12000 – 0 ybp
From ≈ 20 mybp: East African Rift develops		Northern closure of Lake Kivu	
	Southern closure of Lake Kivu		

Table 4: Simplified geological history of the EAR and Lake Kivu (Ross et al. 2014; Pouclet et al. 2016; Pouclet and Bram 2021). Color scale corresponding to Figure 11 a) and b).

Lake Kivu in its current state has a surface area of 2386 km², a volume of 549 km³ and a catchment area of 2700 km². The surface lies at 1463 m above sea level and the maximal depth is 486 m. The shoreline is inhabited with the largest cities in DRC, i.e. Goma (2.000.000) and Bukavu (700.000), and, in Rwanda, the city Gisenyi (100.000).

2. The fundamentals of ATTA

Argon Trap Trace Analysis ATTA, is an atom optical method to measure the isotopic abundance of the radioisotope ^{39}Ar. ATTA relies on photon scattering of atoms and its resulting momentum transfer. The following chapter aims to provide the theoretical basis for these processes and will mainly follow (Metcalf and van der Straten 2002).

2.1. Photon scattering and momentum transfer

When a photon with wavelength λ scatters with an atom, it excites an electron from its ground state into an excited state only if λ matches an internal energy transition of the atom. Following momentum conservation, the momentum change Δp of the atom due to the scattered photon of frequency v:

$$\Delta \mathrm{p}_v = \hbar \mathrm{k} = \frac{h}{\lambda}$$

Equation 17

On relaxation to a lower energy state the atom emits a fluorescence photon via spontaneous emission. Spontaneous emission is randomly omnidirectional, as is the momentum transfer resulting from that emission $\vec{p}_F$. For N scattering processes of directed photons and subsequent spontaneous decay, one gets a net momentum transfer $\vec{P}$ on the atom of:

$$\vec{P} = \sum_{i=1}^{N} \left(\Delta \vec{p}_{v,i} + \underbrace{\Delta \vec{p}_{F,i}}_{\Sigma = 0} \right) = N \cdot \Delta \vec{p}_v$$

Equation 18

This process is also depicted in Figure 12.
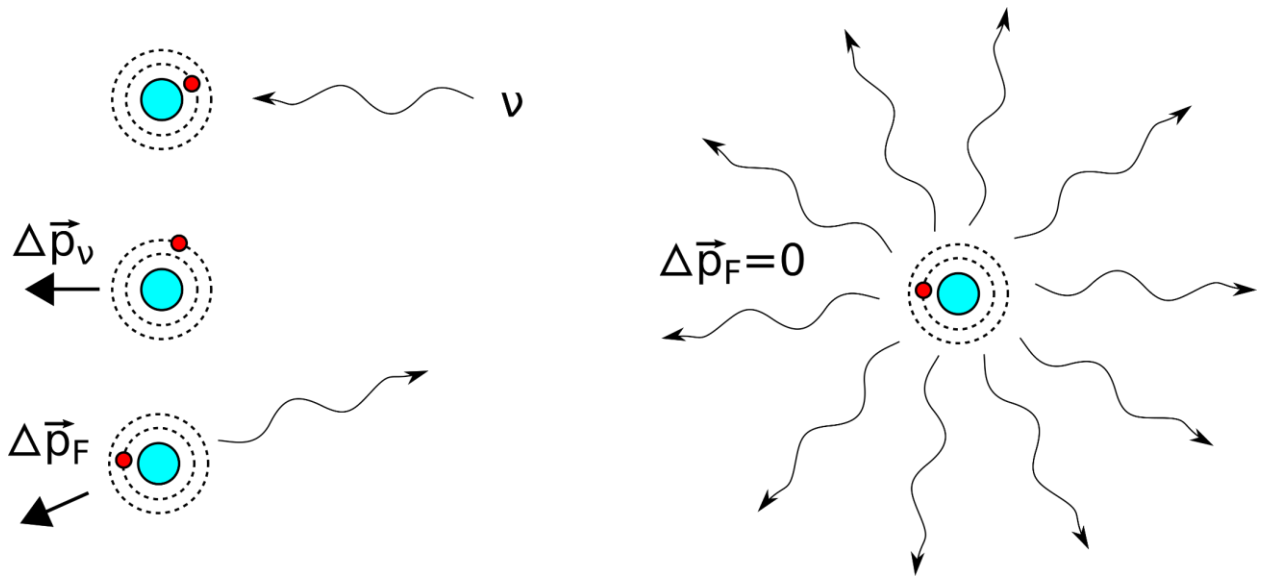
Figure 12: Sketch of the momentum transfer via photon scattering. A photon is absorbed by a ground state atom, the photon's momentum is transferred and the atom is in its excited state. The electron relaxes back to its ground state and via spontaneous emission, a fluorescent photon is emitted, transferring reversely directed momentum. When this process is repeated, the momentum transfers from the directional scattered photons add up to a finite value, while the momentum of the omnidirectional spontaneous emission photons add up to zero.

For a photon to scatter with an atom, its frequency needs to match an energy gap of the electronic configuration of the atom. The lowest energy gap that can be utilized for a scattering process is the transition from a valence electron to the next unoccupied orbital that is allowed by the dipole selection rules. The electronic structure of Argon is shown in Equation 19.
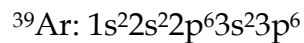
$$^{39}\text{Ar: } 1s^2 2s^2 2p^6 3s^2 3p^6 \hspace{4cm} \text{Equation 19}$$

As a noble gas, argon has a closed orbital shell and the transition energy for a valence electron to reach the next free orbital is E = 11.7 eV very high, requiring photonic excitation with a wavelength λ as given I in Equation 20:

$$\lambda = 107\text{nm} \iff E = h \cdot \frac{c}{\lambda} = 11.7 \text{ eV} \hspace{2cm} \text{Equation 20}$$

The energy spectrum of ^{39}Ar is shown in Figure 13.

Argon 40

Argon 39

ΔE [MHz]   F

j = 1/2   j = 3/2

J

2p$_1$ ——— 0	
2p$_2$ ——— 1	
2p$_3$ ——— 2	
2p$_4$ ——— 1	

J

2p$_5$ ——— 0
2p$_6$ ——— 2
2p$_7$ ——— 1
2p$_8$ ——— 2
2p$_9$ ——— 3
2p$_{10}$ ——— 1

1877.1   1/2
1655.0   3/2
1290.4   5/2
791.2   7/2

2p$_9$ J = 3

168.7   9/2
0
-562.5   11/2

-1384.5   13/2

^{40}Ar:-94.6

4th Repumper
^{40}Ar -1440.5

1s$_2$ ——— 1   Quench
                801.699 nm
1s$_3$ ——— 0   842.696 nm

Cooling Transition
811.754 nm

1s$_4$ ——— 1

1s$_5$ ——— 2

105 nm

107 nm

1s$_1$ ——— J = 0

1s$_5$ J = 2

3rd Repumper
^{40}Ar -1172.1

2nd Repumper
^{40}Ar -749.5

1st Repumper
^{40}Ar -187.9

2636.3   3/2

1868.7   5/2

823.6   7/2

0
-469.1   9/2

Cooler
^{40}Ar +492.2

-1971.3   11/2

Figure 13: Electronic spectrum and transitions of ^{40}Ar and ^{39}Ar in Paschen notation. The graphic is modified from (Ritterbusch 2013). The depicted transitions are: ^{40}Ar Green: Quench transition and fluorescence. Red: closed cooling transition. Black dashed: Transition of the valence electron to the next state for the ground state argon. ^{39}Ar Red: closed cooling transition. Blue: Repumper transitions (4th not applied in experiment). The additional splitting of the ^{39}Ar is due to its nuclear spin of 7/2. The ΔE notation (^{40}Ar-94.6) reads: photon frequency of the cooling transition minus a detuning of 94.6 MHz: λ = 811.754 nm + Δλ ↔ f = 369.3 THz - 94.6MHz.

Light of 107 nm is in the extreme ultra violet (XUV) spectrum and nearly impossible to generate and to handle with current experimental methods. Therefore, excited argon that can build a metastable electronic configuration (see Equation 21) is used.

$$^{39}Ar^*: 1s^2 2s^2 2p^6 3s^2 3p^5 (4s^1 = 1s_{5(J=2)} \text{ Paschen})^4 \qquad \text{Equation 21}$$

The 4s orbital in ^{40}Ar features a fine structure and is split into four sub-states due to Spin-orbit-coupling ($1s_{2\text{-}5}$ in Paschen notation). For a transition to be allowed, the dipole selection rules need to be fulfilled:

$$\text{For } ^{40}Ar: \Delta J = 0, \pm 1$$
$$\text{For } ^{39}Ar: \Delta F = 0, \pm 1$$

Equation 22

With J being the quantum number for the total angular momentum and F being the quantum number for the total angular momentum including the nuclear spin, relevant for ^{39}Ar also featuring a hyper fine splitting. The electronic energy spectrum of ^{39}Ar and ^{40}Ar is shown in Figure 13 using the Paschen notation. The transition $1s_5 \rightarrow 1s_1$ has an angular momentum change of $\Delta J = 2$ and is therefore not possible via dipole transition. This leads to a mean lifetime of this state of about 38 s, making it metastable. Due to the complications of UV laser light mentioned earlier, this state is produced by an argon plasma. Recombinant Ar ions and electrons mostly produce ground-state Ar, but with a low probability also the metastable Ar*.

The metastable argon now has the big advantage that it possesses a much smaller energy gap for its lowest energy transition of the valence electron as it is now out of its noble gas configuration. With an energy gap of about 1.53 eV, the transition $1s_5 \rightarrow 2p_9$ can be excited using 811.754 nm light, which is in the near infrared (IR) spectrum and in the range of standard optics and lasers. With a total angular momentum of J = 3, an electron from $2p_9$ can only relax back to $1s_5$ with J = 2. The $1s_5 \rightarrow 2p_9$ is therefore called a closed transition, as the scattering process can be repeated, as long as the metastable Ar* exists. This transition is the cooling transition used in the ATTA experiment.

2.2. ^{39}Ar scattering and electronic spectrum

The electronic transition spectrum of ^{39}Ar compared to ^{40}Ar is different due to the isotopic shift which, in this case, is caused by two different factors. The mass change

---

[4] The Paschen notation here is used in order to account for the different sub-states of the 4s1 orbital caused by the fine structure splitting (Moore 1971). The structure $xy_{z(J=0, 1, 2, 3, ...)}$ is composed by: x: general quantum number n minus an offset, so, that in the described system x starts with 1. y: The angular momentum quantum number L = 0 's', L = 1 'p', L = 2 'd' … z: numbering increasing with energy. J = 0, 1, 2, … the combined quantum number J.

of the nucleus and the nuclear spin of ^{39}Ar both change the electronic energy levels slightly.

^{39}Ar has a nuclear spin of I = 7/2. The interaction of the nuclear spin with the total angular momentum leads to a hyperfine structure. The hyperfine structure causes the orbitals to further split up into sub-states with F = {|J – I|, ... , |J + I|} (see the right side of Figure 13). The cooling transition becomes the transition 1s$_5$(F=11/2) → 2p$_9$(F=13/2).

On the generation of the metastable ^{39}Ar*, the electrons in the 1s$_5$ state are distributed thermally over the sub-states F = {11/2, ... ,3/2}. In order to populate all the electrons in the lowest F = 11/2 state, additional laser frequencies (called repumper) are used.

The function of the repumpers is explained using repumper number 1 as an example: Electrons are excited from 1s$_5$(F=9/2) → 2p$_9$(F=11/2). Following the selection rules (see Equation 22), the electrons can then either relax to 1s$_5$(F=9/2) or 1s$_5$(F=11/2) with nearly the same probability. Each scattering process reduces the probability of the initial electrons to relax in the 1s$_5$(F=9/2) state. This process happens with all repumpers, so that after a number of repetitions, the states 1s$_5$(F≠11/2) will be depopulated into the state 1s$_5$(F=11/2).

2.3. Isotopic separation

In the following, the metastable ^{40}Ar* or ^{39}Ar* will be referred to as ^{40}Ar or ^{39}Ar, respectively, if not mentioned otherwise.,

The isotopic shift ^{40}Ar → ^{39}Ar changes the scattering frequency of the cooling transition by ΔE = 492.2 MHz. Regarding the wavelength, that makes a difference of:

$$\lambda = 811.754 \text{ nm}$$
$$\Delta\lambda = 0.001 \text{ nm}$$

Equation 23

The probability of a ^{39}Ar-resonant photon to scatter off-resonantly, e.g. scatter an ^{40}Ar instead, is the inverse of the selectivity S given by (Collon et al. 2004):

$$S \approx 4 \cdot \left(\frac{\Delta E}{\Gamma}\right)^2 \approx 712$$

Equation 24

With Γ being the natural linewidth of the transition, here $\Gamma = 2\pi \cdot 5.87$ MHz. . That means, with $N_{40Ar} = N_{39Ar}$, every 712 resonant ^{39}Ar scatterings, one ^{40}Ar atom is excited off-resonantly by a ^{39}Ar-resonant photon. With the natural abundance of $R_A = {}^{39}$Ar/^{40}Ar = 8.1 x10^{-16}, the probability of a ^{39}Ar-resonant photon to scatter an ^{39}Ar atom over an ^{40}Ar atom is given by:

$$\frac{P_{39}}{P_{40}} = S \cdot R_A \approx 6 \cdot 10^{-13}$$

Equation 25

The probability for N consecutive photons to resonantly scatter ^{39}Ar is given by:

$$\left.\frac{P_{39}}{P_{40}}\right|_N = S^N \cdot R_A \qquad \text{Equation 26}$$

For N > 6 photons, this selectivity becomes greater than 1 ($P_{39}/P_{40}|_{N=6}$ = 105) and grows exponentially in N. So it can be inferred that a resonant ^{39}Ar multi-photon scattering event with $N \gg 6$ gives perfect selectivity for ^{39}Ar from its huge ^{40}Ar background.

2.4. Laser cooling

The principle of momentum transfer via directional photon scattering is the foundation for the field of laser cooling and all its adjacent fields like Bose-Einstein Condensation, sparking the works of many researchers awarded with two Nobel Prizes (Nobel Foundation 2021):

1997: Steven Chu, Claude Cohen-Tannoudji, William D. Phillips - for development of methods to cool and trap atoms with laser light.

2001: Eric A. Cornell, Wolfgang Ketterle, Carl E. Wieman - for the achievement of Bose-Einstein condensation in dilute gasses of alkali atoms, and for early fundamental studies of the properties of the condensates.

Laser cooling is equivalent to slowing down an atom, since the ideal gas law associates the mean velocity of the gas particles of an ideal gas with:

$$E_{thermal} = \frac{3}{2} k_B T \qquad \text{Equation 27}$$

The thermal energy of a gas particle at room temperature is about 25 meV. The thermal energy of an ideal gas is equivalent to the mean kinetic energy of the gas particles. For ^{39}Ar at room temperature, the velocity and the associated momentum is therefore:

$$v_{th} = \sqrt{\frac{2 \cdot E_{th}}{m}} \approx 350 \frac{m}{s}$$
$$P_{th} = \sqrt{2 \cdot E_{th} \cdot m} \approx 2.3 \cdot 10^{-23} \frac{kg \cdot m}{s} \qquad \text{Equation 28}$$

To slow down a thermal ^{39}Ar to v = 0, the momentum transfer of N photons needs to be equal the momentum of a thermal ^{39}Ar atom. The number of necessary photons N can be inferred by:

$$P_v(811.754\ nm) = \frac{h}{\lambda} \approx 8.2 \cdot 10^{-28} \frac{kg \cdot m}{s}$$

$$N = \frac{P_{th}}{P_v} \approx 28000$$

Thus one can easily see, that the number of photons necessary to slow down a ^{39}Ar atom to still stand is enough to grant perfect ^{39}Ar/^{40}Ar selectivity.

2.5. Magneto optical trap

The main atom-optical element utilized in ATTA is the magneto optical trap (MOT). Its basic functionality is sketched in Figure 14.
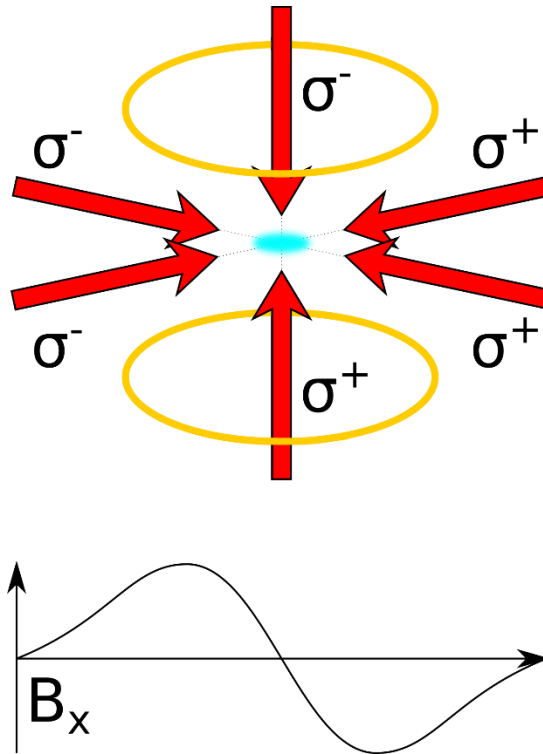
Figure 14: Sketch of a magneto optical trap (MOT). Three pairs of opposing circular polarized laser beams in combination with a magnetic field gradient (orange: anti Helmholtz solenoids) are forming the MOT. At the center, the laser beams are not resonant with the atoms. Upon a displacement of an atom out of the center, the Zeeman-shift acts on the energy levels and the transition 1s$_5$ → 2p$_9$ becomes resonant with the laser beams opposing the displacement. The atom experiences a reversing force and, thus, is trapped in the center of the MOT. The circular polarization transfers the necessary angular momentum change ΔF = +1. The opposing polarization direction of the two opposing beams in combination with the magnetic field gradient ensure no off-resonant destabilizing scattering processes.

The central element of the ATTA machine, the MOT, is trapping ^{39}Ar atoms in its center. In order to trap an atom, enough scattering processes have to occur to slow the atoms down to standstill and thus, the resonant multi photon scattering described

beforehand (Equation 29) is required. Therefore, a MOT tuned resonantly to the $1s_5 \rightarrow 2p_9$ transition of ^{39}Ar essentially captures ^{39}Ar atoms with a perfect ^{40}Ar background separation.

3. Experimental setup

A sketch and a short description of the current experimental setup with its key components is provided in Figure 15.

The central element of the ATTA setup is the already described MOT. The detection of the captured atoms is achieved with both a CCD camera and by measuring the photo-current on an avalanche photo diode (APD), which is focused on the center of the MOT.

The metastable Ar atoms are generated by a radio-frequency(RF)-induced plasma discharge run with an open $\lambda/2$ coil design with a frequency of ~150 MHz and a 100 W amplifier. This part of the setup is called source. The plasma is partially contained in a ceramic tube to reduce sputtering, the main cause for source replacement. The ceramic tube is mounted to a liquid nitrogen-cooled stainless steel vessel to reduce both heating effects of the 100 W RF discharge and also the temperature and, thus, velocity of the Ar atoms.

In between the source and the MOT are several elements enhancing the efficiency of the atom capturing and, thus, the precision. Directly following the source, the collimator is connected, i.e. two pairs of slightly tilted mirrors and a red detuned laser with a sheet profile. The collimator parallelizes the diffusive trajectories of the atoms coming from the source. Thereby, the collimator enhances the atom flux at the MOT by a factor of about 100. Behind the collimator, a magneto optical lens (MOL) is installed. The MOL is equivalent to a MOT, but missing one pair of the opposing laser beams. The two remaining beam pairs are perpendicular to the atom beam. The MOL forces off-center atoms towards the center and can be adjusted to focus the atom beam towards the MOT. The MOL enhances the atom flux by a factor of about 3. A detailed description on the collimator and the MOL can be found in (Ritterbusch 2013).

The next element behind the MOL is the quench laser. The quench laser reduces the dark current of the APD in the MOT caused by metastable ^{40}Ar atoms, which are also produced in the source and scatter the MOT laser beams off-resonantly. The quench has a wavelength of λ = 801.699 nm, driving the transition ^{40}Ar: $1s_{5(J=2)} \rightarrow 2p_{8(J=2)}$, from which the electron can relax further to $1s_4$ and finally to the ground state $1s_1$, without violating the dipole selection rule ΔJ = 0,±1: $1s_{5(J=2)} \rightarrow 2p_{8(J=2)} \rightarrow 1s_{4(J=1)} \rightarrow 1s_{1(J=0)}$ (compare Figure 13). Furthermore, the fluorescence of the $2p_8 \rightarrow 1s_4$ transition is used as a proxy to monitor the atom flux during a measurement. A detailed description of the quench system is given in (Ebser 2018a).
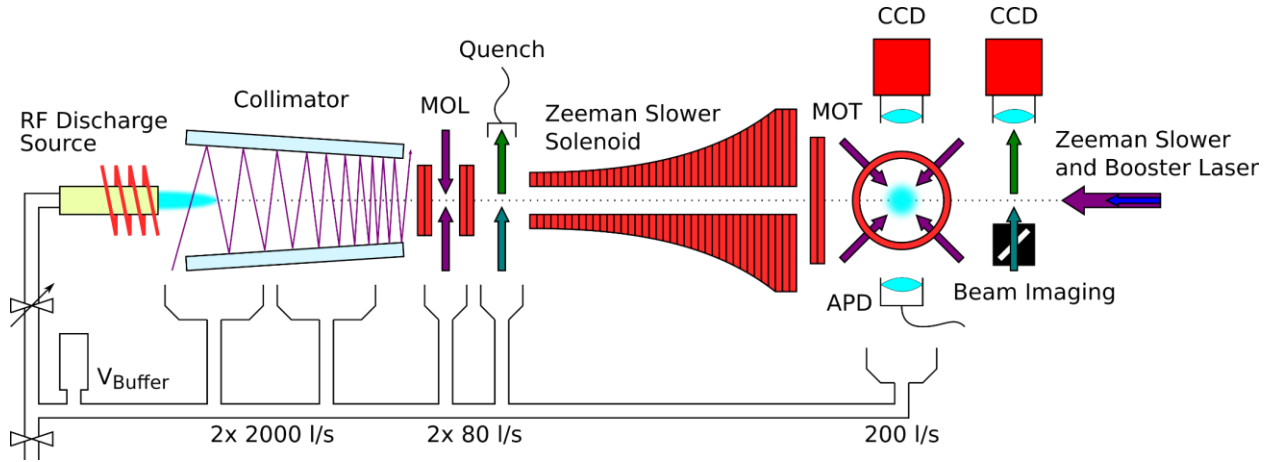
Figure 15: Sketch of the current ATTA setup. The RF discharge source generates the metastable Ar atoms. The collimator collimates the diverging trajectories of the atom beam. The magneto optical lens (MOL) focusses the beam onto the MOT. The quench de-excites metastable [40]Ar and thus reduces readout noise. The quench fluorescence monitors the atom flux. The increasing magnetic field in combination with a laser beam opposing the atom beam slows the atoms down. The MOT captures the atoms, which are then detected by both a CCD and an avalanche-photodiode (APD). The beam imaging is a sheet of light, whose fluorescence is used to monitor the atom beam shape. The vacuum system is closed so the sample is recycled through the machine during measurement.

The next element is the Zeeman slower, the combination of an increasing magnetic field and a laser that is strongly red-detuned from the cooling transition. The resonance frequency in the frame of reference of a fast atom is blue-detuned due to the Doppler shift. The Doppler shift is the shift in the relative frequency from the point of view of a moving frame of reference. In the frame of reference of a moving atom of the velocity v the frequency f_{photon} of the opposing laser beam shifts according to:

$$f_{atom} = f_{photon} \cdot \sqrt{\frac{c + v}{c - v}} \qquad \text{Equation 30}$$

With c being the vacuum speed of light. This Doppler-induced blue-detuning cancels out the red-detuned laser so it becomes resonant. The fast atom slows down until it is not resonant anymore. With an external magnetic field, the Zeeman shift is then used to readjust the resonance frequency of the slowed down atoms to the opposing laser beam. The Zeeman-shift is a shift in energy due to the interaction of an external magnetic field B with orbitals carrying a magnetic momentum $(m_L, m_J, m_F \neq 0)$[5]. With μ_B being the Bohr-magneton and g_j being the Landé-factor, the Zeeman shift changes the energies of the states according to:

$$\Delta E_{Zeeman} = \mu_B g_j m_j B \qquad \text{Equation 31}$$

---

[5] m_L, m_J, m_F being the magnetic quantum numbers. L, J, F are angular momenta, with the choice of letter depending of the presence of a fine-structure (J), a hyperfine-structure (F) or none of the aforementioned (L).

With an increasing external magnetic field, the atom beam is slowed down to slightly above the capture velocity of the MOT, which is about 60 m/s. The Zeeman slower is discussed in detail by (Feng 2019a).

The adjacent MOT is combined with an additional booster laser, that increases its maximal capture velocity and additionally has the beneficial effect of increasing the capture efficiency in decreasing loss due to beam spreading. For a detailed description see (Welte 2011).

Behind the MOT, a sheet of light cuts through the atom beam at an angle of 45°. The fluorescence of the ^{40}Ar beam is recorded by a CCD camera and is a powerful tool to monitor the shape of the atom beam and adjust the collimator and the MOL respectively. This beam imaging system is described in detail by (Ritterbusch 2013).
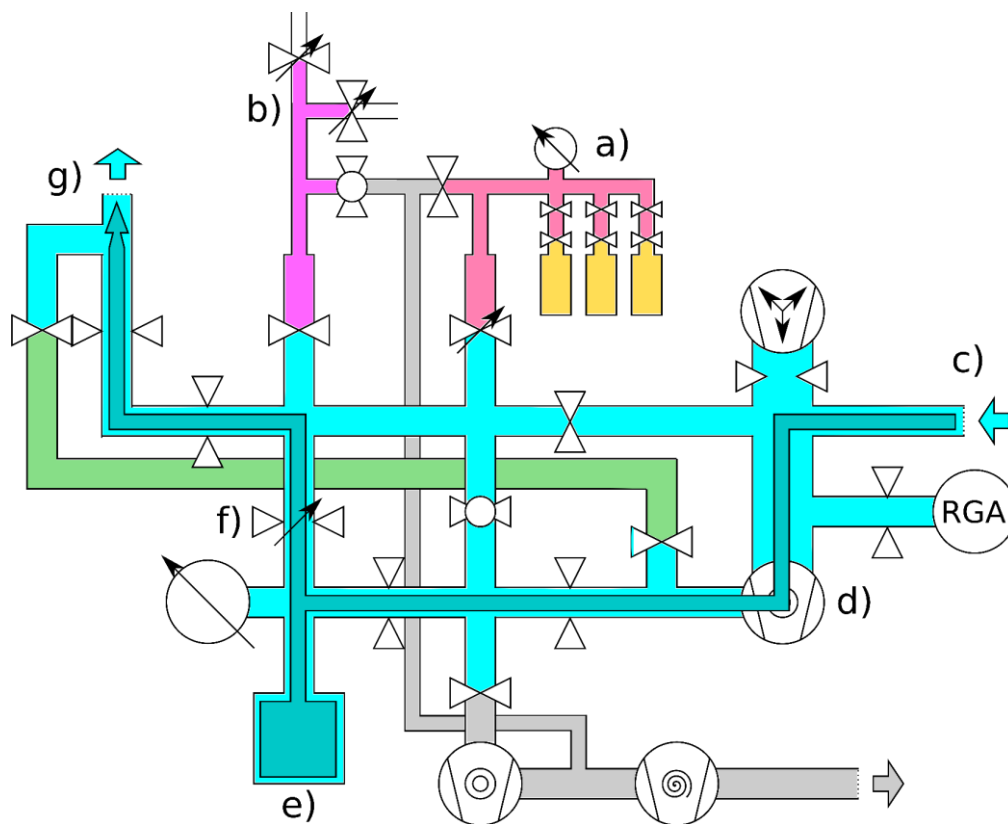
Figure 16: Detailed sketch of the current fore vacuum setup. At the sample port a), the standard samples (10x enhanced R_A, ^{39}Ar free Ar) are permanently installed. The sample of interest can be installed with a ¼" VCR connector. b) Permanently installed connections to Ar and Kr gas bottles. Both a) and b) can be roughly pumped independently by a bypass to the rough vacuum. c) Backflow from the vacuum pumps guided by a Ti-getter and a residual gas analyzer (RGA). d) 80 l/s Turbo molecular pump (TMP) compressing the recycled sample into a buffer volume e). The gas flux is regulated by a needle valve f) and guided g) towards the RF discharge source. Dark green: flow ^{39}Ar measurement configuration. Light green: shortcut for ^{85}Kr measurements, see also (Ringena 2021). Grey: Outflow.

The vacuum system is set up as a closed system during a measurement in the sense that all pump exhausts are guided towards a compressing pump which pumps them

into a buffer volume, from which it is guided to the plasma discharge source. This recycling system has been developed and optimized in order to measure samples with volumes as low as about 100 µL.

During the work described here, a new fore vacuum system was built which is sketched in Figure 16 and depicted in Figure 17. The design is based on the work of (Ebser 2018a) and has been optimized further to improve sample handling, the measurement routine, RGA-based leak detection and the overall workflow.

The installation of the Ti-getter and the RGA has been improved by positioning it close to the compressor pump (a turbo molecular pump, short: TMP) and by using larger diameter tubing. Since the machine runs in a closed recycling mode, avoiding leakage is of major importance, as any leaking gas will add up over time and dilute the sample. Leak testing is done by adjusting the RGA to sensitively detect helium. Helium is then then sprayed onto e.g. the tested gasket. As the gas with the smallest dynamic molecular radius, helium can pass through the smallest gaps and can be used to find leaks very efficiently with the RGA. For the RGA to detect the smallest leaks efficiently, it is crucial to reduce the distance in between the leak and the RGA. For that, the RGA was installed directly to the backflow of the whole machine. Additional valves and shortcuts in the fore-vacuum also improve leak testing efficiency. The accessibility of the buffer volume allows for adjusting its volume depending on the sample size to be measured.
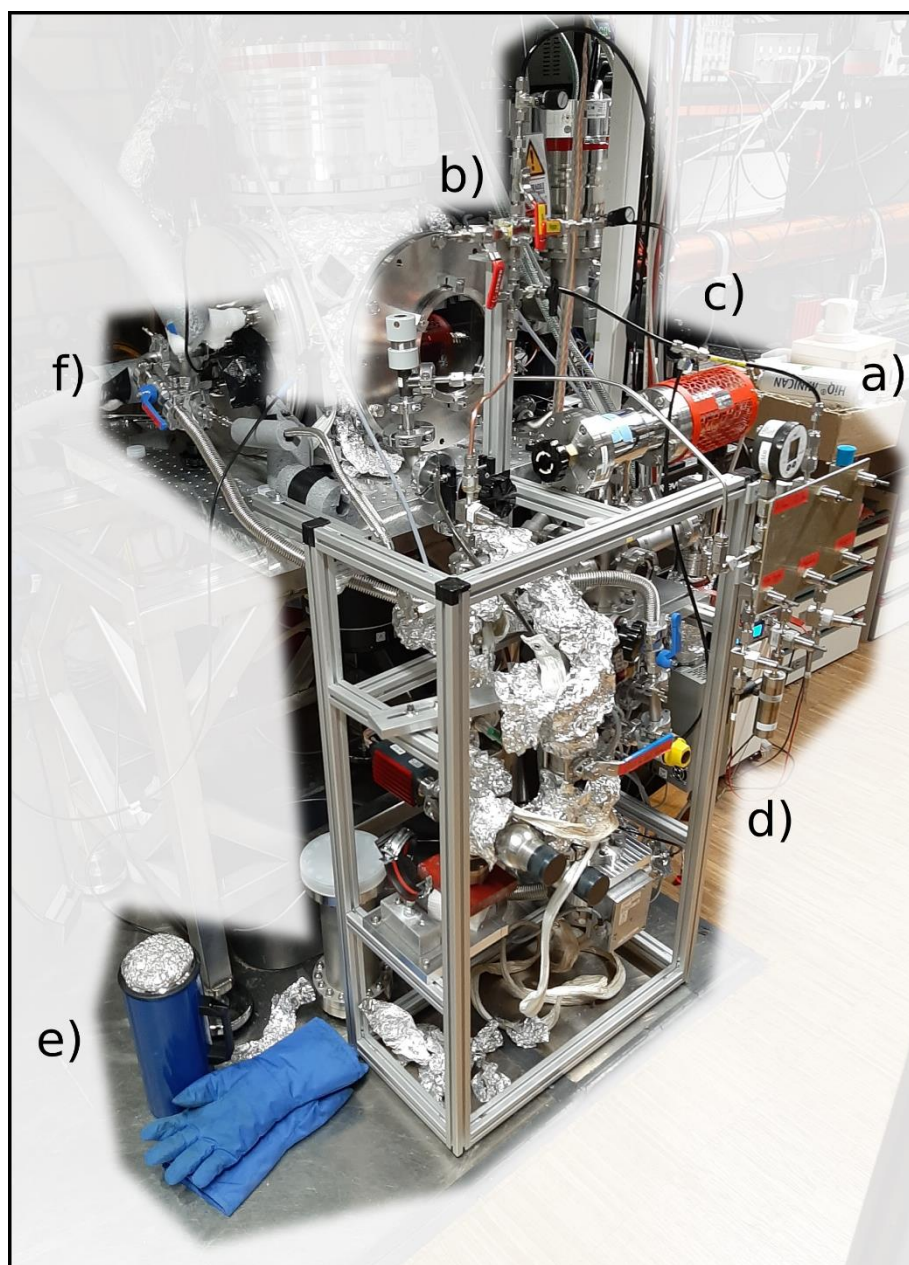
Figure 17: Photograph of the fore-vacuum in 2020. The whole setup was built on an aluminum extrusion rack in order to be modular and easy to copy. a) The sample port is mounted on a steel plate to guarantee rigidity. Accessible sample mounts improve the handling of the liquid nitrogen for cooling. b) The bottle port is decoupled from the sample port with up to three connectors for gas bottles. c) & d) the Ti-getter and the RGA are accessibly installed. e) Dewar and gloves for liquid nitrogen handling. f) Easily detachable connection to the RF discharge source.

3.1. Performance and accidents

The performance of the ATTA machine in this work suffered from two electricity blackout-induced incidents in the laboratory in 2018 and 2019. In 2018, a blackout caused damage to two crucial laser systems and several home-built electronic controllers. In 2019, a major blackout caused the two large 2000 l/s TMPs to shut down

in an uncontrolled way. Due to the vibrations of this shutdown adding up, the pumps crashed critically. Both rotors shattered and caused substantial damage by smashing a lot of the internal setup, e.g. the collimator (see Appendix Figure 57).

After the second blackout, a redesign of the source chamber and its mounting was performed. The redesign did not change anything regarding the optics and the metastable argon generation, but focused on a more rigid and vibration-dampening design. Furthermore, two uninterruptable power supplies (UPS) were installed to provide a stable power source for crucial components like vacuum pumps and lasers. In the case of a future blackout, the UPS could provide power for up to 12 minutes, which is sufficient for most local short-term blackouts happening in Heidelberg. Additionally, the power of a UPS is decoupled from the power grid, so grid irregularities will not threaten the sensitive electronics anymore.

We found that after the first repair, the count rates of up to 7 atoms/h achieved beforehand could not be reproduced, as the count rate is dependent on many factors, therefore optimization is very sensitive and tedious. Finally, after excessive optimization efforts, a count rate of up to 6 atoms could be achieved. This count rate was considered to be sufficient for the measurement of the groundwater samples of Salalah Oman and the ice samples from the Leupa Ice Cave (see chapter 6 for more on both). After the extremely demanding repair of the crashed TMPs in 2019, the count rate was drastically reduced to <1 atoms/h and it took several months, to improve the rate to a point where it was considered sufficient to measure the samples gathered in 2019 at Lake Kivu (see chapter 4). Those measurements were performed with count rates of 2.5 to 4 atoms/h.

3.2. Workflow and concentration determination

The workflow of a measurement day is determined by a 24 h routine. The measurement time of a sample is typically set to 20 h. This time is a good compromise between precision (increasing by $\sqrt{\text{Number of counted atoms}}$) and factors like performance drifts and contamination due to memory effects of the machine (steel implanted ^{39}Ar atoms from earlier runs can slowly sputter out again).

Before and after each measurement, the beam imaging tool is used to check for adjustment drifts. After the sample is measured, the sample is pumped out of the machine and thus destroyed. After that, about 1 ml$_{STP}$ of our standard sample with 10x enhanced R_A ^{39}Ar is measured for 2 h which provides us with the necessary reference. Henceforth this sample is called 10x reference. The 20 h and 2 h durations were chosen to achieve a standardized precision (e.g. count rate 5 atoms/h for atmospheric Ar and 50 atoms/h for 10x R_A → 100 ± $\sqrt{100}$ atoms ↔ 10% statistical error). After the 10x reference, the machine is cleaned for 1 – 1.5 h. During this time, the liquid nitrogen tanks for the source are refilled and a Kr plasma is ignited to sputter all ^{39}Ar atoms stuck to the surfaces in the source chamber. Additionally, the liquid nitrogen flow to the source is turned off for 2x 10 minutes to release adsorbed atoms from all cold surfaces. After this cleaning procedure, the next sample can be measured. To determine the influence of the memory effect of the machine on the

count rate, a [39]Ar-free sample is measured regularly. The [39]Ar atoms detected in those measurements are contamination atoms which are releases by the machine itself. The accumulation of contaminating [39]Ar atoms is assumed to be constant with time. A measured sample can thus be corrected by this accumulation rate. Extensive work on the influence of this contamination and its analysis for [39]Ar measurements can be found in the work of (Ebser 2018a).

3.3. Measurement analysis

In brief, the isotopic abundance (here: c [R_A]) of a sample is inferred by comparing the atom count rate of its measurement with the 10x reference count rates measured before and after the measurement (here: r_0 Especially for samples with a small volume or with low [39]Ar isotopic abundance, the influence of the contamination becomes critical. The number of the counted atoms N for a sample therefore needs to be corrected for this. The contamination is of two distinct origins: the before described accumulation of [39]Ar atoms out of the wall and the so-called cross-contamination. For the first effect, the constant increase of concentration gives an acceleration like term (here: a [$\mu L_{STP}(R_A)/h$]). The cross contamination is not increasing in time, but is constantly present. For our work with argon and in contrast to work with krypton (Ringena 2021) we found this part to be negligible. This results in the description of counted atoms given by Equation 32:

$$N(t) = \left[\left(c_{sample} + \underbrace{c_{cross} \cdot \frac{V_{cross}}{V_{sample}}}_{\approx 0}\right) \cdot (t - t_0) + \frac{1}{2} \cdot \frac{a}{V_{sample}} \cdot (t^2 - t_0{}^2)\right] \cdot r_0 \quad \text{Equation 32}$$

With t being the duration of the counting and t_0 the time the plasma source is turned on. With the previously determined contamination factor a, the reference count rate r_0 and the number of measured atoms N, the [39]Ar isotopic abundance c_{sample} can be determined.

In order to determine a reliable error of the measurement, a Bayesian calculus was developed (Ebser 2018a). This approach assumes all counted atom numbers to follow a Poisson distribution and all other relevant properties of the measurement to be Gaussian. Instead of single values for N, c, a, V and r_0, the probability distributions $\widetilde{N}, \tilde{c}, \tilde{a}, \widetilde{V}$ and $\widetilde{r_0}$ are used subsequently. The distribution of the concentration $\tilde{c}$ is obtained by a Monte-Carlo simulation of the distributions $\widetilde{N}, \tilde{a}, \widetilde{V}$ and $\widetilde{r_0}$. Redistributing Equation 32 one gets:

$$\tilde{c}_{sample} = \frac{\dfrac{\widetilde{N}}{\widetilde{r_0}} - \dfrac{\tilde{a}}{2 \cdot \widetilde{V}} \cdot (t^2 - t_0{}^2)}{(t - t_0)} \quad \text{Equation 33}$$

35

The concentration $\tilde{c}$ is now described by a non-parametrized probability distribution of the sample's ^{39}Ar isotopic abundance in units of the atmospheric ratio R_A. The most probable value produces the measurement value and a σ definition yields the error (e.g. 68% contained in 1σ, 95% in 2σ and so on). An advantage of this calculus is the easy combinability of several measurements i of the same sample:

$$\tilde{c}_{sample} = \prod_i \tilde{c}_{sample,i}$$

<div align="right">Equation 34</div>

One disadvantage is the necessary calculus in the background and the handling of such data and calculations by different users, not necessarily familiar with the methodology.

To make these calculations accessible for many users of different backgrounds, a simple and straight forward analysis routine was developed as part of this work. The main challenges for a user friendly analysis routine is to generate a low-threshold entry point, a simple operation and a clear and descriptive output.

In the following, the developed analysis routine will be summarized using one sample of this work's Lake Kivu campaign as an example.

Running Number ATTA Oben	Date and Time Start dd.mm.yyyy HH:mm:ss 24h Format	NameSample	Function Ref/Sample /Art/Atm /*Source/*Optm/*Mirror	Volume mlSTP Fehler 2%	Atomnumber	Runtime numeric h 30min = 0.5	Quadratic Time numeric h^2 (2.5 h)^2 = 6.25 h^2	Concentration e.g. 10 for Ref empty if unknown	References Running Numbers Comma Separated	ContCorr Running Numers Corresponding Cont Comma Separated
334	21.08.2020 13:57:00 10XRef1	Ref		1.254	58	2	5.3	10		
335	21.08.2020 16:43:00 Kivu225m2	Sample		1.311	26	11.5611111	154.7290426439		334,336	333,341,359,363,389
336	22.08.2020 13:24:00 10XRef1	Ref		1.3623	57	2.84003889	11.2979380827	10		
350	29.08.2020 14:52:59 10XRef1	Ref		1.276	78	2.49	15.39	10		
351	29.08.2020 19:54:00 Kivu225m1	Sample		1.2939	44	20	410.94		350,352	333,341,359,363,389
352	30.08.2020 16:19:00 10XRef1	Ref		1.95795	53	2.16	5.64	10		
373	21.09.2020 11:36:19 10XRef1	Ref		1.83255	85	1.99722222	7.0170882718	10		
374	21.09.2020 14:48:07 Kivu225m2	Sample		1.3053	51	18.6277778	384.9578141585		373,375	333,341,359,363,389
375	22.09.2020 10:18:57 10XRef1	Ref		2.18025	69	1.99722222	4.9971310001	10		
332	20.08.2020 14:30:00 10XRef1 1	Ref		1.99779	50	2	5.29	10		
333	20.08.2020 17:33:00 Dead	Dead		1.2654	2	20	410.92	0	332,334	
334	21.08.2020 13:57:00 10XRef1	Ref		1.254	58	2	5.3	10		
340	24.08.2020 16:40:00 10XRef1	Ref		1.39365	66	2.16388889	6.7831172487	10		
341	24.08.2020 19:43:00 Dead	Dead		1.28535	6	19.9972222	411.7277076371	0	340,342	
342	25.08.2020 16:12:00 10XRef1	Ref		1.51335	53	1.99722222	5.1036273218	10		
358	03.09.2020 11:26:50 10XRef1	Ref		1.71285	47	1.99722222	5.5208248552	10		
359	03.09.2020 14:22:15 Dead	Dead		1.3281	8	19.9972222	408.835975988	0	358,360	
360	04.09.2020 10:48:16 10XRef1	Ref		1.47915	48	2.13513528	5.7805745071	10		
362	05.09.2020 10:18:49 10XRef1	Ref		1.31385	48	1.99722222	4.9874888479	10		
363	05.09.2020 14:40:09 Dead	Dead		1.3338	9	19.9958331	411.4348440963		362,364	
364	06.09.2020 11:17:06 10XRef1	Ref		1.5276	38	1.99722222	5.5382417402	10		
388	03.10.2020 20:44:55 10XRef1	Ref		0.9291	52	1.99722222	7.3236796278	10		
389	03.10.2020 23:44:05 Dead	Dead		0.56715	8	11.6083333	184.1171121172	0	388,390	
390	04.10.2020 22:29:13 10XRef1	Ref		1.3851	44	1.99722222	4.8797686698	10		

Figure 18: Excerpt from the data spreadsheet 'DataRecord.ods'. Every measurement is given a unique running number and all relevant data can be entered either by hand or automatically. The measurements in red are highlighted as examples [335, 351, 374] and were all taken from Lake Kivu at depth 225m. Every measurement gets its respective references assigned (usually the ones directly before and after the measurement; running numbers highlighted in yellow). Additionally, every measurement gets assigned the applicable contamination measurement ([333, 341, 359, 363, 389], grey highlights).

The first step of the data analysis is to enter the measured atom number and all relevant measurement parameters into a database. To provide a low-threshold entry

point, this database is a simple standardized spreadsheet which can be filled either by hand or automatically. Figure 18 shows an excerpt of this spreadsheet with all entries relevant for the analysis of the Lake Kivu samples from 225 m depth.

The analysis routines are written in MatLab and consist of a set of one script and three functions. This process is visualized in Figure 19.
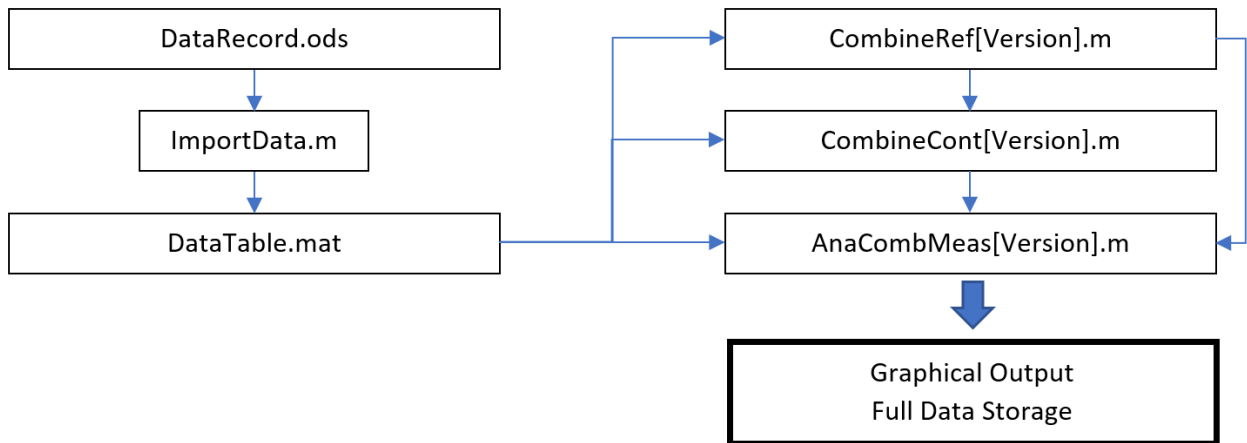
Figure 19: Organigram of the data analysis process. All data and programs are stored centralized at: \\AFS\.kip.uni-heidelberg.de\projects\matterwave\ATTA\Data\DataAnalysis.

A simple import script (ImportData.m) transforms the spreadsheet in a MatLab readable file (DataTable.mat). To analyze and combine a set of measurements, the analysis function *AnaCombMeas* is used. To analyze e.g. the above described sample set from Lake Kivu (running numbers 335, 351, 374), the function is executed in the MatLab command line with the following arguments:

```
AnaCombMeas1_3([335,351,374],'ATTA Oben',100000)
```

The argument 'ATTA Oben' describes the machine and the number 100000 defines the number of Monte-Carlo simulations to be done generating the probability distributions.

Each of the single measurements require a set of references, also defined in the spreadsheet. The analysis function automatically executes the function CombineRef to generated the combined reference for each measurement. The probability distribution for the combined reference [334, 336] relevant for the measurement 335 is shown in Figure 20 a). The CombineRef function can also be executed by itself with the following command:

```
CombineRef1_5([334,336],'ATTA Oben')
```

The *CombineRef* function does not need an argument for a Monte-Carlo simulation, as it is basically only a pointwise multiplication of multiple Poisson distributions.

Each of the single measurements also require a set of [39]Ar-free contamination background measurements (called *Dead* in laboratory slang). The set of contamination measurements for the set [335, 351, 374] is the same for every sample, although that is not a necessity. As contamination measurements also need references, the *CombineCont* function automatically executes the *CombineRef* function as well. The *CombineCont* function can also be executed independently with the command:

```
CombineCont1_8([333,341,359,363,389],'ATTA Oben',100000)
```

With [333, 341, 359, 363, 389] being the set of relevant set of contamination measurements also shown in Figure 20 b).

38

With the references and contamination data now analyzed the main function *AnaCombMeas* then calculates the probability distribution for the ^{39}Ar isotopic abundance following Equation 33. The graphical output of this calculation is shown in Figure 20 c) and d).
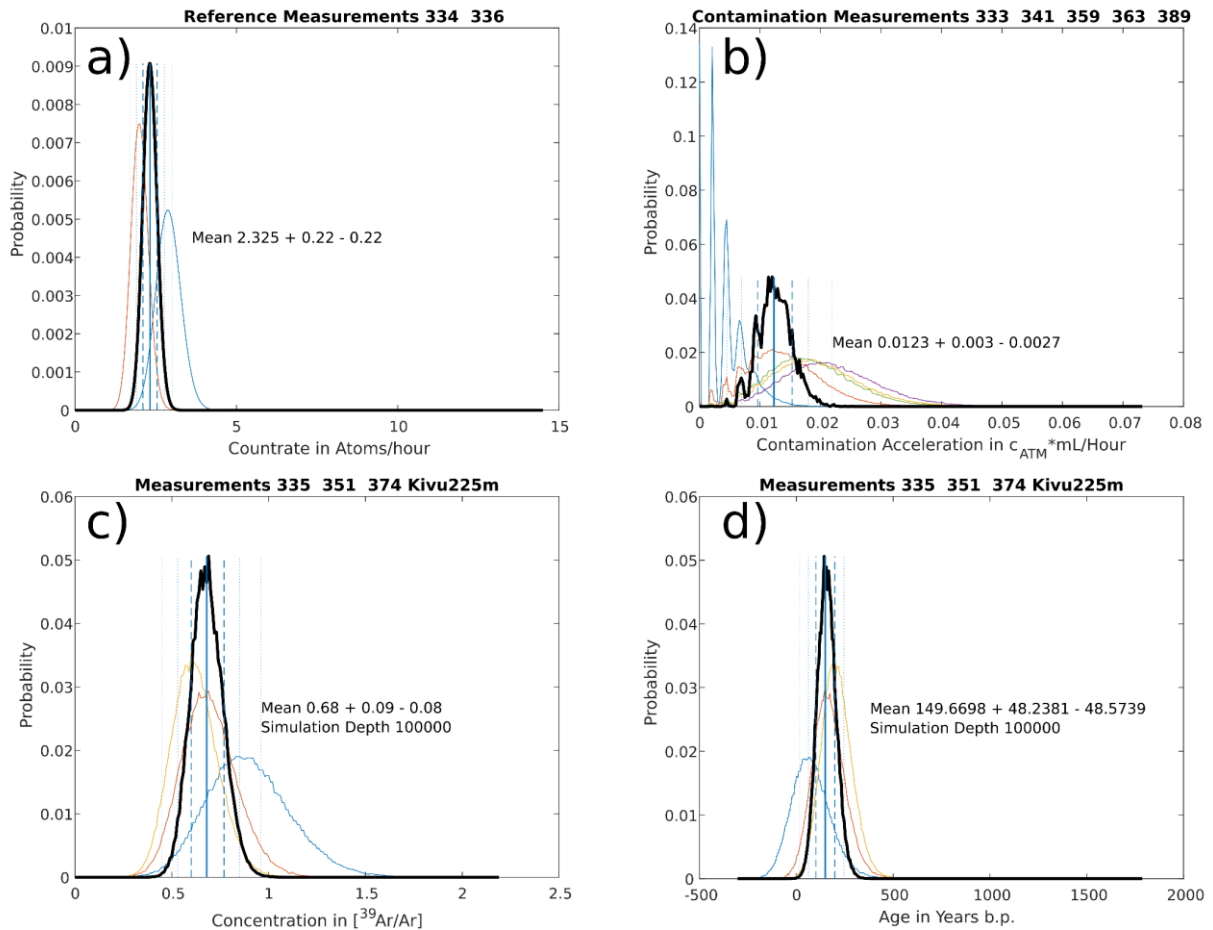

Figure 20: The relevant probability distributions for the exemplary data point at 225m in Lake Kivu. The vertical blue line in all graphs give the most probable value and the dashed and dotted lines the 1σ, 2σ and 3σ boundaries. a) The combination of the two reference measurements for measurement [335]. The reference count rate r_0 for this measurement is $2.33^{+0.22}_{-0.22}$ atoms/hour. b) The combined relevant contamination acceleration. The spikes in the blue distribution come from the transformation of a discrete histogram into a continuous probability distribution. c) The ^{39}Ar concentration at depth 225m determined by the three single measurements [335, 351, 374]. Simulation Depth 100000 describes the amount of Monte-Carlo simulations. The higher the Simulation count, the smoother the resulting curve. d) The tracer age directly calculated from c).

The graphical output is saved as a pdf file and as a MatLab figure file. All calculated results, intermediate results and distributions are saved as well. When starting one of the aforementioned functions, they automatically check the database, whether or not one of the necessary calculations has been done already and if so, loading the results instead of generating them again. Especially when working with high numbers of Monte-Carlo simulations (e.g. >10^5), this can reduce calculation times tremendously.

4. First ^{39}Ar analysis of lake water

The following chapter presents the first measurements of gas and water samples from gas-rich water bodies using ArTTA. The structure of this chapter is based on the structure of the corresponding paper manuscript, that will be submitted for publication in an international journal in the near future. In contrast to the planned publication, this chapter contains additional details regarding the sampling, the ArTTA measurements and additional work inferring a transit time distribution for Lake Kivu.

4.1. Abstract

We report the first ^{39}Ar concentration measurements of lake water using the quantum physical method of Argon Atom Trap Trace Analysis (ArTTA). ArTTA is a radioisotope detection method suitable for dating within a time range of 50 – 1000 years with ^{39}Ar. The aim was to use ^{39}Ar as a dating tracer, elucidating the lake's hydrodynamics, especially its suspected very long deep water residence times. In the sampled depth profile reaching up to 430 m deep, we unexpectedly found highly enriched ^{39}Ar concentrations at depths of 280 m and 350 m, namely $\left[^{39}\text{Ar}/\text{Ar}\right]_{280m} = 4.82^{+0.64}_{-0.41}$ R_A and $\left[^{39}\text{Ar}/\text{Ar}\right]_{350m} = 2.58^{+0.27}_{-0.24}$ R_A (with $R_A = \left[^{39}\text{Ar}/\text{Ar}\right]_{atm} = 8.1 \times 10^{-16}$), interfering with the use of ^{39}Ar as a dating tracer. However, using the 1D lake model Simstrat, we used the measured data to infer the ^{39}Ar concentrations of the lake's known groundwater intrusions. According to these simulations, two of these intrusions at 310 m and 330 m depth are especially notable, carrying ^{39}Ar concentrations of $\left[^{39}\text{Ar}/\text{Ar}\right]_{310m\ GW} = 27^{+2}_{-3}$ R_A and $\left[^{39}\text{Ar}/\text{Ar}\right]_{330m\ GW} = 22^{+2}_{-2}$ R_A. To our knowledge, these are the highest ^{39}Ar concentrations in water described so far. This work introduces ^{39}Ar measurements and dating for limnological research and offers novel insights into radioisotope production in volcanic groundwater systems. Lake Kivu, a lake on the border between the Democratic Republic of the Congo and Rwanda, is a meromictic lake highly influenced by strong volcanism. Its high CO_2 and CH_4 gas content (>65 mmol/L and >15 mmol/L for depths >250 m) poses both the possibility for commercial exploitation and a fatal danger for the about 2 million residents on its shoreline. A better understanding of Lake Kivu's hydrodynamics, solute-dynamics and the stability of the water column is crucial to recognize the potential and the hazards the lake's gas could represent.

4.2. Introduction
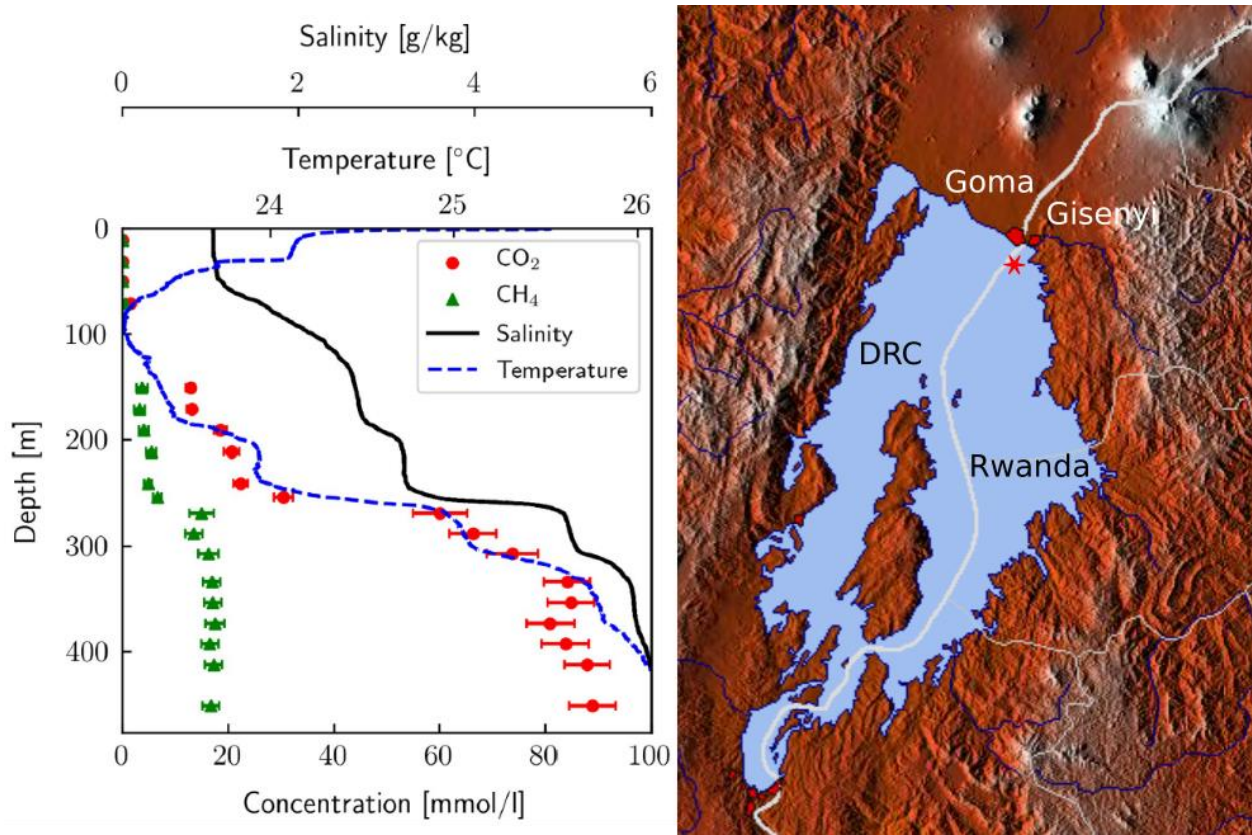
Figure 21: CTD Profile and map of Lake Kivu along the border of Rwanda and the Democratic Republic of the Congo (DRC). The red star marks the sampling point, a raft, permanently anchored 5 km south-west of Gisenyi, with a local depth of 412 m. The CTD and gas profiles are according to (Bärenbold et al. 2020b).

Lake Kivu is a meromictic lake at the East African Rift, straddling the border between Rwanda and the Democratic Republic of the Congo (DRC). It is strongly influenced by volcanism, most prominently by the active Mt. Nyiragongo at its northern shore. Its strong salt-stabilized stratification below a depth of 70 m is a result of several subsurface groundwater intrusions, also carrying large amounts of gas, mainly carbon dioxide (Descy et al. 2012; Bärenbold et al. 2020b). The anoxic deep water favors the microbial decomposition of CO_2 to methane (Descy et al. 2012), resulting in the lake's water containing up to 90 mmol/l CO_2 and up to 17 mmol/l CH_4 (Tassi et al. 2009; Bärenbold et al. 2020b)(see Figure 21). Gas rich deep water bodies of meromictic lakes are known for bearing the risk of limnic eruptions, a quasi-instantaneous release of the majority of the dissolved gasses, endangering all oxygen-dependent life in its proximity. Such catastrophes have occurred previously in 1984 and 1986 in Cameroon at the lakes Monoun and Nyos, causing thousands of casualties (Kling et al. 1987; Kling et al. 2005). A similar event at the much larger Lake Kivu with the big city of Goma at its shore could have an even more severe impact. This risk is especially high, since such events can be triggered by a strong disturbance in the water column. The cause of the eruptions at lakes Nyos and Monoun are not completely clear but subsurface landslides or small volcanic eruptions at the lake floor are discussed. There

is potential for both scenarios to occur at Lake Kivu as well, especially when consideringpast local events like the flow of a large amount of lava from the nearby volcano Nyiragongo into the lake in 1977 and 2002 (Tedesco et al. 2007; Lorke et al. 2004; ALLARD 2002). Smaller eruptions where the superficial lava did not reach the lake have happened even more often, the last one in May 2021 (OCHA 2021). On the other hand, the dissolved methane in Lake Kivu represents a precious energy resource for the region (Boehrer et al. 2019; Doevenspeck 2007).

An assessment of the risk of gas eruptions and the potential of the methane resource at Lake Kivu requires a good understanding of the lake's hydrodynamics. In particular, the residence time of gasses and water in the deep, stratified layers is important to estimate gas fluxes and possible changes in the gas concentrations over time. It has been hypothesized that the residence time of the deepest water is around 1000 years (Schmid et al. 2005). Such an age would be exceptionally high for lakes but comparable to residence times in the deep ocean. An ideal tool for direct radiometric dating in this age range is the very rare noble gas radioisotope ^{39}Ar with its half-life of 269 years (Loosli 1983; Lu et al. 2014).

Here, we present results of investigating Lake Kivu's hydrodynamics using the radioisotope dating method ^{39}Argon Atom Trap Trace Analysis, ArTTA. The isotope ^{39}Ar is mainly of cosmogenic origin with an approximately constant atmospheric abundance of $[^{39}\text{Ar}/\text{Ar}]_{atm} = R_A = 8.1 \times 10^{-16}$. This extremely low abundance makes ^{39}Ar difficult to measure. ArTTA is a new measurement method, based on techniques from atom physics, which was already successfully applied to several hydrological and glacial systems (Ritterbusch et al. 2014; Ebser et al. 2018b; Feng et al. 2019b). This work shows the first application of an ArTTA measurement to gas-rich water bodies. The method utilizes the quantum mechanical isotope shift in combination with resonant multi photon scattering in a magneto-optical trap (MOT) to achieve a perfect isotopic separation of ^{39}Ar and reliable measurements of ^{39}Ar/Ar ratios down to the 10^{-16} abundance level. The ^{39}Ar isotopic abundance in a sample is determined via the detection rate of single ^{39}Ar atoms in the MOT and its comparison with the count rate for a standard sample of known abundance. The precision of a measurement is determined mainly by the counting statistics of the detected atoms.

Dating of surface water and groundwater by using ^{39}Ar as a tracer is based on equilibrium with atmospheric Ar at the surface, radioactive decay in deeper layers isolated from the atmosphere and additional sources of ^{39}Ar. Several studies have shown that Lake Kivu has important subsurface groundwater inflows, leading to a general upwelling water circulation (Schmid et al. 2005). This inflowing groundwater affects the dissolved Ar in the deep water, which has to be taken into account for the interpretation of ^{39}Ar abundances in Lake Kivu. To model the effects of vertical mixing, groundwater inflows, and radioactive decay, we use an existing dynamic model of Lake Kivu, which is based on the 1D modelling software Simstrat (Bärenbold 2020a). With this model and the measured ^{39}Ar profile in the lake, we can determine the ^{39}Ar abundance in the subsurface groundwater discharges and thus obtain insights both on the origin and properties of the groundwater as well as the dynamics of argon as a solute in the lake. This approach became especially important in light of our

unexpected finding of [39]Ar abundances far above the atmospheric level in the deepest layers of the lake, which can only be explained by a strong influence of underground production of [39]Ar in some of the groundwater intrusions.

4.3. Sampling

The measured samples were gathered in two field trips, conducted in March 2018 and during a targeted re-sampling for [39]Ar in June 2019. On the lake, at the coordinates 1°44'20.9"S 29°13'46.2"E, a float is anchored, from which all of our samples were taken. The float is property of the Lake Kivu Monitoring Program (LKMP), which is part of the Rwanda Environment Management Authority (REMA).
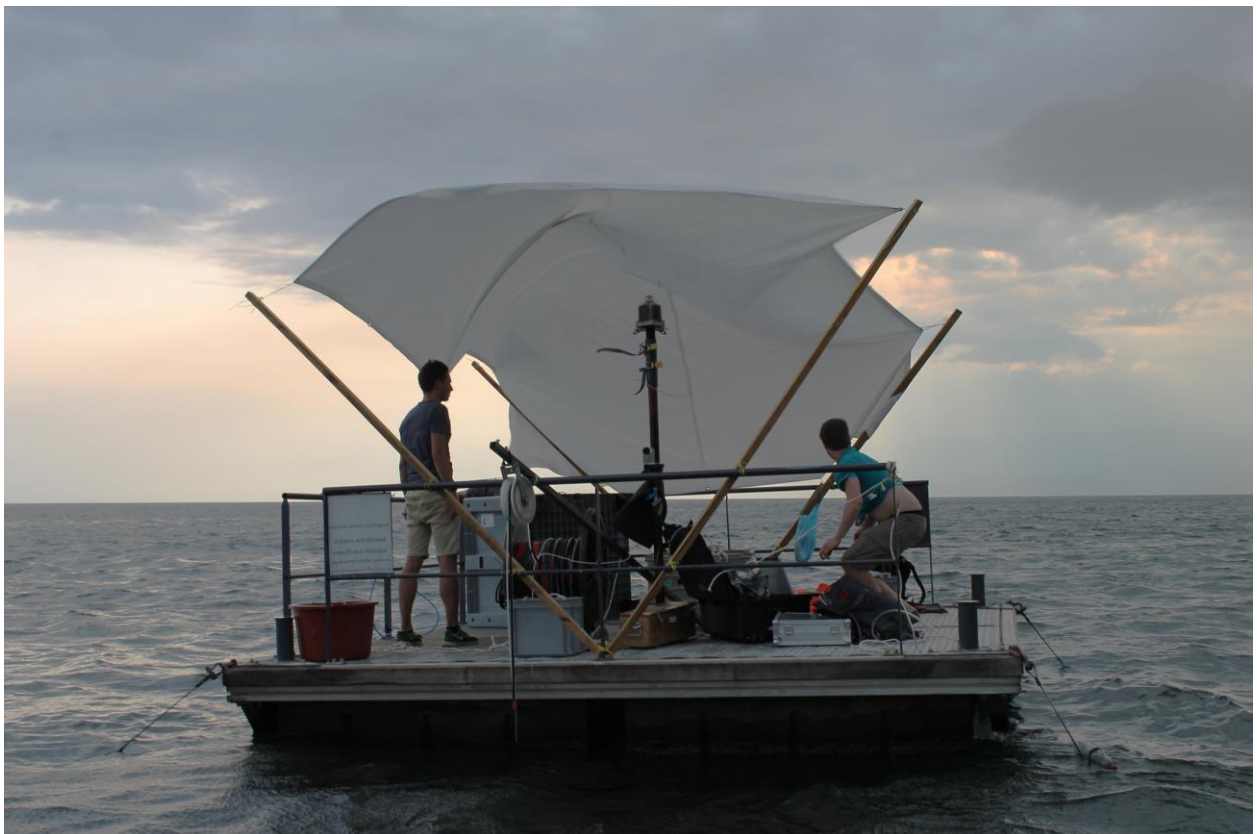
Figure 22: Sampling on Lake Kivu in March 2018 together with Fabian Bärenbold, Reto Britt and Michael Plüss from EAWAG Kastanienbaum (Switzerland). The weather conditions were good in the morning, but became worse every day around 2 pm, at which time this picture was taken. Working on the lake between 6 am to 1 pm is advisable.

Two different techniques were used for samples taken above and below the strong gas pressure gradient at 250 m, respectively.

For samples taken above 250 m, we used a submersible pump (0.75 kW submersible centrifugal pump, UG-18 from Pumpen Lechner) attached to both a 250 m cable and PE tube (10 mm diameter). This combination led to a 1.6 L/min pumping speed. After rinsing the tube volume twice (about 25 min), the pumped water was led through a T-piece attached to a 27 L pre-evacuated commercial propane gas bottle and a 2 m long clear PVC tube (see Figure 23).The bottle was opened carefully, so that a part of

the pumped water could flow into the bottle. The PVC tube was used to monitor the water flow. Care was taken to guarantee that no backwards leakage into the sampling container occurred. When the pressure in the bottle reached atmospheric pressure, it was closed and typically contained 20 – 25 L of water, depending on the gas content of the sampled water.
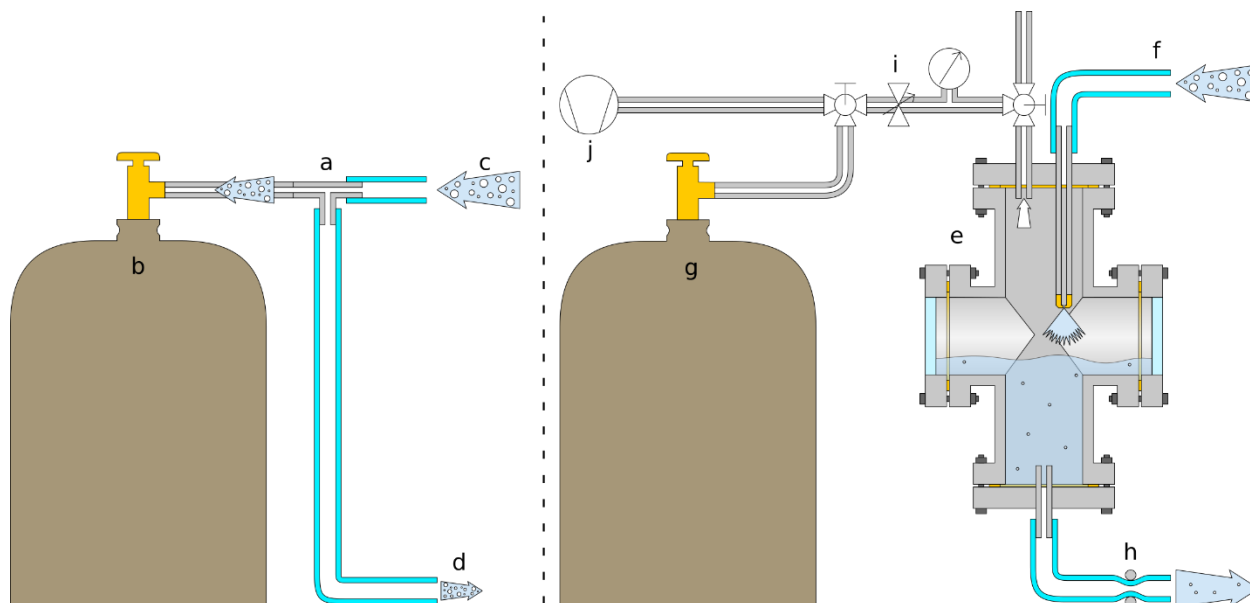

Figure 23: Schematics of the sampling setups for water with low or medium gas concentrations above 250 m and for gas rich water sampled below 250 m. Left: For low gas concentrations, our standard sampling method for water was used as described previously (Kersting 2018; Rädle 2019). A T-piece (a) is attached onto a pre-evacuated steel bottle. The pumped water is guided through said T-piece along a 2 m long clear PVC hose. The bottle is slowly opened, so that some of the water flow is directed into it. By monitoring the water flow in the clear outlet tube, we ensure no backwards leaking of air. Right: Center of the system for high gas pressure water is a stainless-steel spray chamber (e) with metal gaskets and two windows. The self-sustained flow of gas-rich water (f) is guided into the chamber and sprayed through a nozzle, creating a large surface area to enhance the phase separation. The gas phase is then guided towards a pre-evacuated 27 L bottle (g). By tuning the output throttle (h) and the needle valve (i), an overpressure in the chamber can be built up and the water level in the chamber can be stabilized. Prior to sampling, the whole setup is evacuated with a membrane vacuum pump (j) and the chamber is flushed with water.

At depths below 250 m, the CO_2 and CH_4 content of Lake Kivu is very high and thus, the previously described method is not applicable. Furthermore, due to the enormous dilution of dissolved atmospheric gasses in the water by CO_2 and CH_4, the relative amount of argon in the gas phase is rather small. Based on measurements from the first campaign (Bärenbold et al. 2020c), the volumetric fraction of Ar is as low as about 0.01 % for the deepest layers. As this mixing ratio is far lower than in atmospheric air (0.934 %), the risk of air contamination is enhanced for the sampling of Ar from the deep water. Therefore, the strategy was changed towards directly separating the gas from the water phase and compressing it into a 27 L steel bottle. The aim is to reach a pressure of about 1.5 bar in the container, which is equivalent to 40 L of gas at STP conditions, yielding > 400 µl of pure argon. In 2018, this was realized using an acrylic

spray chamber (Bärenbold et al. 2020c) and a compressor to fill the sample containers. This method, especially the use of a compressor, introduced leaks into the system and led to air contamination. Therefore, a new, airtight setup was built, in which the phase separation is achieved in a stainless steel spray chamber (see Figure 23 and Figure 24) with steel tubing and high grade metal gaskets. The whole setup was tested for helium leaks before the sampling campaign.

Figure 24: Picture of the spray chamber sketched in Figure 23. The construction was attached to the raft's mast to reduce the influence of wave movements. The needle valve (in the front) and the sampling container are also shown.

To generate an overpressure in the chamber during sampling, the outflow was restricted by an adjustable clamp. Using this clamp and a fine needle valve, the gas flow into the sample container was regulated to hold the water level stable at all times. This was done by monitoring the water level on the window of the spray chamber by eye. With this setup, pressures of 1.5 bar could be achieved. The whole setup was evacuated and flushed with lake water before each sampling.

4.4. Sample preparation

The collected samples were processed further in the gas extraction and separation lab at the Institute of Environmental Physics of Heidelberg University (IUP). The sample preparation device is shown in Figure 25. The argon is separated by removing all reactive gasses with two titanium sponge getters at 900°C and at room temperature, respectively, leaving only the noble gasses, which are mostly (>99%) pure argon. The process has been described in detail elsewhere (Ebser et al. 2018b; Feng et al. 2019b; Beyersdorfer 2016) and in the caption of Figure 25.

In addition to the described standard procedure, three additional steps were necessary to cope with the high amounts of H_2S, CH_4 and CO_2 in the samples from Lake Kivu: The corrosive H_2S was removed by guiding the gas through a chamber filled with fine copper wool at a temperature of about 100 °C. In combination with abundant moisture, needed as a catalyst, the H_2S reacts with the copper by forming copper sulfide ($Cu + H_2S \rightarrow H_2 + CuS$). The CH_4 reacts with CuO at 900°C to CO_2, Cu and H_2. The CO_2 is then trapped in a liquid nitrogen-cooled, naked stainless-steel trap together with H_2O. Subsequently, the resulting gas mixture resembles usual air-like samples and can be handled further as usual.
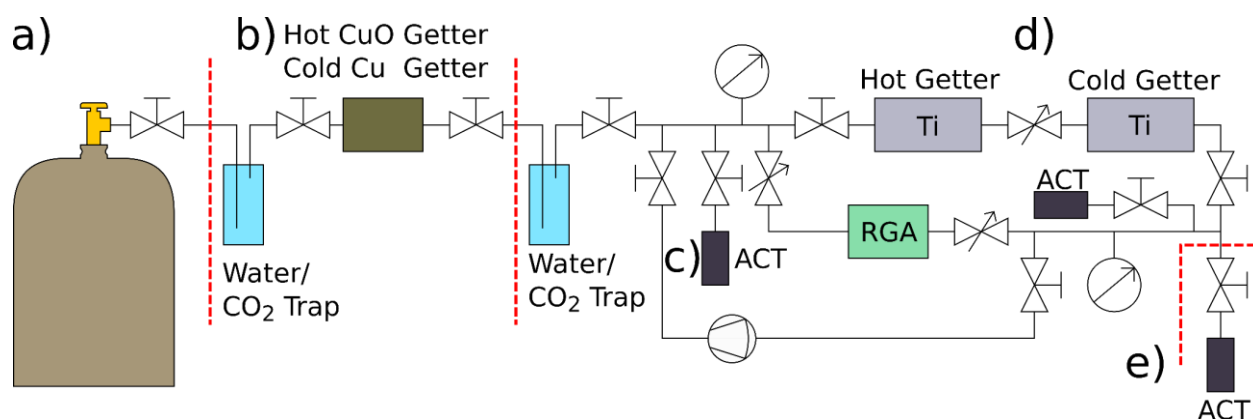

Figure 25: Sketch of the [39]Ar preparation line built by Stefan Beyersdorfer (Beyersdorfer 2016) and extended in this project. a) The sample container is attached to the machine. The gas from its head space is pulled into an activated charcoal cryo-trap (ACT) c). During this pull, the gas passes section b) comprised of two liquid nitrogen-cooled naked steel traps, a cold copper wool getter and a hot copper(II) oxide (CuO) getter. In the steel traps, CO_2 and water vapor condense. The cold copper wool chemically binds H_2S and the hot CuO reacts with CH_4. Section b) was added in this project to account for the gas composition of Lake Kivu. After processing and trapping all the gas from a) on the first ACT c), the remaining gas is pulled through a hot and a cold titanium sponge getter d) onto the final ACT e). The hot titanium is highly reactive and will chemically react to most reactive components of the gas except hydrogen. The cold titanium, however, adsorbs the hydrogen on its surface due to van-der-Waals interactions. The processed gas is >99.6% pure argon in the end. The final ACT e) is detachable and used as the sample container for the processed sample, as it can be attached directly to the ATTA machine. Figure 26 shows a picture of such a sample container.

Figure 26: Sample container for argon samples of a volume typically below 5 mlSTP. The container can be attached directly to the ATTA machine using a Swagelok ¼'' VCR connector. The high-quality bellow valves are operated exclusively with 1.4 Nm torque wrenches.

4.5. Simstrat model and fitting

Lake Kivu has previously been modelled using the one-dimensional hydrodynamic lake model Simstrat coupled to the biochemical library AED2, as set up and described by (Bärenbold et al. 2021). The model simulates vertical diffusive (including the effects of double-diffusion) and advective transport of dissolved gasses in Lake Kivu and has been extended to also simulate the concentration of ^{39}Ar.

The simulations were done using the computational power of the bwUniCluster 2.0 system provided by the Steinbuch Centre for Computing (SCC) at Karlsruhe Institute of Technology (KIT). All simulations were performed using the following parameters: At least 1000 years of simulation time with a resolution of 5 minutes per computed step. The simulations differ only in the ^{39}Ar isotopic abundance of the groundwater intrusions, the initial conditions of ^{39}Ar present in the lake and, for the purpose of an assessment of the dynamics of ^{39}Ar in the water column, the radioactive decay switched on or off.

The results are vertical profiles for all the simulated properties in pre-determined time steps, which were further analyzed using MatLab 2020b. The convergence of the resulting ^{39}Ar profiles was investigated to determine the time that the system needs to reach a steady state. Only equilibrated ^{39}Ar profiles were used in our analyses, based on the finding that gas concentrations in the lake currently are approximately at a steady state (Bärenbold et al. 2020b). The resulting ^{39}Ar profiles were compared to our measured values and the deviation was quantified by calculating χ^2, the sum of the error-weighted squared differences between measured and modeled abundances. The fit was optimized (i.e. χ^2 was minimized) manually using the following

procedure: For each optimization step, the inflow parameters were varied in pairs of two with 10 different values for each, resulting in 100 simulations per optimization step. Subsequent χ^2 analysis led to a global minimum around which a finer step size could be applied. In total, we varied five (plus two) parameters, namely the inflow concentrations at 143, 310, 330, 400 and 430 m depth and, to a lesser extent, the inflow concentrations at 190 and 253 m.

4.6. Results
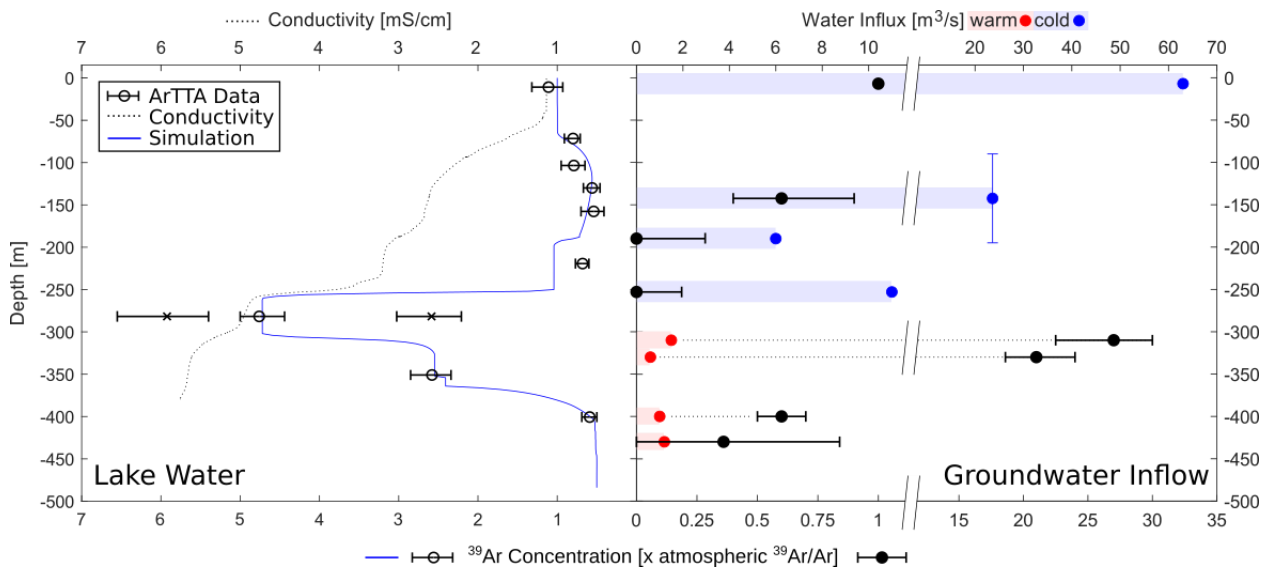
Figure 27: Vertical profiles of ^{39}Ar in the lake and in groundwater inflows. Left: Measured and modelled profiles in the lake. Note that the x-axis is inverted, in order to visualize how abundances in the lake mirror those in the inflow shown in the adjacent panel. ^{39}Ar isotopic abundance relative to atmospheric RA, as measured by ArTTA in lake water, are depicted as black circles, the individual measurements at 280 m as black x. In blue, the best fit result of the SimStrat Simulation is shown. The black dotted line was added for orientation and displays the conductivity. Right: The modelled water influxes and a qualitative measure for the springs' respective temperatures are shown as blue and red bars. The spring centered at about 145 m represents an inflow distributed over a depth range, while the other inflows are point sources. The black dots represent the ^{39}Ar concentration of the groundwater infiltration. These values were deduced from the best fit simulation shown in a).

4.6.1. ^{39}Ar measurements with ArTTA

The ^{39}Ar isotopic abundances deduced from the ArTTA measurements are presented in Table 5 and Figure 27 left respectively. The atom count rates of those measurements are summarized in Figure 28. The uncertainty of the single measurement follows mainly from the statistical errors of the samples and the adjacent reference measurements under the assumption of a Poisson distributed expectation value using a Bayesian analysis. For combined measurements, the single results are also combined, following a Bayesian calculus. All calculations were performed according to standardized procedures described previously (Ebser 2018a). For all depths, except for 280 m, the measurement replicates were in good agreement with each other or

were comparable to adjacent depths in those cases where only single samples were measured. At the depth of 280 m, the significant discrepancy of the measurements conducted on duplicate samples raises concerns of mistakes made during the measurement, sample preparation, or sampling. To the best of our knowledge, errors in the measurement are very unlikely since no irregularities could be observed in the real time monitoring of the measurement, nor in the measurements' overall quality. Hence, an air contamination either during sampling or during sample preparation is suspected. Since a contamination by air leads to a shift in the measured ^{39}Ar abundance towards the atmospheric value (1 R_A), we assume the higher measured concentration to be the more reliable data point. But since we cannot exclude measurement errors completely, we present all three possible variants: Exclusion of either of the single measurements and the combination of them. If not otherwise mentioned, we refer to the approach using the combination of these values.

Sample Name	Sampling Date	Depth	Running Number	Measurement Date	Measured ^{39}Ar isotopic abundance [xR_A]	Combined ^{39}Ar isotopic abundance (if applicable) [xR_A]	Tracer Age [years b.p.]	Ar Volume [ml$_{STP}$]
Kivu_75m	11.03.2018	75 m	213	21.11.2018	0.84 +0.14 -0.13		69 +60 -63	1.7
Kivu_130m	11.03.2018	130 m	230	02.12.2018	0.56 +0.11 -0.10		225 +76 -70	1.3
Kivu225m2	09.07.2019	219.3 m	335	21.08.2020	0.89 +0.23 -0.19		47 +94 -90	1.3
Kivu170m	08.07.2019	157.7 m*	343	25.08.2020	0.54 +0.16 -0.13		239 +107 -101	1.6
Kivu130m	08.07.2019	103.5 m*	349	28.08.2020	0.79 +0.16 -0.14		91 +76 -72	1.3
Kivu225m1	09.07.2019	219.3 m	351	29.08.2020	0.68 +0.15 -0.13		148 +82 -77	1.3
Kivu400m3	12.07.2019	400.6 m	353	30.08.2020	0.51 +0.16 -0.13		263 +114 -103	1.3
Kivu70m	08.07.2019	72 m	355	01.09.2020	0.76 +0.17 -0.15	0.80 +0.10 -0.10	105 +82 -78	1.2
Kivu10m	08.07.2019	10.9 m	357	02.09.2020	1.12 +0.20 -0.19		-44 +107 -74	1.3
Kivu280m1	10.07.2019	281.7 m	361	04.09.2020	2.72 +0.42 -0.35		-388 +54 -56	1.3
Kivu225m2	09.07.2019	219.3 m	374	21.09.2020	0.61 +0.13 -0.12	0.69 +0.09 -0.08	190 +81 -72	1.3
Kivu280m2	10.07.2019	281.7 m	376	22.09.2020	5.93 +0.60 -0.54	4.82 +0.64 -0.41**	-691 +37 -37	1.2
Kivu400m1	12.07.2019	400.6 m	378	23.09.2020	0.81 +0.27 -0.25		84 +144 -112	1
Kivu350m2	11.07.2019	350.9 m	381	28.09.2020	2.60 +0.35 -0.32		-370 +51 -49	0.7
Kivu400m3	12.07.2019	400.6 m	384	29.09.2020	0.62 +0.15 -0.14	0.59 +0.1 -0.09	184 +99 -84	0.6
Kivu350m1	11.07.2019	350.9 m	386	30.09.2020	2.64 +0.42 -0.36	2.58 +0.27 -0.24	-376 +57 -57	1.2

Table 5: ^{39}Ar concentrations of the samples determined by ArTTA. The asymmetrical error of the concentration measurements comes from the skewness of the Poisson distribution. *These samples have a different depth than intended, thus the discrepancy in naming. We suspect a disturbance of our sampler with a fishing net. An attached CTD probe gave the correct sampling depth. **As discussed, the single measurements differ significantly. Thus, a combination of both measurements probably does not represent in situ conditions.

For depths between 70 and 220 m and below 350 m we find ^{39}Ar concentrations between 0.8 to 0.55 R_A, which would correspond to apparent ^{39}Ar ages of 87 to 232 years. Since the transport processes within the lake are dominated by advection resulting from upwelling, any atmospheric ^{39}Ar signal is disturbed by the enhanced ^{39}Ar signal at 280 and 350 m, with values between 5.88 and 2.57 x R_A. Thus, a model-based analysis is necessary to derive reliable residence time information.
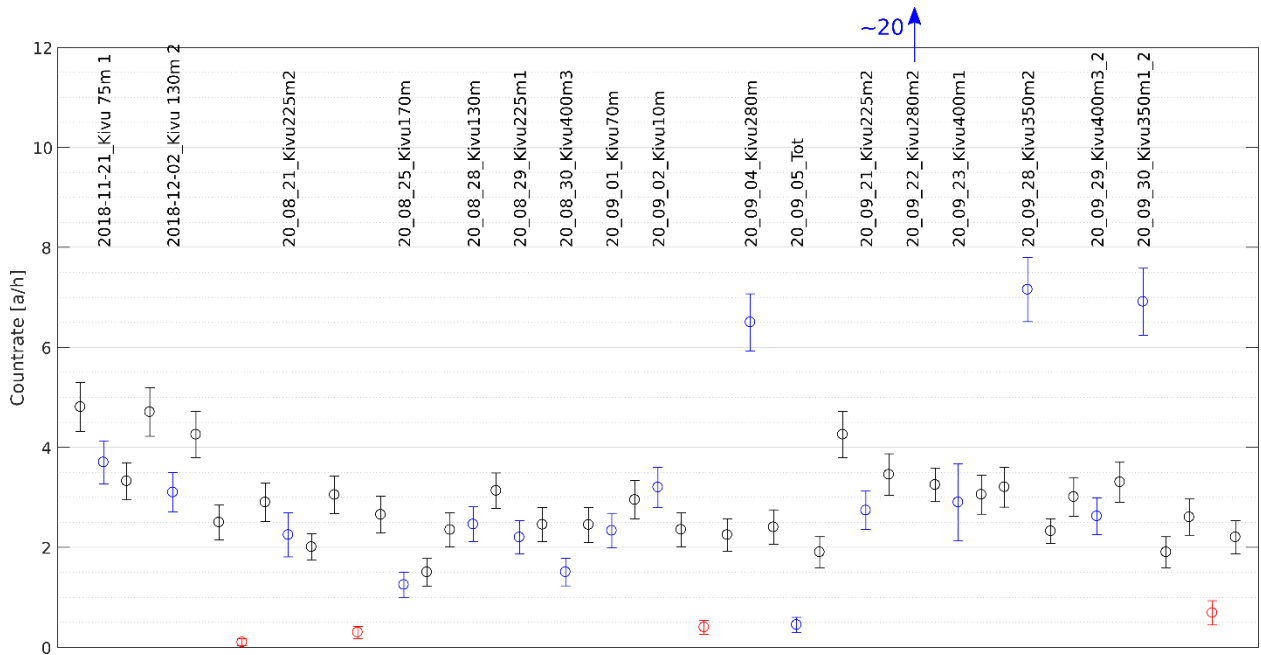
Figure 28: Summary of the count rates measured in all Lake Kivu samples (blue) with their respective references (black) and the relevant background measurements with ^{39}Ar-free argon (red).

4.6.2. Simstrat simulations

The ^{39}Ar isotopic abundances in the lake measured by ArTTA were fitted using Simstrat by varying exclusively the ^{39}Ar isotopic abundances of the numerous inflows. All other model parameters (such as inflow volume, temperature, salinity or the model's boundary conditions like meteorological or biochemical activity) were fixed to the optimized values determined by Bärenbold (Bärenbold 2020a). The simulation results are depicted in Figure 27 Right and in Table 6.

The ^{39}Ar concentrations of the inflows were inferred by varying the concentrations of the inflows whilst minimizing χ^2, the error weighted difference between the simulation results and the measured ^{39}Ar isotopic abundances. The errors were determined by fitting both the measured values plus and minus their respective one sigma uncertainties. As will be discussed later, the model does not sufficiently describe the measured ^{39}Ar isotopic abundance at 219 m, which is lower than the model results. Therefore, the ^{39}Ar concentrations of the inflows at 190 and 253 m were set to zero. In order to determine an error value for the ^{39}Ar inflow at 190 and 253 m, the ^{39}Ar inflow was varied and a χ^2 exclusion criterion of $\chi^2 < 5$ was applied, which corresponds to a fitting problem with 5 – 6 degrees of freedom, . The ^{39}Ar abundance at 219 m was excluded from the χ^2 analysis.

With the Simstrat results, we find that the inflows at 310 and 330 m depth hold highly enriched ^{39}Ar concentrations of 27 and 21 times R_A, respectively, while the other springs feature concentrations below R_A.

50

Source	Volume Flow [m³/s]	³⁹Ar Concentrations [R_A]			T [°C]	S [g/kg]
Depth [m]		280 m Combined	280 m 1	280 m 2		
Surface	63	1	1	1	21.5	0.1
90 - 195	23.6	0.6 + 0.3 -0.2	0.8 ± 0.3	0.4 ± 0.3	21	2.2
190	6	0 + 0.3 -0	0.1 + 0.3 -0.1	0 + 0.1 - 0	21	2.2
253	11	0 + 0.2 -0	0.1 + 0.3 -0.1	0 + 0.1 - 0	22.6	2.6
310	1.5	27 + 2 -3	13 + 1 - 3	22 ± 3	26	4.4
330	0.6	21 ± 2	26 ± 2	35 ± 3	26	5.6
400	1	0.6 ± 0.2	0.6 ± 0.2	0.7 ± 0.2	25.6	5.7
430	1.2	0.3 ± 0.3	0.3 ± 0.3	0.3 ± 0.3	25.7	6

Table 6. ³⁹Ar isotopic abundances in the groundwater intrusions deduced by variation of this parameter using the described Simstrat model. The parameters Volume Flow, Temperature and Salinity are taken from Bärenbold (Bärenbold 2020a) and shown for orientation. Three different results are shown, depending on which ³⁹Ar value was chosen for the two conflicting measurements in 280 m depth: both combined or one of the measurements on their own.

4.6.3. Simulation error

During preparation of this thesis, an error in the presented simulations was found regarding the simulated Ar flux into the lake. The simulation assumed an equal amount of total argon entering the lake at every depth. Hence, only the relative abundance ³⁹Ar/Ar in units of [xR_A] was simulated. Correcting this error was unfortunately too time consuming in the context of the timeline of this thesis, as a complete recalculation would require several weeks of server time. Although we know that our simulation results are flawed, we have reason to assume that we can draw qualitatively equal conclusions.

Depth [m]	Ar
40	2.34E-04
78	2.40E-04
86	
98	2.36E-04
137	
167	2.19E-04
196	2.03E-04
213	1.96E-04
254	1.81E-04
273	1.22E-04
294	1.11E-04
337	1.11E-04
348	
368	1.18E-04
390	
408	9.41E-05
440	
Uncertainty	5%
ASW	2.46E-04

Figure 29: Total argon concentration in Lake Kivu in [ccSTP/g] (Bärenbold et al. 2020c).

Figure 29 gives an overview over the measured total Ar concentrations in Lake Kivu. It becomes clear, that the lower groundwater intrusions carry less argon. This error in our simulations becomes important when looking at mixing effects. The higher the argon amount of a mixing partner, the higher its influence on the mixture's concentration. This leads to the following conclusions:

- ► In mixing two layers, the influence of the layer with less argon has been overestimated. This might explain the discrepancy of the measured and the simulated ^{39}Ar isotopic abundance at 225 m.
- ► The influence of the inflow at 253 m to the layer between 253 m and 300 m has been underestimated. This might lead to even higher ^{39}Ar isotopic abundances for the inflows at 310 and 330 m.
- ► Below 254 m, the total dissolved argon changes only slightly. The simulation results for this area should therefore be quite reliable.

In order to fix this error in the presented simulations, they will be repeated independently by simulating ^{36}Ar, ^{39}Ar and ^{40}Ar concentrations.

4.6.4. Transit Times

The 1D lake model described above is very powerful and it should enable us to extract what is known as a Transit Time Distribution (TTD). The concept of a TTD is a powerful tool to describe the dynamics of a hydrological system. Essentially, it is equivalent to the probability density function (pdf) of the age of an idealized infinitesimal volume of the system, while age can be defined in various ways, e.g. the time a water particle last had contact with the atmosphere. This concept is widely used in many hydrological disciplines (Sprenger et al. 2019) and in the following, a method to deduce a quasi TTD for solutes (argon as a proxy) in Lake Kivu using the modelled ^{39}Ar isotopic abundances will be presented. For the TTD discussed here, time zero represents the time a gas parcel enters the lake through one of the eight different intrusions.

Programming the 1D lake model was mainly done by Fabian Bärenbold and is described in his PhD thesis (Bärenbold 2020a). Technically, such a model should be able to create a TTD for the modelled system. For this, one would need to extend the model so that each water parcel has a parameter "age" which increases for each time step by exactly the time step and new water enters the system with an age of 0. Due to time constraints, however, a different route was chosen here. Several simulations were performed with the input of argon limited to one groundwater intrusion at a time (plus the atmospheric input at the surface) to get information on transit times. In doing so, the point-spread function of each defined argon input can be used to determine where in the water column it accumulates. In order to get additional time information, i.e. how long it took for the argon to get from its intrusion point to each point in the water column, the simulations are repeated using hypothetical stable ^{39}Ar$_{stable}$ that enters the lake and accumulates the same way the radioactive ^{39}Ar did. By creating the ratio of both, a mean apparent age α of the ^{39}Ar from each intrusion at each depth in the water column is calculated. This process is visualized in Figure 30

and Figure 31. It needs to be noted that only an apparent age is calculated with the presented method, not a real mean age. For the relation of the mean age of a system to an apparent age, see chapter 1.3.

Figure 30 a) and b) are showing the simulated isotopic abundance of ^{39}Ar over the water column, with a) presenting the hypothetical ^{39}Ar$_{stable}$ and b) the real, decaying ^{39}Ar. In c) the ratio of both is depicted and in d) the corresponding ^{39}Ar tracer age α according to $\alpha = 269\ y/\ln(1/2) \cdot \ln([^{39}Ar]/[^{39}Ar_{stable}])$ is shown. In order to assess how well equilibrated the water column is at each depth after a 2000 y-spanning simulation time , the change of apparent age per simulation time has been determined and is visualized in part e) of Figure 30. If the change in apparent age is smaller than 1 month per simulated year, the water column at this position was judged to be sufficiently equilibrated. This criterion was chosen as a compromise between precision and computation time. To simulate 2000 years, calculation times of 9 days were required. Therefore, the required calculation time to reach a significantly higher precision was deemed too excessive. If only the sufficiently equilibrated depths are taken into account, this results in the reliable values for a ^{39}Ar apparent age distribution shown as black circles in part f) of Figure 30. Notably, values between 400 – 120 m depth and also above 80 m were obtained this way. The latter one represents the influence of fresh water at the surface and will not be considered further here. In general, only values below 120 m will be discussed, as they are the only ones giving realistic information with the method presented here. The values between 400 and 120 m depth, on the other hand, show a clear transit time. A dominant motion of the argon upwards through the water column can be seen, consistent with the overall upwelling present in the lake. Figure 31 gives an overview of the transit times for all the argon entering the lake through the different intrusions.
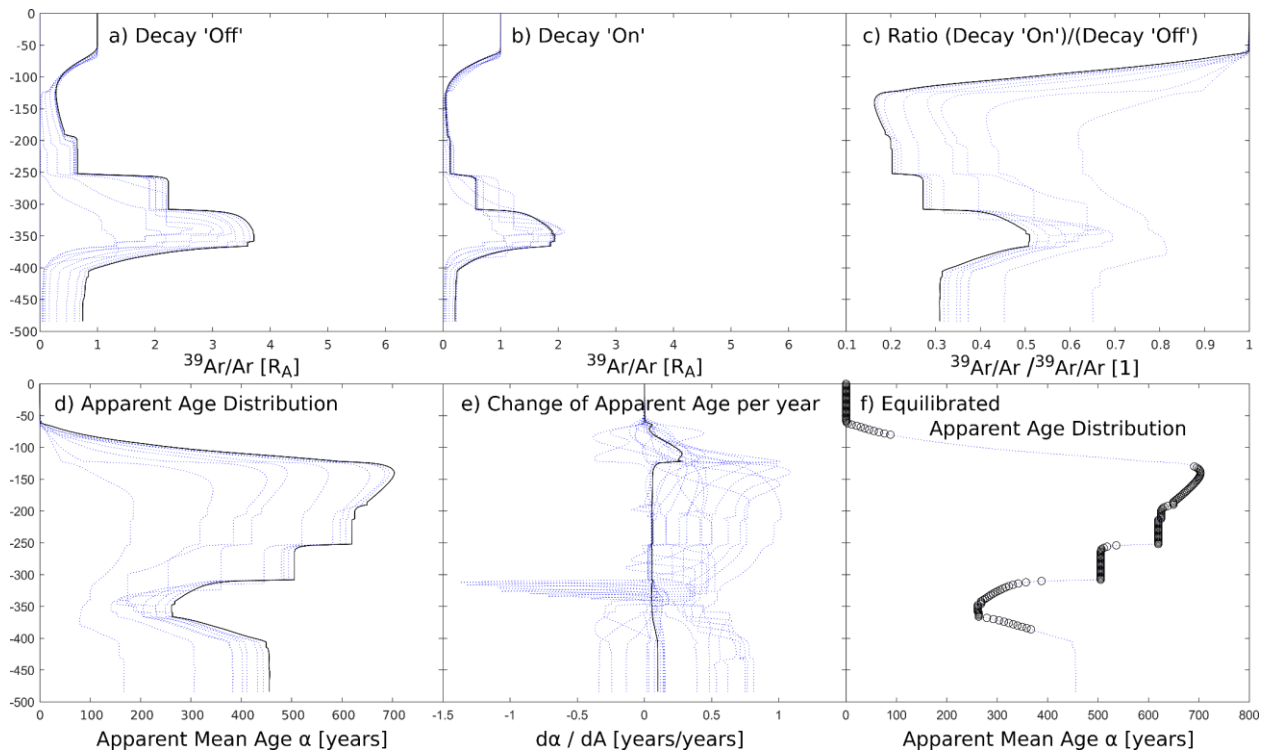
Figure 30: Apparent age calculation of ^{39}Ar in the water column of Lake Kivu, using the intrusion at 330 m as an example. All simulations cover a simulated time of 2000 years with a simulation time step of 5 min. The blue dotted lines represent intermediate results in 200-year-steps to visualize the convergence. a) & b) The ^{39}Ar isotopic abundance over the water column with hypothetical "stable" $^{39}Ar_{stable}$ and with real ^{39}Ar, respectively. c) Pointwise ratio of $^{39}Ar/^{39}Ar_{stable}$. d) The corresponding ^{39}Ar tracer-age or apparent age as a measure of equilibration e) The change of apparent age per simulated year $d\alpha/dA$, used as a measure of equilibration. f) The ^{39}Ar apparent age over the water column with the exclusion criterion: $d\alpha/dA < 0.08 \approx 1$ month/ 1 year.
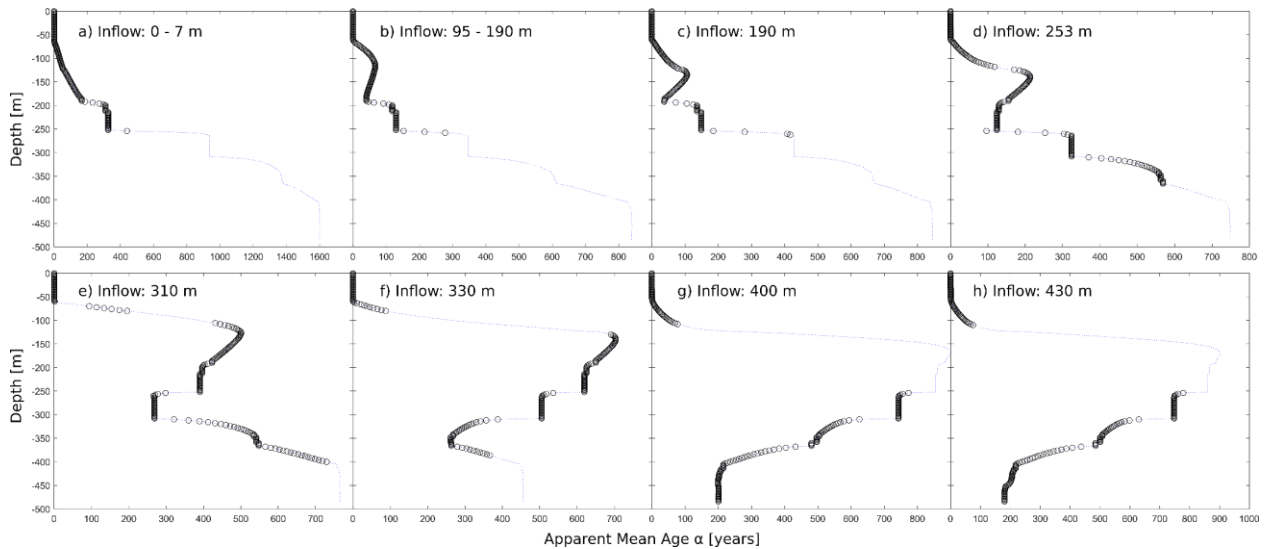

Figure 31: Reliable apparent age α equivalent to Figure 3 f) for all investigated intrusion depths. a) The inflow at 0 - 7 m represents the freshwater inflow at the surface.

Finally, in order to now deduce a full TTD for the lake, two steps need to be performed. The first is to repeat those simulations in which only one of the intrusions carries argon, but now, the argon flux at each intrusion is equal to one. Subsequently, the

54

aforementioned simulation with the hypothetical stable ³⁹Ar is performed and results in an argon concentration distribution which reflects the amount of argon at any depth that solely originates from a single intrusion.

The concentration distribution c of the inflow at depth D as a function of the height in the water column z:

$$c_{ArStable}^{D}(z)$$ <div style="text-align:right">*Equation 35*</div>

The total amount of argon $G(z)$ as a function of z and the normalized concentration distributions $\hat{c}^{D}(z)$ as visualized in Figure 32 a):

$$G(z) = \sum_{D} c_{ArStable}^{D}(z) \mid \hat{c}^{D}(z) = c_{ArStable}^{D}(z)/G(z)$$ <div style="text-align:right">Equation 36</div>

In the next step, the TTD $\Theta^{D}(z)$ can be defined as the percentage of contribution $\hat{c}^{D}(z)$ of each intrusion to each depth multiplied with the corresponding age of the argon $\alpha^{D}(z)$ from this intrusion at the corresponding depth. The TTD is visualized in colour scale in Figure 32 b).

$$\Theta^{D}(z) = \alpha^{D}(z) \cdot \hat{c}^{D}(z)$$ <div style="text-align:right">Equation 37</div>

In order to determine the mean transit time $\bar{\alpha}(z)$ of the argon at any depth, it should be considered that when two systems with two different ages are mixed, the ages are not mixed linearly, but the concentrations are. Therefore, the age distributions $\alpha^{D}(z)$

have to first be transformed into concentrations. Then, the mean needs to be created and finally, this mean has to be transformed back into an age:

$$\bar{a}(z) = \frac{T_{1/2}}{\ln(1/2)} \cdot \ln\left[\sum_D exp\left(\frac{\alpha^D(z)}{\frac{T_{1/2}}{\ln(1/2)}}\right) \cdot \hat{c}^D(z)\right]$$

This mean age $\bar{a}(z)$ is visualized as the red plot in Figure 32 b).
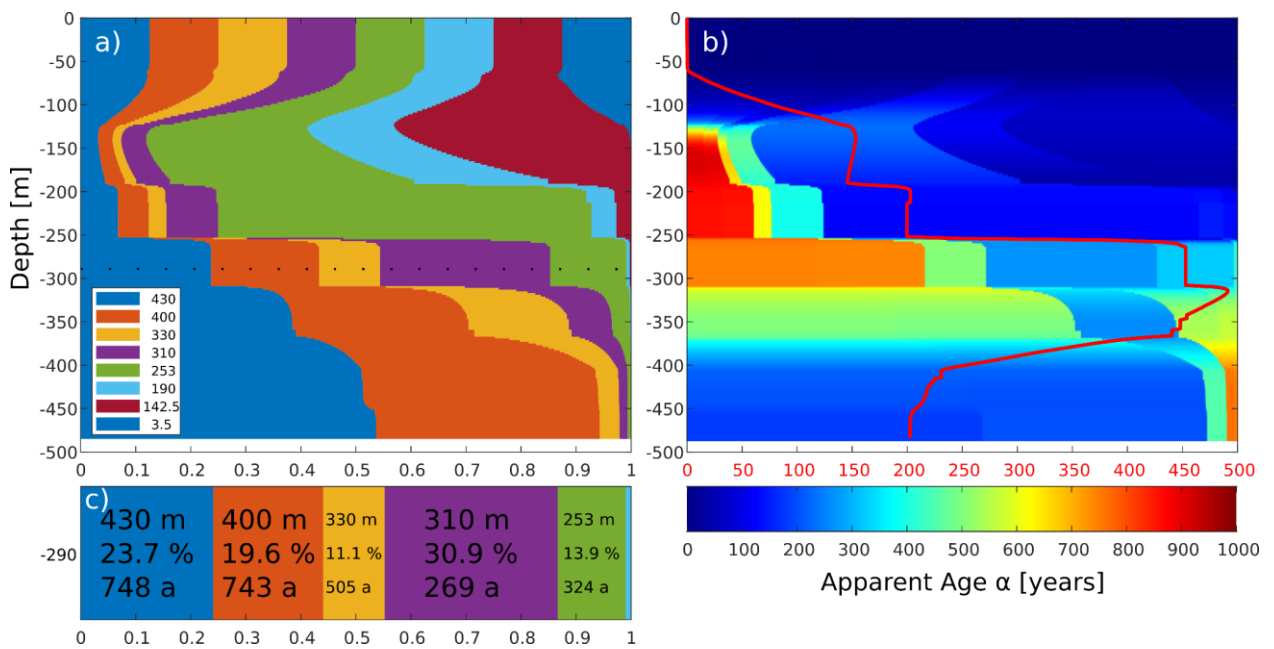
Figure 32: a) Relative contribution to the amount of total argon at any depth of the different intrusions. b) Similar to a) but in color scale representing the transit time distribution (TTD) of argon in the water column. The color scale represents the apparent age of the argon at each depth. The red curve is a measure of the mean age of the argon at each depth. c) For readability: Cut of graph a) at 290 m (dotted line). Here, the relative contribution of each intrusion with its respective apparent age is shown, the latter being equivalent to graph b).

For a final cross-check, the calculated mean apparent age can be compared to a very simplified model, i.e. the box flow model. The box flow model describes a system of connected boxes with inflow Φ, outflow φ and volume V. With a single box, a mean transit time τ through the box is given as:

$$\tau = V/_\Phi$$

Several boxes can now be connected together, representing the stratified water column. The flow is simplified from box to box by only allowing upwards flow, due to the strong advective upwelling motion. With this setup, a transit time distribution as shown in Figure 33 is obtained. The transit time at each depth is presented both in

real age and in apparent age under the assumption of a homogeneous and an exponential age distribution (compare chapter 8.1).
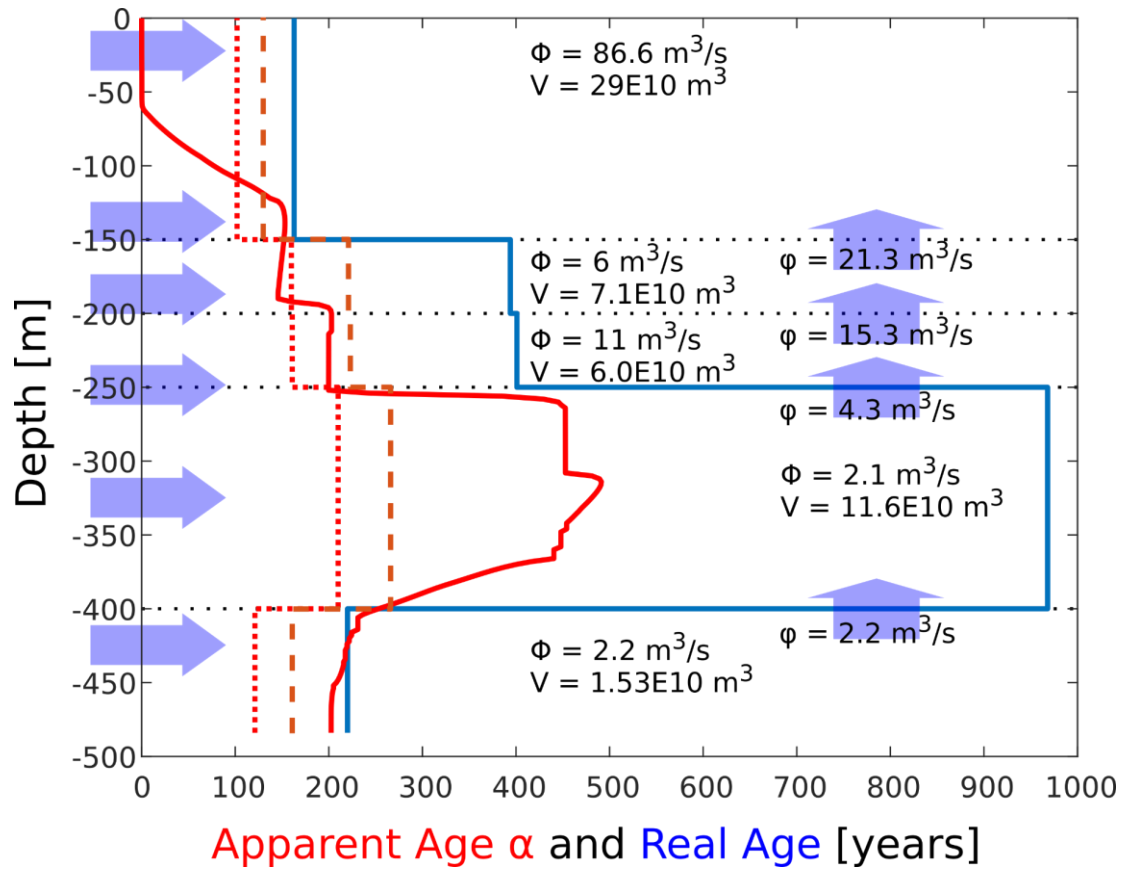

Figure 33: Comparison of the TTD calculated beforehand with a highly simplified box flow model. Each box has an inflow and an outflow, which acts as an additional inflow for the box above. The resulting mean transit time for the water in each depth is shown in dark blue. The TTD from Figure 32 b) is shown as a red solid line. The red dashed and dotted lines show the apparent age of the box flow model assuming a homogeneous age distribution (dashed) or an exponential age distribution (dotted), respectively.

The TTD calculated beforehand could not exactly be recreated with the overly simplified box flow model. This was to be expected, since it is highly simplified and e.g., no downwards flow is modelled and diffusion is not represented at all. It is remarkable, how closely this overly simplified model matches the much more complicated one. This suggests that the simple box flow model might actually be applicable to Lake Kivu for low resolution questions.

In summary, we were able to deduce a TTD for argon in Lake Kivu. However, care should be taken when interpreting the results, since the deduced TTD is not in units of real age but in units of apparent age, also called tracer age. This is caused by the fact that a mixing of two volumes with different ^{39}Ar concentrations always leads to an underestimation of the real age of the mixture, due to the non-linearity of the exponential decay. Thus, the apparent age is always younger or equal to the real age (also compare with Figure 5 in chapter 1.3). Furthermore, due to the influence of mixing and constant ^{39}Ar replenishment at the surface and the non-ideal setup of these simulations, only values below about 120 m are valid. Nevertheless, the inferred TTD

can give us a very good idea on the time scales at which the advective and diffusive processes in Lake Kivu are occurring.

4.7. Discussion

This work presents highly enriched ^{39}Ar concentrations, which were found in the very distinct vertical structure of Lake Kivu. Remarkably, this structure is distinct enough to be used to determine properties of the inflowing groundwater, in conjunction with the knowledge on these groundwater inflows derived from other tracers (Bärenbold 2020a). We find a vertically very localized inflow of groundwater with an extremely high ^{39}Ar concentration of up to 27^{+2}_{-3} R_A. This can be understood by looking at mechanisms for ^{39}Ar production other than cosmic rays (cosmic radiation-induced neutron spallation of ^{40}Ar ($^{40}Ar(n,2n)$ ^{39}Ar)(Loosli 1983)). ^{39}Ar can also be produced underground by neutron spallation of ^{39}K ($^{39}K(n,p)$ ^{39}Ar) (Šrámek et al. 2017), which can lead to an enhanced ^{39}Ar isotopic abundance in adjacent aquifers (Andrews et al. 1989; Loosli et al. 1989; Yokochi et al. 2013). For this reaction to be dominant, a sufficient neutron flux and ideally a high target density of ^{39}K is necessary. High neutron fluxes resulting in strong ^{39}Ar underground production can be provided by several sources. Uranium and thorium provide neutrons as a side product in their respective decay chains (Šrámek et al. 2017) and Nyiragongo's lava was found to be especially enriched in both U and Th (Williams and Gill 1992). Natural nuclear reactors like those described in Oklo, Gabon (Gauthier-Lafaye et al. 1989) can also provide very high neutron fluxes. Furthermore, Yokochi et al. have studied the natural production of $^{39}Ar^*$ in rocks due to background radiation caused by U, Th and ^{40}K. Since young rock carries a higher concentration of those isotopes, as they are not decayed yet, the $^{39}Ar^*$ concentration inside the rock matrix can be several orders of magnitude higher than geologically old rock (Yokochi et al. 2012) Figure 34. With temperatures above the rock's release temperature, this highly concentrated geogenic $^{39}Ar^*$ could easily be released by the rock matrix into the groundwater system.
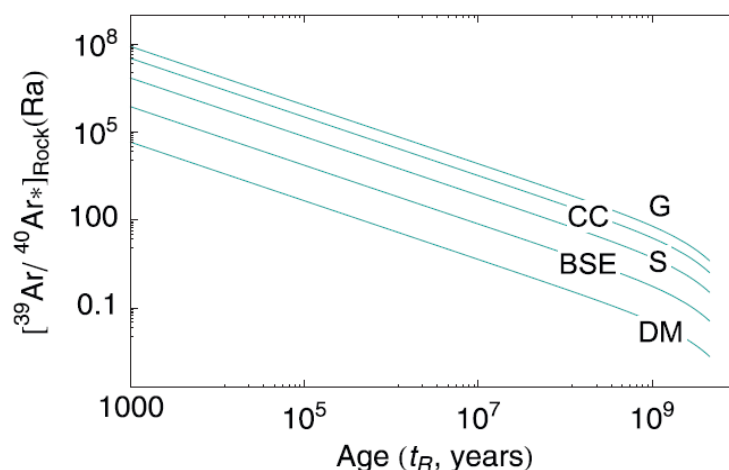

Figure 34: The $^{39}Ar^*/^{40}Ar^*$ ratios in closed-system silicate rocks, from (Yokochi et al. 2012). G granite, CC continental crust, S sandstone, BSE bulk silicate Earth, DM depleted mantle.

All three described scenarios or a combination of them seem to be possible regarding the young dynamic geology around Lake Kivu, as evidenced by e.g. the lake level rise 10 – 14 kyr BP due to the activity of the volcanoes Nyiragongo and Nyamulagira (Ross et al. 2014). ^{39}K as a target for neutrons should be available, as it is the main isotope of potassium and abundant in many bedrocks. Notably, the lava of Nyiragongo is described to be "ultra-alkaline" and therefore, especially rich in potassium (Chakrabarti et al. 2009; Sahama 1972; Williams and Gill 1992). Thus, a high concentration can be assumed, especially in any young vulcanites.

The distinct vertical localization of the groundwater inflows indicates hydrogeological structures comprising distinct confined aquifers. The inflow at 253 m, for example, has been precisely localized by Ross et al. (Ross et al. 2015) close to the city of Goma (DRC). Volcanic rock can form very complex hydrogeological networks composed of alternating layers of compact soil (e.g. volcanic ashes) and layers with high permeability such as tuff, pumice or even hollow lava tubes (MacDonald et al. 2005), which might be an explanation for the distinct aquifer structures. It was also previously observed that the eruptive events of the Nyiragongo volcano can be linked to changes in the aquifer fracture system near Goma (Tedesco et al. 2007).

The analysis of our measurements using the pre-parameterized Simstrat model (Bärenbold 2020a) appears to successfully represent *in situ* conditions with two caveats: The deviation of the ^{39}Ar measurements at 280 m and the discrepancy of the model to the measured value at 220 m. The measurements at 280 m are not conclusive. We suspect a contamination error during sampling or sample preparation. To prevent such a mistake in the future, a triplicate sampling at every depth is advisable. Although this error is significant for the concentration analysis, it does not change our interpretation qualitatively. For a quantitative analysis of factors like residence time in the ^{39}Ar-producing zone or reactivity of the same, further isotope measurements and a geological analysis of the area would be necessary.

One depth range where the model does not represent *in situ* conditions, is the ^{39}Ar concentrations in the layer between 200 and 250 m. Here, our model gives us ^{39}Ar concentrations of about 1 R_A, while our measurements are clearly lower at $0.68^{+0.09}_{-0.08}$ R_A. As a result, the ^{39}Ar abundance of the inflows at 190 and 253 m had to be reduced to zero in the simulations. Otherwise, the assumption of an atmospheric ^{39}Ar concentration of the groundwater at recharge and no underground production would have resulted in an age of the inflowing groundwater greater than 1000 years (about four ^{39}Ar half-lives, detection limit) and (together with the flux volume of about 17 m³/s) in a reservoir volume of at least 5e11 m³ between precipitation and infiltration. This would be unrealistically high. Especially because all of the groundwater intrusions seem to carry tritium (Bärenbold 2020a). We assume this discrepancy to be caused by the aforementioned error in our simulations. The presented simulations overestimate the total amount of argon entering the lake at 310 m and below, which is strongly influencing the ^{39}Ar isotopic abundance at 225 m. A lower amount of total argon entering at 310 and 330 m would increase the influence of downwards mixing from the 253 m spring. Therefore, our inferred ^{39}Ar concentrations seem to be underestimated to a certain extent, although quite high.

Our sampling and sample preparation methods were proven to be successful, despite one problem with the 280 m sample. Especially in comparison with the first attempt in 2018, we were able to successfully sample gas with a total argon concentration down to about 0.01 %$_{vol}$ in 2019. The concentration measurements using ArTTA were successful as well, leading to sufficiently small errors in the ^{39}Ar concentration measurements of 29 samples down to 10 % relative uncertainty.

To further explore the origin of fluids highly enriched in ^{39}Ar in the Lake Kivu basin, additional geological and hydrogeological investigations are advisable. Hydrogeological measurements from wells and drill cores around the lake and particularly on the northern shore of the lake which is strongly influenced by volcanism, could provide insights on the aquifers feeding the lake and their recharge areas, as well as host rock composition. Since some of the groundwater intrusions could be localized before, e.g. at 253 m depth near the city of Goma (Ross et al. 2015), directed drilling around Goma could be a promising approach. Further localization surveys for discharge springs in the lake could also be promising. These could either be conducted using narrow grid CTD probing or modern unmanned ROUVs (remotely operated underwater vehicle). ROUVs would be especially useful in the search for rifts, vents or other types of subsurface intrusions for groundwater or gas.

Yokochi et al. (Yokochi et al. 2013; Yokochi et al. 2012) and Šrámek et al. (Šrámek et al. 2017) contributed to the use of geogenic noble gas isotopes like ^{4}He,^{21}Ne, ^{39}Ar, ^{40}Ar, ^{81}Kr and ^{85}Kr (in the following e.g. ^{40}Ar*, with asterisk indicating geogenic production) as age tracers to determine residence times of groundwater in bedrock that produces these isotopes. The main principle of these methods is to quantify the production processes in the rocks and the release coefficients from the rock matrix into the water phase. With those parameters, one can then calculate the relevant transit times based on the concentrations of the respective isotopes. In order for this approach to be applicable to the hydrogeology of Lake Kivu's groundwater intrusions, several more parameters would be required. The most relevant parameters e.g. for the method described by Yokochi et al. would be the ratio of ^{39}Ar* to ^{40}Ar* both in the fluid and the rock matrix. Additionally, more knowledge on the transfer of those isotopes from within the rock matrix into the water is crucial. This transfer function is highly temperature dependent as can be seen in looking at closure temperatures of rock relevant in geochronology. Those closure temperatures describe the temperature, argon diffuses out of its rock matrix and ranges for different minerals between 160°C for feldspar and 550°C for hornblende (Doepke 2017). With geothermal influences around Lake Kivu, this dependency might be highly relevant.. The work of Bärenbold et al. (Bärenbold et al. 2020c) in combination with Simstrat could provide information on the ^{40}Ar* fraction in the groundwater intrusions. Determining [^{39}Ar*/^{40}Ar*] in the rock matrix and the composition and the properties of the rock matrix, e.g. gathered from drilling cores, could be another possibility to get further insights into the geology around Lake Kivu. For this purpose, the corrected simulations to be performed in the near future will not only determine the isotopic abundance of ^{39}Ar in the groundwater intrusions, but also those of ^{36}Ar and ^{40}Ar. In doing so, we hope to infer the amount of geogenic ^{40}Ar* in said intrusions and thus, get more insights on the geochemical processes causing the high ^{39}Ar* abundance.

It was attempted to determine a TTD for argon in Lake Kivu. Due to limits of the Simstrat model in its current state, it was only possible to achieve a TTD in units of ^{39}Ar apparent age between 120 and 484 m depths. In order to extend this method towards other solutes and towards a TTD in units of real age, several adjustments deeper in the model's programming will be necessary. For now, we can see this TTD as an estimation on the time scales of thethe dynamics of Lake Kivu.

Within their described limitations, our measurements and extensive modellingresult in two major findings. First, the stratification and the very distinct properties of the water column of Lake Kivu provide strong evidence that some of the groundwater intrusions feeding the lake are highly enriched in ^{39}Ar. The hydrogeology of the Kivu region appears to comprise several very distinct aquifers with some of them likely very influenced by volcanism and radiogenic processes, leading to the highest ^{39}Ar concentrations ever described in groundwater. Furthermore, the method of ArTTA was effectively demonstrated for the analysis of meromictic lakes and an improved sampling method for very gas-rich water bodies was successfully applied.

5. Lake Kivu's gas content explored with a total dissolved gas probe

5.1. Dissolved CO_2 and CH_4 in Lake Kivu

Lake Kivu contains large amounts of dissolved gasses and thus, not only bears a possibly fatal danger to all surrounding residents but also carries a treasure that the first ones have started to exploit. The dissolved methane in Lake Kivu is abundant enough to support power plants with capacities of hundreds of MW for a few decades (Contour Global 2021; Symbion 2021; Gill 2019). After a proof of concept project at Cap Rubona in 2009 (Descy et al. 2012), the first commercial power plant KivuWatt started operation in 2016 and is currently running at a maximum capacity of 26 MW (Contour Global 2021). Future plants, planned by e.g. Symbion, are aiming for up to 512 MW (Gill 2019).

Lake Kivu's methane is a shared resource between Rwanda and the Democratic Republic of the Congo. Both states have come to a mutual agreement for a cooperative and fair use of the precious resource. As a consequence, reliable and possibly easy to apply methods for measuring the gas content are urgently needed to ensure smart and efficient use of this valuable resource. On the other hand, the vast amount of gas in the lake is conceived as a hazard by residents (2 million people in Goma alone). Although the gas content in the lake has not changed significantly since the 1950s (Boehrer et al. 2019; Bärenbold et al. 2020b), the geologic environment is very dynamic, as reflected by the strong volcanic activities in the surrounding area. Thus, changes in the hydrogeological structure, likely influencing the lake and the gas content, are very possible (Tedesco et al. 2007). Therefore, it is of the highest interest for the safety of millions of people to assess the danger of a limnic eruption, particularly after notable volcanic activity (Halbwachs et al. 2002; Lorke et al. 2004).

Different methods are available to measure dissolved gasses in water bodies, and two of them, applied to Lake Kivu, will be presented briefly in the following.

Figure 35: Gas extraction raft of proof-of-principle power plant KP1 in 2018. In the back ground one see from left to right the peaks of the volcanoes Nyiragongo, Mikeno and Karisimbi. Nyiragongo is active and has a constantly open lava lake in its crater.

One of the most common methods to determine gas amounts and compositions is the collection of water samples, which are analyzed with a gas chromatograph for their dissolved substances (Boehrer et al. 2019). For this method, the gas is extracted from the sample and guided through e.g. a zeolite-filled column together with a carrier gas (mostly helium). The zeolite has a large surface area and constantly weakly adsorbs and desorbs the different gas molecules, mainly via van-der-Waals forces, donator-acceptor-bonds and H-bonds This adsorption-desorption dynamic is dissimilar between different gas-zeolite combinations, so the propagation speed through the column is specific for each gas. A detector at the end of the separation column measures the gaseous mixture components quantitatively and differentially. Using a gas chromatograph to measure Lake Kivu's gas content entails several challenges, mainly regarding the sampling. In order to determine the gas concentrations, one has to know the exact amount of water the gas was extracted from. This is the main challenge for Lake Kivu, since its deep water is oversaturated in gas compared to atmospheric pressure. So, when sampled with e.g. a Niskin bottle, a compensation volume has to be added to the sampler to account for the expanding gas. This can be achieved by adding, for example, an inflatable balloon to the Niskin bottle. Sampling bags can be used for a reliable quantification of extreme quantities of dissolved gasses (Horn et al. 2017; Boehrer et al. 2019).

Another method is the analysis of the extracted gasses using a mass spectrometer (Bärenbold et al. 2020b; Bärenbold 2020a). A mass spectrometer ionizes the gas mixture and achieves the discrimination of the gas-mixture components via their different charge to mass ratios e/m. Mass spectrometers are mostly large stationary

machines. However, smaller spectrometers for in-field applications were developed, which, in combination with e.g. a membrane contactor, can measure the gasses dissolved in water directly on site (Brennwald et al. 2016). Such a mass spectrometer is powerful but its use and maintenance can be challenging.

Since the currently used monitoring strategies, although very useful, are challenging and require well trained and educated operators, a quick, easy and reliable method to achieve the same goal(i.e. determining the gas amount and composition in Lake Kivu) would be very welcome. Measuring total gas pressure with a sensor (total dissolved gas = TDG sensor) appears as a simple and viable way to record and detect even small and slow changes in the gas content (see Figure 36).
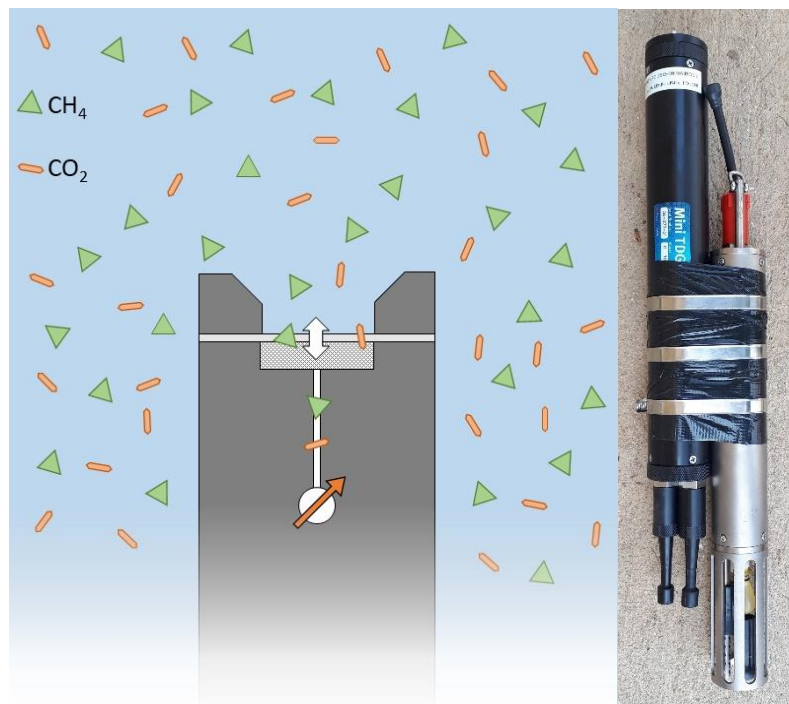
Figure 36: Left: Sketch of the sensor head of the ProOceanus Mini TDGP. The green triangles and the orange bars represent methane and carbon-dioxide respectively. Both dissolved gasses pass through the PTFE membrane into the inner volume comprised of a metal mesh, a thin channel and the pressure sensor. Right: The TDG probe mounted to a Sea&Sun 48M CTD probe.

Such a probe consists of a pressure sensor in a measurement volume separated by a semi-permeable membrane from the lake water. This membrane is permeable for gasses, but not water and non-volatile solutes. Under water, an equilibrium between the sensor volume (i.e. the gas side) and the water side is reached with the pressure in the measurement volume representing the total dissolved gas pressure of the gasses in the water (see Figure 37 a)). Under certain assumptions, conclusions can be drawn about the dissolved amounts of gasses. In the following we explored the possible use of total gas pressure measurements to draw conclusions about dissolved gasses.

5.2. Extending the capabilities of a TDG probe

A TDG measurement, as presented in Figure 37 a), records the pressure and resembles a limited growth, reaching a plateau. This type of data was normally obtained by either reading the pressure after reaching the plateau or by fitting the curve with a limited exponential growth law:

$$P(t) = P_0 \cdot \left[1 - exp\left(-\frac{t}{\tau} \right) \right]$$

Equation 40

With τ being the response time depending on the permeability of the membrane.

The gas transport through a semi-permeable membrane such as PTFE can be described by the Solution-Diffusion model (Barrer and Rideal 1939; Wijmans and Baker 1995):

$$J = \frac{k}{h} \cdot \Delta P$$

Equation 41

With J the flux, k the permeability, h the thickness of the membrane and ΔP the pressure gradient. With the continuity equation, we get the mass balance:

$$dN(t) = V dP_i(t) = J \cdot A \cdot dt$$

Equation 42

With P_i the pressure inside the volume and A the membranes surface area. With P_0 the outside pressure and with combining Equation 41 and Equation 42, we get:

$$V dP_i(t) = k \cdot A \cdot \frac{P_0 - P_i(t)}{h} dt$$

$$\updownarrow$$

Equation 43

$$P_i(t) = P_0 \cdot \left[1 - exp\left(-\frac{k \cdot A}{V \cdot h} \cdot t \right) \right]$$

With k, A, V and h material and setup properties, it reduces with $(V \cdot h)/(k \cdot A) = \tau$ to Equation 40.

When analyzing TDG data of Lake Kivu recorded in 2018, we noticed a deviation of the data curve and the fit curve. This deviation might be explained, by different gas species having different motilities into and inside the membrane matrix, depending on molecular interactions between the gas molecules and the PTFE membrane molecular matrix. With CH_4 and CO_2 being the two main gasses present, we thus expect a behavior of the curve following a two component limited exponential growth:

$$P(t) = P_1 \cdot \left[1 - exp\left(-\frac{t - t_0}{\tau_1} \right) \right] + P_2 \cdot \left[1 - exp\left(-\frac{t - t_0}{\tau_2} \right) \right]$$

Equation 44

With τ_1 and τ_2 the gas specific response time through the membrane, P_1 and P_2 the respective partial pressures, t_0 a time offset and assuming the dynamics of the two

components to be independent from each other. By fitting this function, it should be possible to not only extract the total pressure, but to also infer the partial pressures and the time constants of the different gas species.
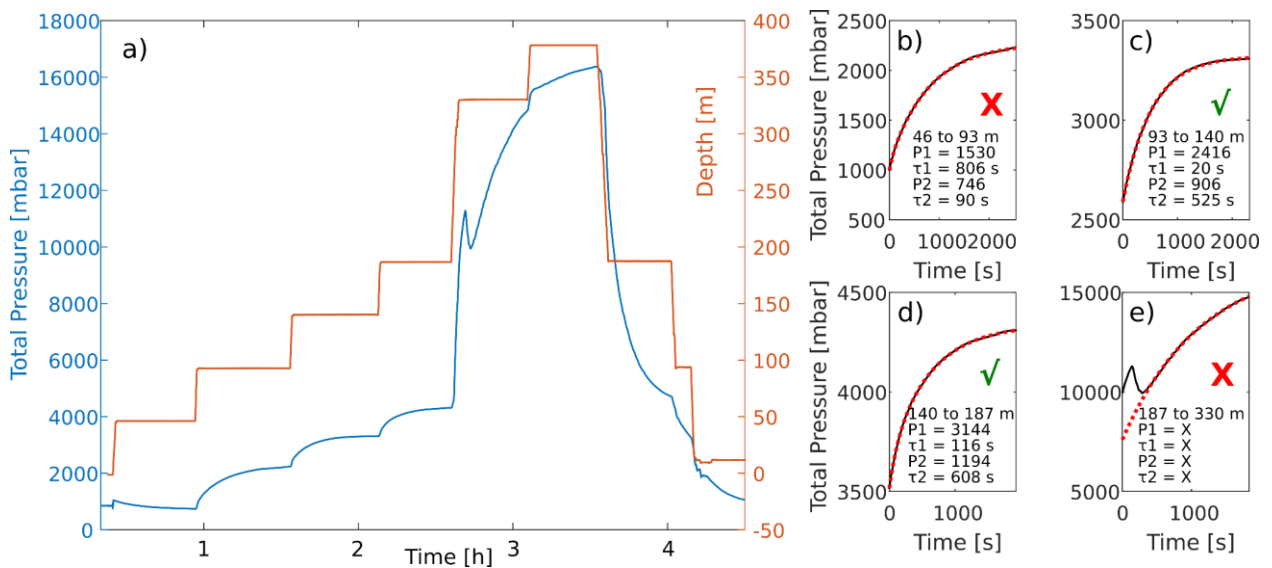

Figure 37: a) TDG probe pressure readings in blue and CTD depth reading in red. In total, five of these measurements with slightly different depth-steps were performed. Clear irregularities are visible at pressure readings > 10 bar. b) – e) Fit results for different depth-steps. b) Good fit, but does not fulfill the criterion P1 > P2 and τ1 < τ2 c) & d) Good fit and do fulfill the criterion P1 > P2 and τ1 < τ2 e) bad fit due to pressure reading irregularities

Figure 37 a) shows an example of one TDG measurement from Lake Kivu. In total, 6 profiles were measured. The red curve shows the depth data recorded with an attached CTD probe (see Figure 36). The probe was lowered in steps of 50 - 150 m. This lowering was done very fast in order to achieve a quasi-instantaneous pressure change across the membrane and the probe was kept at the new position for 30 to 60 minutes in order to approach a plateau of the readings. As can be observed at depths > 200 m, there were problems with kinks and other irregularities appearing in the pressure record. This was probably due to a fabrication problem causing the probe to not be sturdy enough to withstand high pressures. Even though the probe is a prototype that was specifically made for the high pressures in Lake Kivu, it might actually not be up to the task of being reliable with those high pressures. However, we could observe that these irregularities did not cause any permanent damage to the probe, so the other measurements were presumably not affected by them. We only used increasing pressure readings for our analysis. When pulling up the probe, the pressure gradient across the membrane is reversed and the membrane can bulge out, increasing the gas side volume and rendering the readings unusable. When the probe is pulled up too fast, this bulging can actually damage or destroy the membrane if the pressure gradient becomes too high.

66
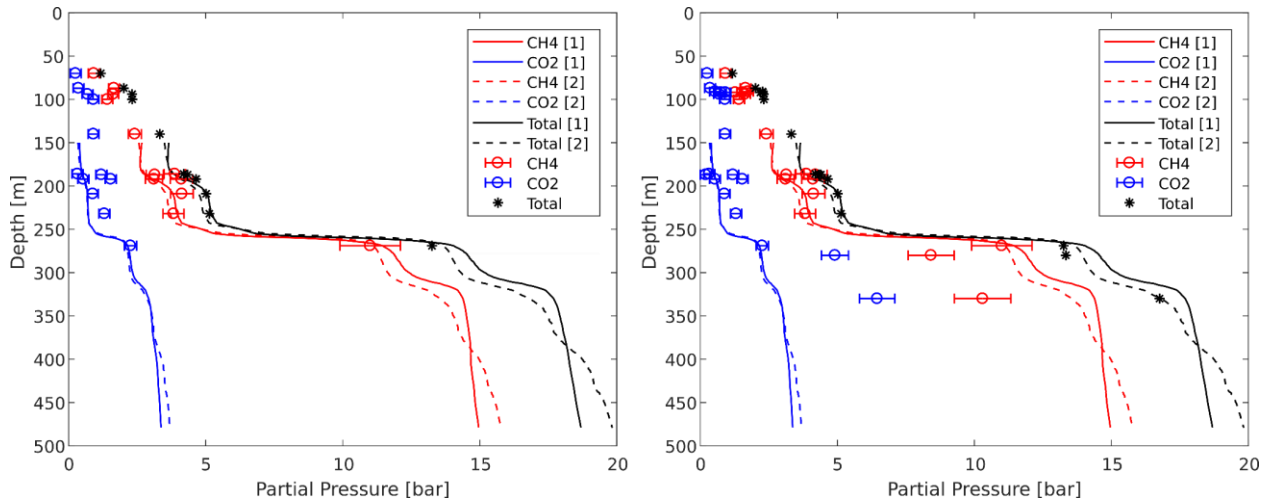
Figure 38: Red and blue lines/dashed lines: partial pressure data kindly provided by Fabian Bärenbold [1] (Bärenbold et al. 2020b) and Bertram Boehrer [2] (Boehrer et al. 2019) . Left graph: Red and blue circles: fit results fulfilling the criterion P1 > P2 and τ1 < τ2. Right graph: Red and blue circles: all fit results.

Fitting our recorded TDG data with the two component limited exponential growth model (Equation 44), we get a set of parameters $\{P_1, \tau_1, P_2, \tau_2\}$ with $P_i(z)$ plotted in Figure 38 b). Surprisingly, the time constants were not as constant as expected. We found a clear pressure dependency of the membrane permeability which led to increasing time constants with increasing pressure. We assume that this happened due to mechanic compression (Ballhorn 2000). The bigger problem, however, was that the time constants of CO_2 and CH_4 were not alike in all fits: for the majority of the fits (> 70 %) the larger partial pressure came with a smaller time constant, thus had a higher motility, and vice versa. In Lake Kivu, methane has the higher partial pressure, although, due to its much lower solubility, its overall concentration is much smaller. We thus can associate the higher partial pressure (arbitrarily chosen to be P_1) with methane and the lower (P_2) with CO_2. If we now compare the fit data with literature data (see Figure 38), we find that our fit-inferred data do fit the literature data quite well. But if we only look at the aforementioned fits which fulfill the condition $P_1 > P_2$ and $\tau_1 < \tau_2$, the correspondence of the fit inferred data with the literature becomes much better. The condition $P_1 > P_2$ and $\tau_1 < \tau_2$ (from now on called 'Lake Kivu exclusion criterion' Equation 45) could be seen as an indication, that methane (the higher partial pressure) has a higher motility through the PTFE and the measurements not fulfilling the conditions are measurements errors.

$$P_1 > P_2 \text{ and } \tau_1 < \tau_2 \qquad\qquad \text{Equation 45}$$

So it seems the idea of fitting the pressure record curve using Equation 44, we can infer the partial pressures, as well as the total pressure in the majority of the measurements. The remaining open questions are: Where does the necessary condition $P_1 > P_2$ and $\tau_1 < \tau_2$ come from and what does it say about the different motilities of CH_4 and CO_2 in the PTFE membrane? How valid is our assumption of an independent CH_4 and CO_2

passage through the membrane? Are there other factors affecting the pressure records we have not looked at so far?

5.3. Experimental falsification

5.3.1. Setup

To tackle those questions, together with the help of Emelie Breunig (Breunig 2020), an experimental setup was designed to create gas-equilibrated water and examine it with a TDG probe, effectively simulating the TDG measurements of Lake Kivu in a laboratory environment. For this purpose, a TDG sensor was built that was attached to a 1¼'' water pipe threat. The design is shown in Figure 39.
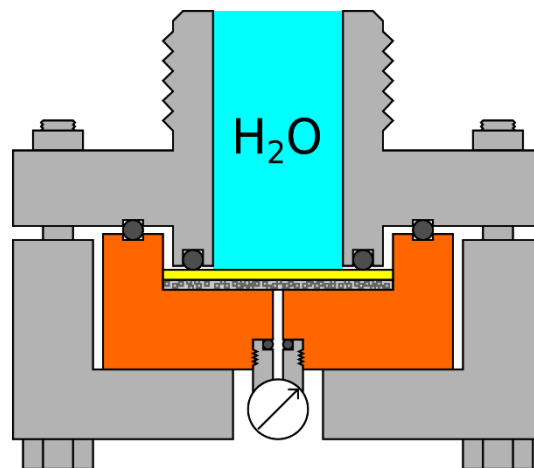
Figure 39: Sketch of the self-built TDG pressure sensor. The PTFE membrane (here yellow) and the underlying metal mesh are the same as those used in the ProOceanus MiniTDGS. The base and the membrane holder are made out of stainless steel and brass respectively. The screw-in pressure gauge is a standard commercial three connector pressure gauge with a range of -1 to +20 bar. Readout and data log is realized using an Arduino Uno.

The self-built TDG sensor consists of a membrane holder that carries the same dimensions, the same membrane and metal mesh beneath as the ProOceanus miniTDG used at Lake Kivu. The membrane holder has a 0.5 mm hole in the middle, that leads towards a commercial -1 to 20 bar pressure sensor. The gas side volume is dominated by the inner volume of the pressure sensor and was estimated at 25 mm³. This is considerably larger than the inner volume of the ProOceanus probe. We thus should expect considerably longer equilibration times. Sensor read out and data logging was realized using an Arduino Uno. The pressure sensor was then installed onto a tubular system, constructed of mainly 1¼'' water pipes. The whole setup is shown in Figure 40.
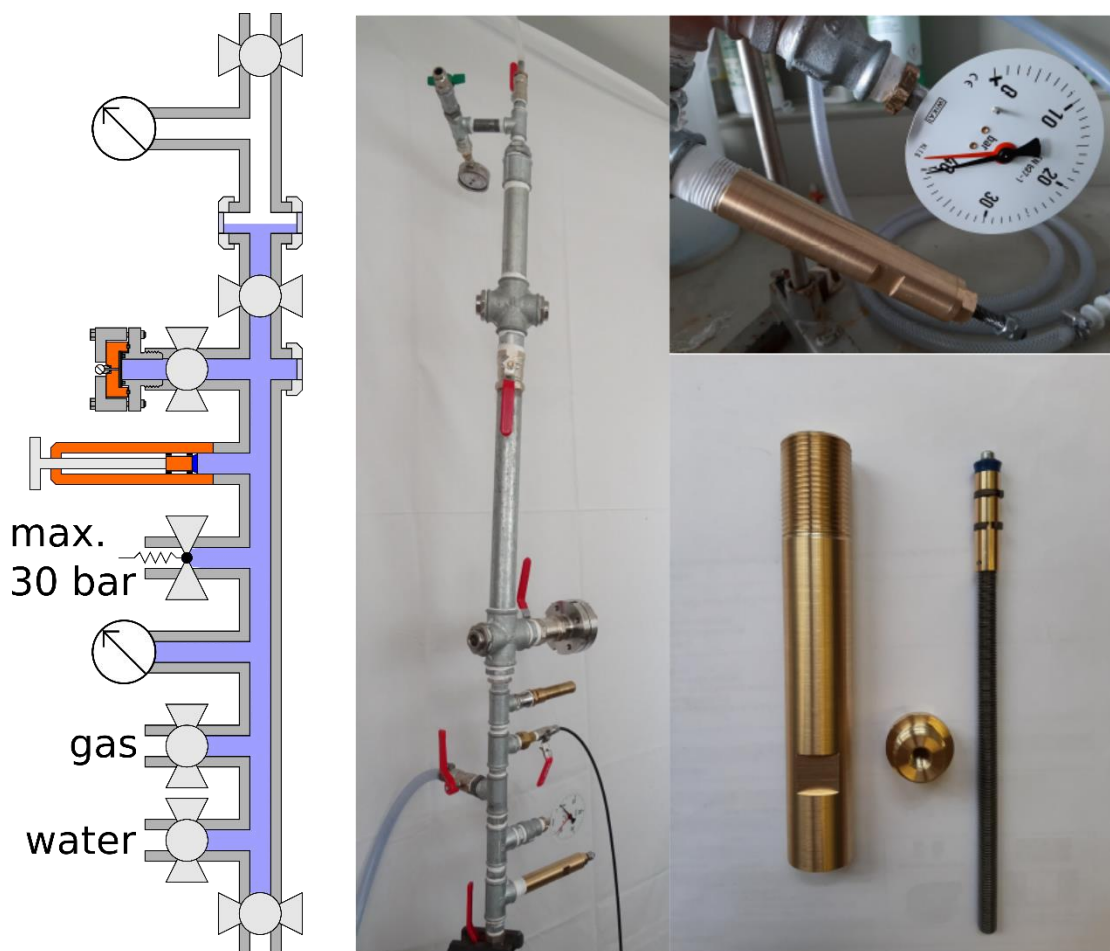
Figure 40: Full TDG experimental setup. The chamber is constructed of 1¼'' water pipe and is divided into two principle sections, which are separated with a ball valve. The lower part is the water section, where the TDG sensor and the compressor cylinder are mounted. The upper part is the headspace section. The whole setup is mounted on a rotatable axis, so that the water-gas mixture can be shaken during equilibration.

The TDG experimental setup consists of two separable parts, the lower one is the water part, which exclusively holds gas equilibrated water during the measurement. The upper part is the headspace which holds the gas reservoir during the gas-water equilibration, that happened before each measurement. Several lines are attached to the water part. The water inlet was attached to a deionized (VE-) water line. The gas line was attached to two CO_2 and CH_4 bottles, providing gas pressures of 14 and 10 bar, respectively. Then, a self-constructed high pressure cylinder was installed. This compression cylinder could increase the water pressure to at least 40 bar, but we decided to install a 30 bar security valve to avoid the risk of bursting pipes. The pressure cylinder was useful to simulate water pressures larger than the gas pressure of the dissolved gasses. The TDG sensor described above was installed to the water part in combination with a valve. Manometers were attached to both the water and the gas part to control the gas and water pressures.

The whole setup was leak-tested extensively in order to accommodate measurement run times of several hours. Pressures of 20 bar could be contained for >10 h without dropping significantly. In order to introduce turbulences, increasing equilibration

speeds tremendously, the whole setup was mounted on a mount allowing rotation of about ± 150°. The inner volumes were estimated as the following: water part 800 cm³, head space 250 cm³. The used water was the deionized water from the institute with a nearly constant temperature of 21°C.

5.3.2. Measurement Routine

The measurements that were performed can be divided into two main categories: pure gas phase (A & C) measurements and gas-equilibrated water measurements (B & C).

The first measurements determined the increase of pressures of pure gasses passing through the membrane, since these are the easiest measurements to perform and we can learn about the passing of gasses from its gas phase through the membrane in this way. Those measurements were extended later by including binary mixtures of CO_2 and CH_4 as well.

The second category represents measurements of the pressures of gas-equilibrated water. For those measurements, the chamber was filled with about 1 L of water. Then, the gas line was opened, as well as very slightly the top outlet. This created now a constant gas flow through the water flushing the headspace until it was assessed to be air free (mostly about 30 min). Then the top outlet was closed and the gas pressure was increased to the desired end pressure. Equilibration with occasional rotation of the chamber then took from 10 – 30 min for CO_2 up to 5 h (16 h in one case) for CH_4. This was necessary to account for the much lower solubility of CH_4:

$$K_{CO2} = 33.8 \ \frac{mmol}{L \cdot bar} \quad K_{CH4} = 1.34 \ \frac{mmol}{L \cdot bar}$$

$$\updownarrow$$

$$K_{CO2} = 750 \ \frac{cm^3_{STP}}{L \cdot bar} \quad K_{CH4} = 30 \ \frac{cm^3_{STP}}{L \cdot bar}$$

Equation 46

The equilibration times were determined experimentally and were doubled later, to guarantee well-equilibrated water. Not only pure gasses were measured this way, but mixtures of CO_2 and CH_4 as well. One additional possibility in those measurements was to increase the water pressure independently of the gas pressure using the compression cylinder. For example, water could be equilibrated with 5 bar CO_2. After equilibration, the water part was carefully cleared of remaining bubbles by knocking onto the steel piping with a heavy tool. Then, the dividing valve between the water part and the head space was closed. Afterwards, by screwing in the piston, the pressure could be increased from 5 bar up to e.g. 20 bar. The aim behind this was to mimic a natural setting with a total gas pressure of e.g. 5 bar at 200 m depth, and thus 20 bar water pressure.

The measurement process itself was quite similar for both gas-phase and gas-equilibrated water measurements: after the described preparation, the valve to the TDG probe was opened, and the read out pressure was recorded. The whole setup could be rotated during measurement. A stainless steel metal cage with stainless steel balls was inserted into the water part. On rotation of the whole setup, the cage moves and creates some turbulence to prevent bias of gas diffusing too slow towards the membrane. No significant difference in measurements with or without this rotation could be observed.

The four different measurement setups are visualized in Figure 41.
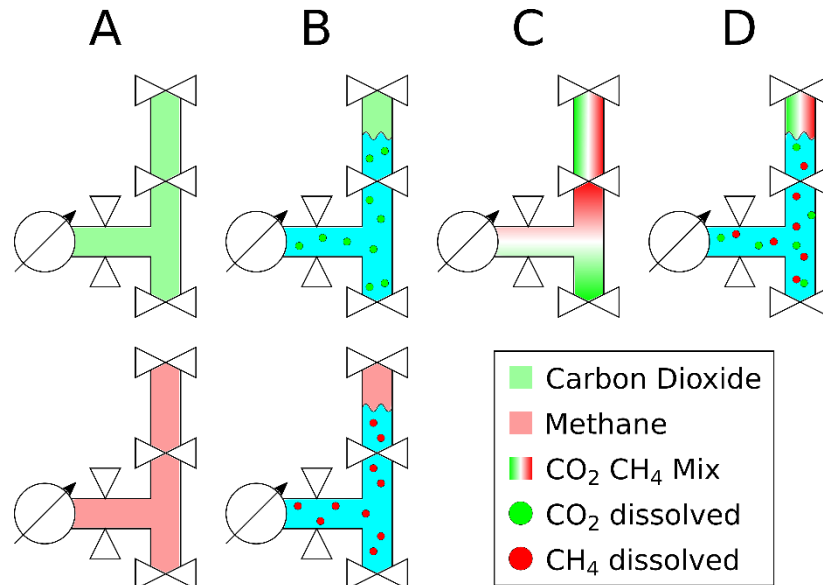
Figure 41: Visualization of the four different measurement configurations. A – Pure gasses are measured in their gas phase. B – Pure gasses are equilibrated with water. The equilibrated water is then measured. C – CO_2 and CH_4 are mixed and are measured in gas phase. D – CO_2 and CH_4 are mixed and equilibrated in water. The water then is measured.

5.4. Results

A – Pure gasses in the gas phase

Measuring pure gasses in the gas phase was done in several steps, either successively increasing the pressure after equilibration, e.g. 0-2, 2-5, 5-10 and 10-13 bar. Or directly increasing from e.g. 0-10 bar. No systematic differences were observed during both approaches.
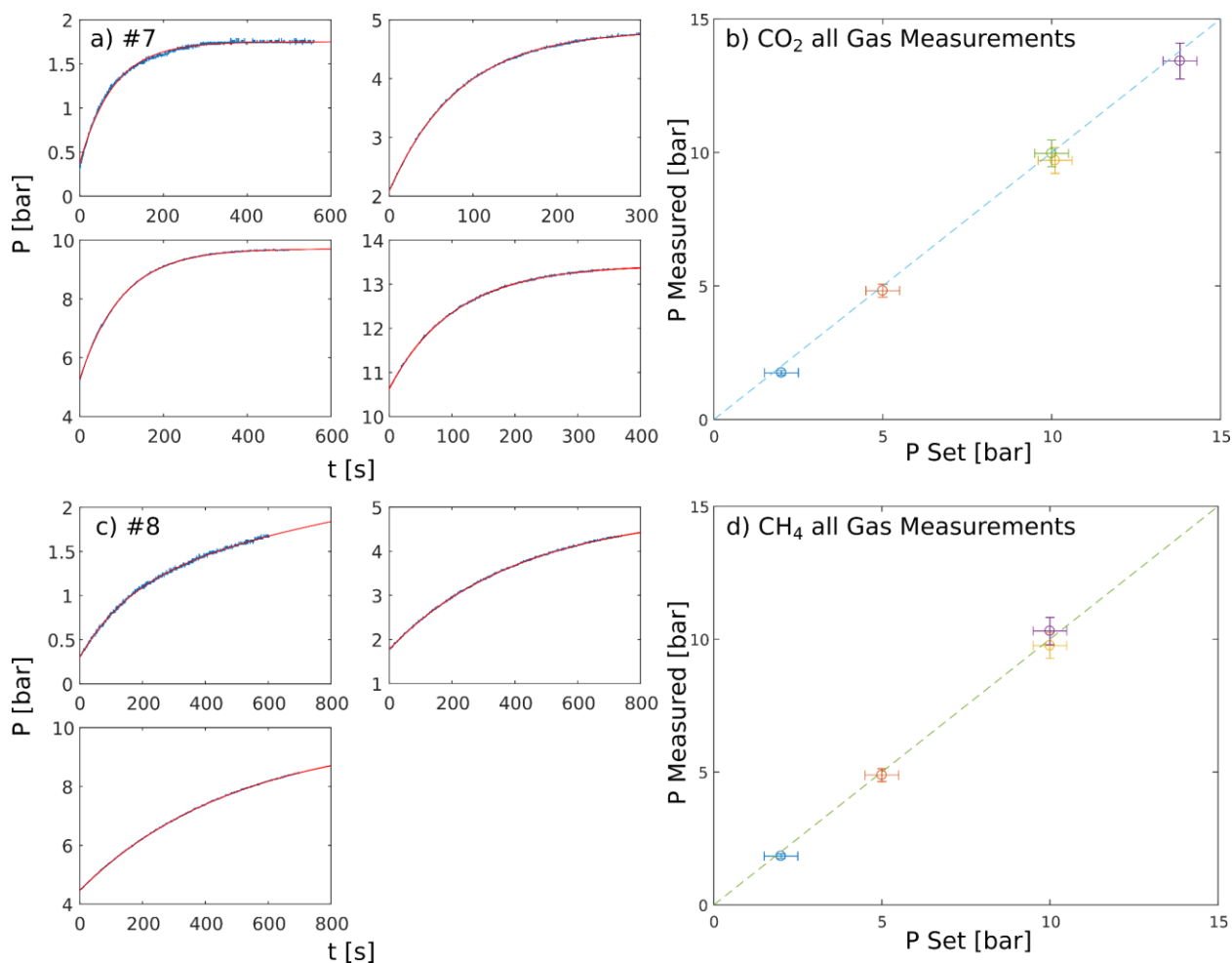
Figure 42: a) & c) Pressure readings of the TDG sensor [bar] over time [s] and b) & d) TDG measured pressure vs set pressure with pure CO_2 (a & b) and CH_4 (c & d). The graphs a) & c) are complementary to Table 7. Graphs b) and d) are representing all pure gas phase measurements.

	CH$_4$ Gas – Measurement #8			CO$_2$ Gas – Measurement #7			
Step [bar]	0 − 2	2 − 5	5 − 10	0 − 2	2 − 5	5 − 10	10 − 14
P [bar]	1.8	4.9	9.8	1.8	4.8	9.7	13.4
τ [s]	300	420	500	80	84	100	105

Table 7: Extrapolated pressures and time constants resulting from the fits of two exemplary measurements for pure gas.

All records are corresponding well to the fits with the one component limited exponential growth model (Equation 40). All end pressures were reached within the error margins. Looking at the time constants, we have much shorter timescales for CO_2 than for CH_4, which is contradicting the before mentioned exclusion criterion for Lake Kivu. We also observe an increase in the time constants with the overall pressure.

B – Pure gasses dissolved in water
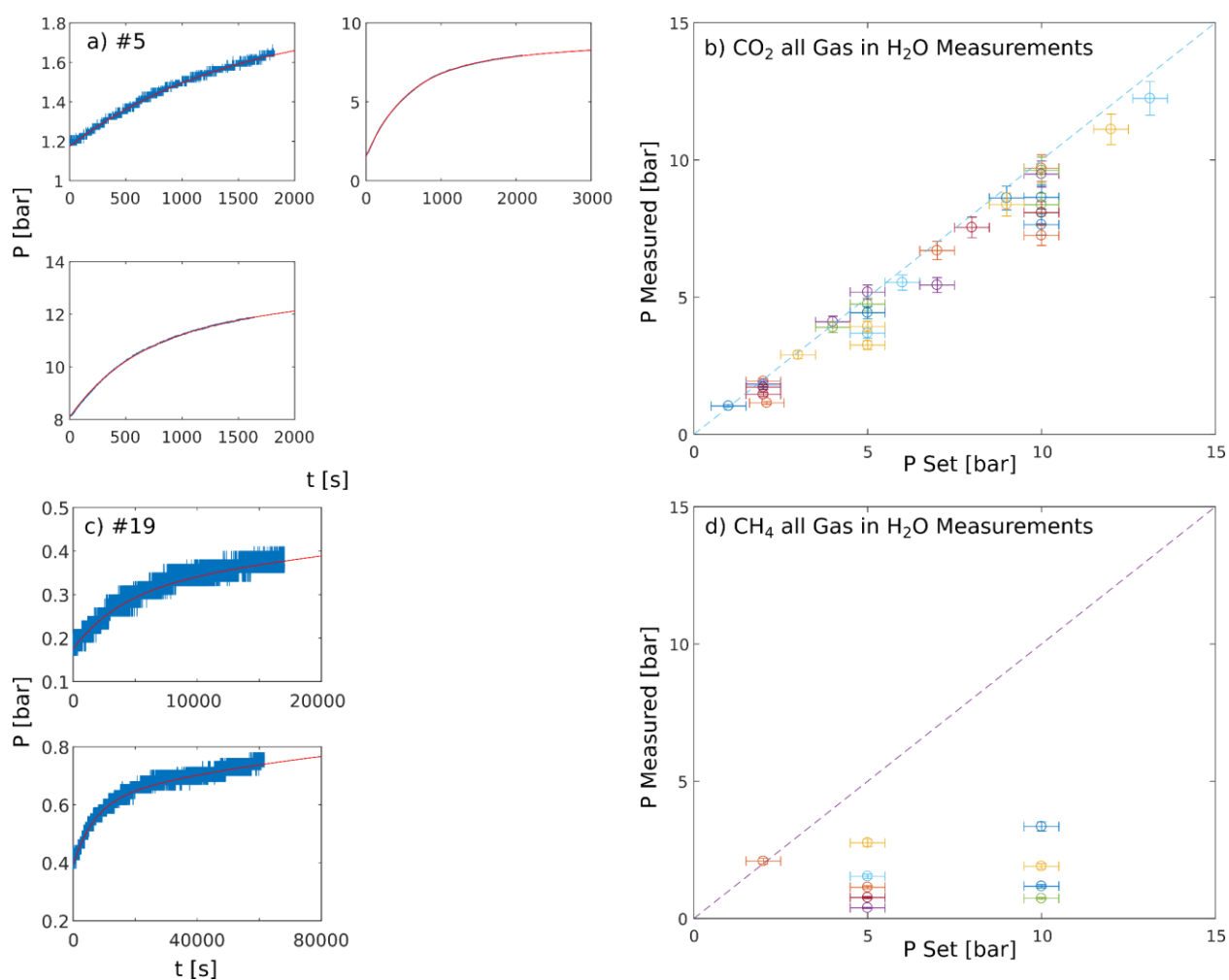
Figure 43: a) & c) Measurement data and b) & d) measured pressure vs set pressure with pure CO_2 (a & b) and CH_4 (c & d) dissolved in water. The graphs a) & c) are complementary to Table 8. Graphs b) and d) are representing all measurements of this type. One can clearly see in c) and d), that the methane is barely able to pass through the PTFE membrane.

	CH₄ in H₂O – Measurement #19		CO₂ in H₂O – Measurement #5		
Step [bar]	0 – 5	0 – 10	1 – 2	2 – 10	10 – 13
P [bar]	0.4*	0.7*	1.8	8.1	12.2
τ [s]	9500	15000	1500	620	730

Table 8: Pressures and time constants resulting from the fits of two exemplary measurements for pure gas dissolved in water. *: The methane dissolved in water was only barely able to penetrate the membrane. The end pressures were not reached after a runtime of about 16 h.

Figure 43 and Table 8 are showing some example measurements of pure gasses dissolved in water. For CO_2, the results seem to resemble those found for the gas phase measurements, with the exception of the time constants which increased by a factor of about 7. Only the time constant at #5(1 – 2 bar) is much higher. It is unclear why this was found. As can be seen in Figure 43 b), the final pressure could be determined by fitting in the majority of measurements. Some measurements, however, gave

slightly lower values, which can be explained by e.g. equilibration errors. For methane on the other hand, we observe clear deviations from the behavior seen before. It seems that the methane is only barely able to penetrate the membrane, resulting in time constants of several hours. Even with measurement times of up to 16 h (overnight) the set pressure was not reached and the fit parameters did not reflect the adjusted pressures. It could be excluded that this was an effect of non-equilibrated water, as equilibration times before each measurement did spread from 1 – 12 h, while times of about 30 minutes were tested beforehand and assessed to be sufficient. Moreover, a 90 minutes CH_4 equilibration in measurement #35 (gas mix equilibrated in water, as shown down below) was sufficient. It thus can be inferred, that the impermeability of the membrane to the methane is specific to an interaction between dissolved $CH_4(aq)$ and the PTFE.

When measuring pure gasses dissolved in water, measurements with additionally increased water pressures were also performed. It turned out that the increase in water pressure did not affect the pressure readings significantly. Measurements with additional water pressures of 10 and 15 bar were performed.

C – Mixed gasses in gas phase

Since the pressure reading dynamics of single gasses both in gas phase and dissolved in water were investigated, the focus will now be on gas mixtures. Here, the main interest will be whether and/or how the gas mixture's compositions can be inferred from the pressure reading dynamics. For this purpose, different pressures and pressure ratios of CO_2 and CH_4 were filled into the experiment and measured as before.

Figure 44 and Table 9 show an exemplary selection of all performed measurements of this type. Looking at measurement #11 and #14, setups with different partial pressures for CO_2 and CH_4 (7:3 or 3:7 bar), one can observe a clear separation of the partial pressures. However, there is also a clear contradiction to the measurements with single gas species in the time constants. The time constant of e.g. CO_2 which was always smaller than the one of CH_4 in the measurements before, was larger in measurement #11. However, it was smaller again in measurement #14.

Looking at the measurements #12 and #39 which both had equal CO_2 and CH_4 partial pressures (1:1 or 5:5 bar, respectively), equal partial pressure values from the fits were expected but were not inferred. In fact, the inferred partial pressures deviated from the expected values by >30% (see Table 9) in both measurements. It is clear, that equal partial gas pressures are not distinguishable by this method. In all gas mixture measurements, the fit-inferred partial pressure component with the stronger contribution to the total pressure also has the higher time constant, hence shows a slower dynamic (e.g. Table 9 #12 $[P_1,\tau_1]$=[1.3 bar, 320 s] and $[P_2,\tau_2]$=[0.6 bar, 55 s]). This observation contradicts the Lake Kivu exclusion criterion as shown in Equation 45.
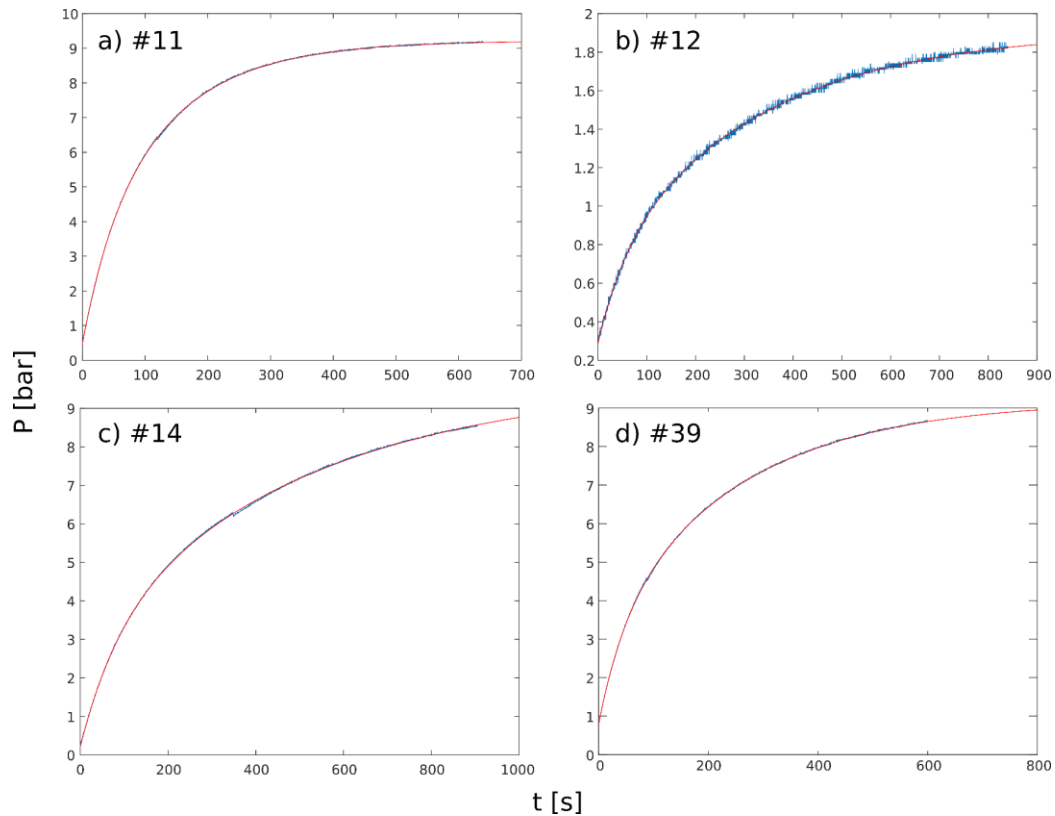
Figure 44: Pressure readings of gas mixtures in gas phase. The data shown here are complementary to Table 9, showing fit results of four exemplary measurements with different gas mixtures. With measurement #11 and #14, we can clearly differentiate the different time constants. Note: in #11 the pressure associated with CO_2 rises slower than the pressure associated with CH_4; in measurement #14 vice versa. In measurement #12 and #39, CO_2 and CH_4 had the same pressure and the fit was not able to differentiate both gasses. The mixtures CO_2:CH_4 [bar] were a) 7:3 b) 1:1 c) 3:7 d) 5:5.

	$CO_2 + CH_4$ Gas Mix – Measurement #11		$CO_2 + CH_4$ Gas Mix – Measurement #12	
P_{ex}/P_{setup} [bar]	CO_2 6.6 / 7	CH_4 2.5 / 3	??? 1.3 / 1	??? 0.6 / 1
τ [s]	130	46	320	55
	$CO_2 + CH_4$ Gas Mix – Measurement #14		$CO_2 + CH_4$ Gas Mix – Measurement #39	
P_{ex}/P_{setup} [bar]	CO_2 2.9 / 3	CH_4 6.8 / 7	??? 6.3 / 5	??? 2.8 / 5
τ [s]	86	510	240	48

Table 9: Fit result of four exemplary measurements with different gas mixtures. With measurement #11 and #14, we can clearly differentiate the different time constants. Note: in #11 the pressure associated with CO_2 rises slower than the pressure associated with CH_4; in measurement #14 vice versa. In measurement #12 and #39, CO_2 and CH_4 had same pressure and the fit was not able to differentiate both gasses.

D – Mixed gasses dissolved in water

In order to mimic the dynamics in Lake Kivu, measurements of water-equilibrated gas mixtures are the most relevant. However, those were also the most complicated ones and required long preparation times. Due to time constraints, only one such measurements could be performed without critical errors or mishaps like leaking or

electronic failure. This measurement (#35) and its fit results are shown in Figure 45 and Table 10.
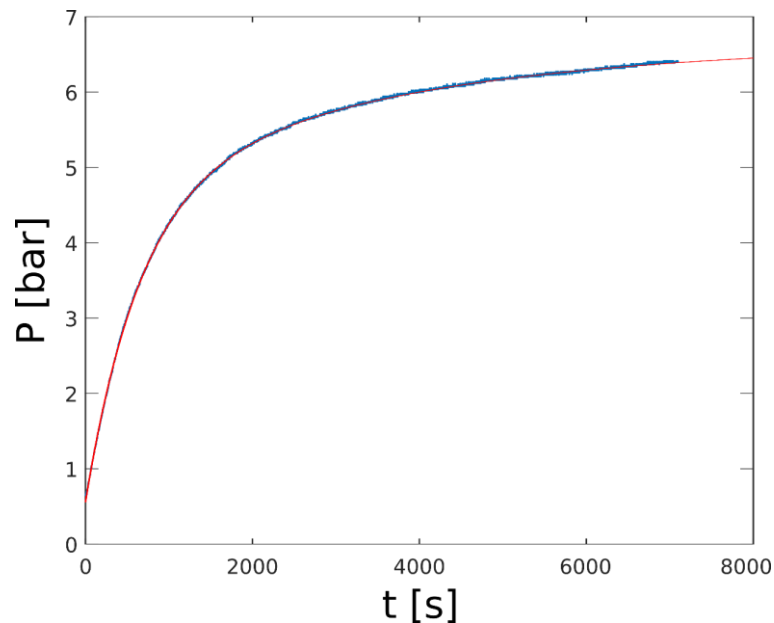

Figure 45: Measured pressure of a 5:3 bar water-equilibrated CO_2:CH_4 gas mixture. The measurement number is #35 and the corresponding data are shown in Table 10. The final pressure of 8 bar is not reached in this measurement.

	Gas mix dissolved in water – Measurement #35	
P_{Set} [bar]	5 bar CO_2 + 3 bar CH_4	
P [bar]	CO_2: 4.5	CH_4: 2.1
τ [s]	650	3400

Table 10: Fit result of measurement #35 regarding CO_2 and CH_4 content dissolved in water.

With the setup in measurement #35, the partial pressures of CO_2 and CH_4 clearly could be differentiated. While the partial pressure of CO_2 was reached within the error margin of an estimated 10%, the time constant of 650 s corresponded to the dynamics observed in the measurements with pure CO_2 dissolved in water. On the other hand, the observed CH_4 dynamics were, very surprising when compared to the measurements of type B described above. While pure CH_4 dissolved in water barely passed the membrane, here, 2.1 bar of the set 3 bar were able to pass while having a comparatively fast dynamic of 3400 s. While the lower inferred partial pressure might be an effect due to gas equilibration problems, the faster dynamics and the higher permeability of the membrane are far more difficult to explain. The observed increase of membrane permeability for CH_4 in the presence of CO_2 indicates a coupling of the dynamics of both gasses and will be discussed further below.

5.5. Summary and Discussion

By analyzing TDG measurements of Lake Kivu, we were able to infer the partial pressures of CO_2 and CH_4 via fitting in combination with an arbitrary exclusion criterion. In order to elucidate the resulting open questions, an experimental setup

was built to perform similar measurements in a controlled environment. Several different experimental setups (A – D) were used in order to investigate the processes involved in the dynamics of a TDG pressure measurement.

We found that pure gasses in gas phase (A) and, for CO_2, dissolved in water (B) followed the model of a one component limited exponential growth (see Equation 40). For all those measurements, CO_2 showed much lower time constants, hence faster dynamics, compared to CH_4. CO_2 in water showed slower dynamics (by factor 7) than gas phase CO_2. The dynamics of CH_4 dissolved in water were even slower. In fact, $CH_4(aq)$ seemed to only barely pass the PTFE membrane.
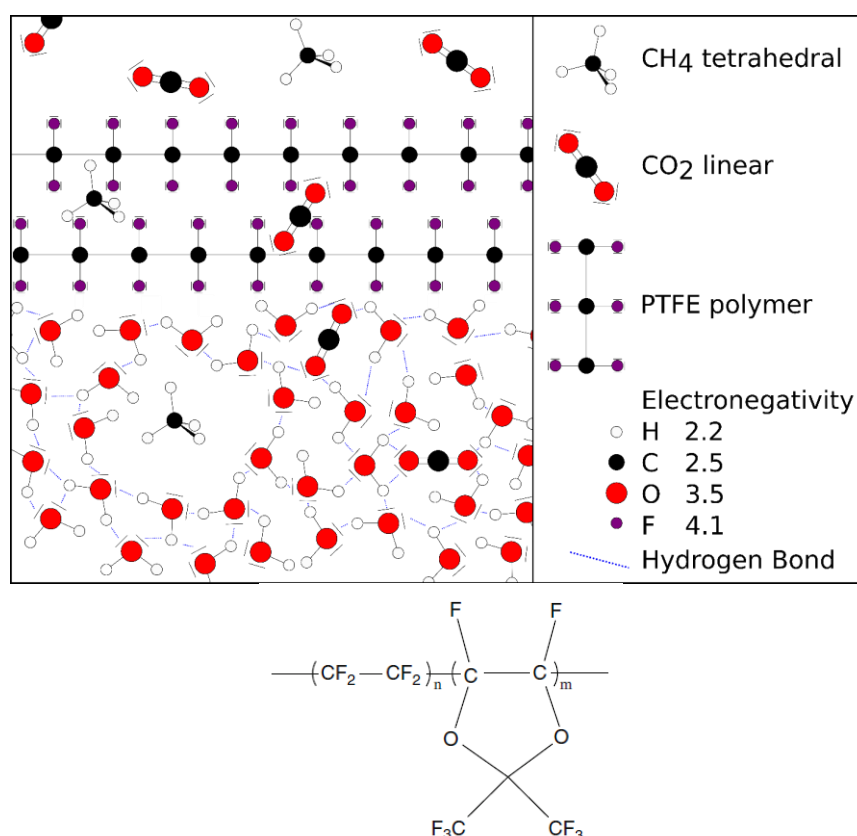

Figure 46: Left: Sketch of CH_4 and CO_2 in a H_2O hydrogen bond network close to a PTFE membrane. The small difference in electronegativity between hydrogen and carbon causes the methane molecule to be very unpolar, thus hydrophobic. The carbon-dioxide on the other hand has polar bonds and unpaired electrons and is therefore much more integrated in the hydrogen bond network of the solute water. Right: Detail of the chemical structure of AF2400 PTFE (Zhang and Weber 2012).

The difference in the CH_4 dynamics in setups A and B makes it worthwhile to consider the molecular structure of $CH_4(gas)$, $CH_4(aq)$ and PTFE. Figure 46 shows a sketch depicting some of the molecular properties of CO_2, CH_4 and PTFE.

CH_4 is the smallest alkane, a group of hydrocarbons, and its structure resembles a tetrahedron. Hydrocarbons are known for their unpolar H-C bonds and their resulting hydrophobicity. This hydrophobicity causes the very low solubility of CH_4 in H_2O ($K_{CH4} = 1.34\ mmol/(L \cdot bar)$). Water molecules are dipolar and in bulk, they build up

a network of hydrogen bonds, a weak attractive force of the partially positively charged $H^{\delta+}$-atom and the two free electron pairs of the water's oxygen. Since the CH_4 molecule is not able to integrate into the H-bond network, it occupies a relatively large volume in the water matrix and thus, has a large hydrodynamic radius. When such a hydrophobic solute is solved in water, the water molecules create a shell around the solute with a solid, nearly ice-like structure with a high surface tension, a process called hydrophobic hydration (Haselmeier et al. 1995; Conti Nibali et al. 2020).

CO_2, on the other hand, is a highly water soluble gas that displays an interesting chemistry when dissolved in water. In contrast to CH_4, CO_2 has more polar bonds and has two free electron pairs on the oxygen atoms at its ends. It threfore integrates very well in the waters H-bond network, causing a small hydrodynamic radius and a strong solubility in water $K_{CO2} = 33.8 \; mmol/(L \cdot bar)$. Furthermore, $CO_2(aq)$ reacts with water to carbonic acid H_2CO_3 (about 1% in aqueous solution), a process that is mildly dependent on temperature and pressure. This carbonic acid further dissociates, depending on the pH value, into hydrogen-carbonate- and carbonate-ions (Bauer et al. 1980):

$$CO_2 + H_2O \rightleftharpoons H_2CO_3$$
$$H_2CO_3 + H_2O \rightleftharpoons HCO_3^- + H_3O^+$$
$$HCO_3^- + H_2O \rightleftharpoons CO_3^{2-} + H_3O^+$$

Equation 47
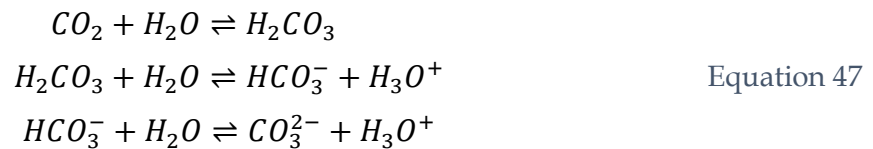
With the laboratory's deionized water determined to have a slightly acidic to neutral pH of 6.5±0.5, the equilibrium in this system favors HCO_3^-. Ions in water have a very small hydrodynamic radius, caused by the relatively strong interaction of the ionic charge with the H-bond network.

PTFE (short for polytetrafluoroethylene) is a glassy amorphous polymer constructed of chains and networks of $(F-C-F)_n$ units (see Figure 46). In bulk, PTFE is a solid of white color, that is known for its properties of e.g. being gas permeable, its low reactivity and hydrophobicity (Zhang and Weber 2012). Due to the very high electronegativity of fluorine, the fluorine groups in this polymer have polar bonds, carry negative partial charges, as well as three free electron pairs. Despite those free electrons, due to their tight bond, the fluorine atoms are not able to connect to the water's H-bond network (Dunitz and Taylor 1997). The PTFE membrane used in these experiments is made of AF2400, a PTFE variant with some additional oxygen groups which increase inhomogeneity and pore space (Golemme and Santaniello 2019).

Having reviewed some of the chemical properties and interactions of CH_4, CO_2, PTFE and H_2O, we can now reconsider the previous observations.

A – Pure gasses in gas phase

CH_4 is a non-polar, tetrahedral molecule, while CO_2 has a linear structure and polar bonds. For a diffusive process through the pores of a PTFE network, CO_2 therefore has some advantages compared to CH_4: its linear structure has, in the correct orientation,

a much smaller radius than the tetrahedral CH_4. Also, dipole-dipole interactions between the polar bounds of CO_2 and PTFE are reducing the effective radius further. The kinetic radius according to (Golemme and Santaniello 2019) is 1.65 Å for CO_2 and 1.9 Å for CH_4. It hence becomes clear, why CO_2 passes the PTFE membrane faster than CH_4, as was observed in the presented experimental results. This effect is actually widely used in gas separation procedures. The motility of CO_2 compared to CH_4 in PTFE membranes is material-dependently discussed to be around values of 13 and 20 (Gregorio et al. 2005; Scholes 2018), while in our measurements, the difference is smaller: $\tau_{CH4}/\tau_{CO2} = 4 \pm 1$, possibly specific to the used AF2400 type of PTFE.

B – Pure gasses dissolved in water

For CO_2 dissolved in water, one can observe nearly similar behavior compared to the CO_2 gas phase measurements. The increased time constants of factors around 7 could be explained by several mechanisms. In contrast to the gaseous CO_2, CO_2(aq) needs to undergo a phase transition in order to pass through the membrane. As described, CO_2 is embedded in the H-bond network of the water and for a CO_2 molecule leaving this network, additional energy is necessary, decreasing the reaction speed. Another factor could be the availability of CO_2 molecules at the surface of the membrane. The diffusivity of CO_2 in aqueous solution is obviously much lower compared to gaseous CO_2.

For methane, we observe a massive discrepancy of the TDG dynamics for aqueous vs. gaseous CH_4. While gaseous CH_4 passes the membrane, aqueous CH_4 seems to only barely be able to pass the membrane and build up a pressure behind it. This discrepancy seems to rule out an effect exclusively dependent on CH_4 to PTFE interactions. Measurements with rotating the whole setup to create turbulences performed similar, so we can exclude a diffusion bias of missing CH_4 in the vicinity of the membrane. It seems possible that the presence of water blocks the methane from accessing the membrane, maybe caused by the water's H-bond network and the interaction of the PTFE membrane with the same. For a methane molecule to access the PTFE, this interaction needs to be broken to open up a gap for the CH_4 to pass. Basically the H-bonded sphere of water molecules that formed around the methane molecule as described above (Conti Nibali et al. 2020) needs to be broken. This process might require large amounts of energy and would thus be statistically improbable. To investigate this further, simulations of the molecular dynamics would be a good tool to tackle those questions. For now, it is safe to say, that the membrane's material is not well suited to investigate pure CH_4 pressures in water.

C – Gas mixtures in gas phase

In analyzing the results from measurement type C, one can observe several deviations from the theoretical model assumed beforehand. Measurement #11 showed a higher time constant for CO_2 than for CH_4 and vice versa for measurement #14. This strongly contradicts the assumption for τ to be a material/setup constant. Furthermore, measurements #12 and #39 did not agree with the set partial pressures (set as equal: 1:1 bar and 5:5 bar) and detected two significantly different pressures (1,3:0.6 bar and

6.3:2.8 bar). Interestingly, those fitted pressures both show the same ratio of about 2.2. It was also observed that for all C-type measurements, the higher fitted pressure component always associated with the higher time constant.

This indicates that the diffusion of the two gasses across the membrane is not the sum of two independent processes, as assumed beforehand. It rather seems, that the process is the sum of two coupled processes, with a fast low pressure- and a slower high pressure component. It is notable, that this contradicts the 'Lake Kivu exclusion criterion' $P_1 > P_2$ and $\tau_1 < \tau_2$.

D – Mixed gasses dissolved in water

With both gasses dissolved in water, one can observe both gasses passing the PTFE membrane. CO_2 actually showed the same time constant of $\tau_{CO2} = 650$ s as the pure CO_2 measurements in B, but in contrast to those, CH_4 also passed the membrane with a time constant of $\tau_{CH4} = 3400$ s. The time constants are showing an equal motility ratio of $\tau_{CH4}/ \tau_{CO2} = 5.2$ as in setup A. Interestingly, the 'Lake Kivu exclusion criterion' $P_1 > P_2$ and $\tau_1 < \tau_2$ does apply in this measurement.

It therefore becomes very clear now when comparing pure $CH_4(aq)$ with the CH_4-$CO_2(aq)$ mixture, that the diffusion of $CO_2(aq)$ and $CH_4(aq)$ through the membrane cannot be decoupled. It seems that $CO_2(aq)$ enables the diffusive transport of $CH_4(aq)$ through or rather onto the surface of the membrane. This might be due to interactions of CO_2 molecules with the methane atom's hydration shell, reducing its surface tension, as CO_2 easily connects with the H-bond network.

The presented explanations of these kinds of molecular processes are currently mostly speculative. It is unfortunate, that the data available for the last setup D are limited to only one successful measurement. To get more insight into the molecular processes involved, thorough simulations of the described molecular dynamics would be required.

The aim of this project was to answer the question whether or not a TDG probe's capabilities can be extended such, that not only the total pressure, but also the main partial pressures could be worked out based on the probe's pressure recordings. We found that, with a rather arbitrary criterion, the readings from Lake Kivu can actually provide the partial pressures of CH_4 and CO_2. It became clear, however, that the processes involved in the diffusive processes from the aqueous medium into and through the membrane are not independent for each gas species but highly coupled, resulting in significant deviations in the time constants when comparing gas mixtures with pure gasses.

Looking ahead, at least two further steps are necessary in order to determine whether this TDG extension is a reliable and useful method: Performing more measurements of type D with more variations in the gas composition and creating a large data set of recordings with the original TDG probe in Lake Kivu or similar systems to test repeatability, reliability and precision.

In conclusion, determining partial pressures with the investigated TDG probe worked within certain constraints at Lake Kivu and should be investigated further. This method has the potential to be a very powerful and user friendly approach to a complicated but highly relevant problem.

6. ^{39}Ar as a versatile dating tracer - Leupa ice cave, MSM43 ocean cruise, Oman Salalah Plain groundwater

Dating with ^{39}Ar ATTA is highly versatile and applicable to many different fields in the environmental sciences. The following chapter is dedicated to the presentation and documentation of additional measurement campaigns that were mainly conducted by other group members but measured as part of this PhD project. Therefore, these project will be briefly discussed and put into their respective contexts but will not be presented as thoroughly as the rest of this thesis.

A summary of all measurements is given in Figure 47, showing the count rates of all measured samples, references and background correction measurements.
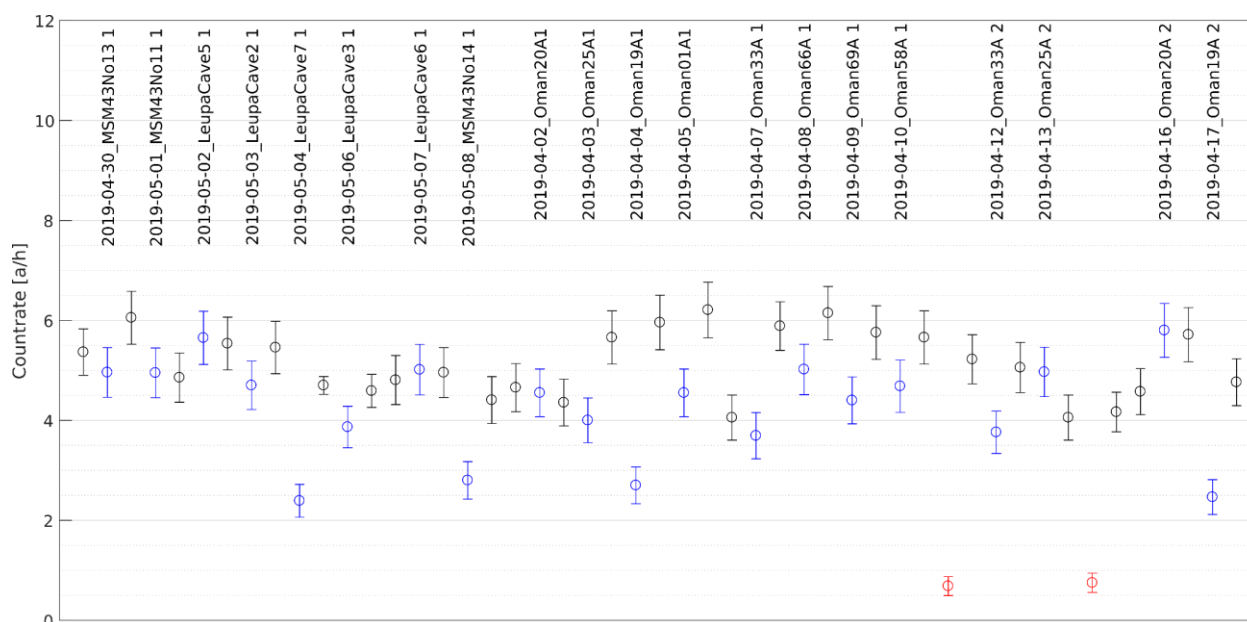

Figure 47: Summary of all count rates of the campaigns 'Leupa Ice Cave', 'MSM43 Ocean' and 'Oman Groundwater' (all in blue). The red data points are measurements with ^{39}Ar free argon for background correction purposes. The black points are all the respective reference measurements.

6.1. Leupa ice cave

Ice deposits like glaciers can play a crucial role when reconstructing the climate of the Holocene (Balco 2020; Mackintosh et al. 2017). In the ice, several atmospheric tracers can be saved and conserved until they are sampled and thus, provide valuable information on e.g. the climate conditions during ice generation. In order to combine that information with a time stamp, dating methods are a crucial part of these investigations. In a stable environment with annual precipitation and only minor thawing, glacier ice can build a layered structure similar to growth rings in trees.

Many ice bodies, however, are located in regions with an unsteady climate and variable precipitation, demanding an alternative dating approach. For these cases, ATTA provides a powerful dating tool for the isotopes [81]Kr (Buizert et al. 2014) and, as shown recently, [39]Ar (Feng et al. 2019b; Beyersdorfer 2016). With a dating range of 50 – 1000 years, [39]Ar provides a powerful tool for studying climate variations in the late Holocene like the Little Ice Age (roughly between 1570 – 1715) or the beginning of the anthropogenic climate change.

The Leupa Ice Cave is a natural ice cave in the Mt. Canin massive in the Julian Alps (Colucci et al. 2017). Located at an altitude of 2300 m a.s.l. and with an annual mean temperature of -1.4°C, an ice sheet of a mean thickness of 3 m was able to form here. Figure 48 shows a photograph of the layered structure of the ice sheet and the sampling locations of the ice samples measured in this work (numbers 2,3,5,6,7). From top to bottom, one can assume an age gradient with distinct jumps caused by thawing or precipitation free periods.

Deposits within the ice, as well as the structure of the ice, can give valuable information about the climate during ice formation. Turbid, gas bubble-containing ice is a sign for undisturbed ice, not affected by thawing. Those gas bubbles contain the argon necessary for ATTA. Clear ice is free of gas bubbles and a sign for past thawing processes after which meltwater filled the voids. Deposits investigated in this ice sheet were mainly pollen and cryogenic cave carbonates (CCC). Pollen can be used as a powerful tracer for both the climate as well as for dating purposes, as the presence of a certain species can be coupled to historic events. CCCs are carbonates precipitated from liquid water upon freezing and in this case are used to perform ^{14}C dating.
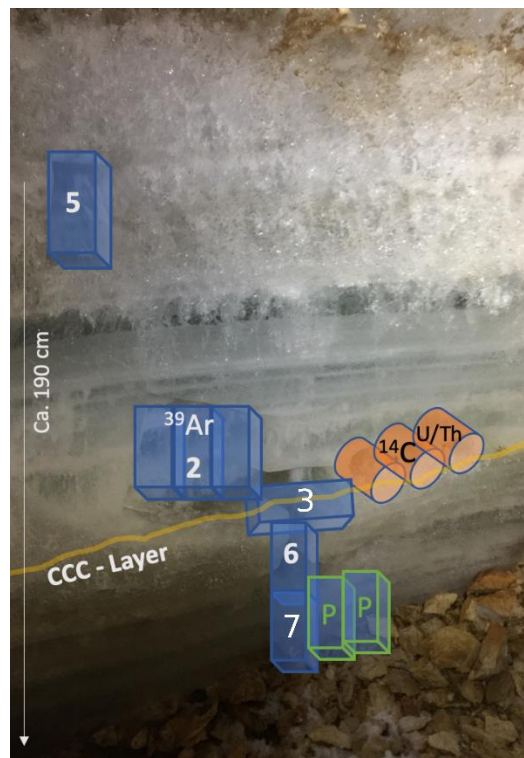

Figure 48; Photography of the sampling location of the samples analyzed with ATTA (blue; 2,3,5,6,7). The green P represents samples with analyzed pollen and the orange blocks were

analyzed by ^{14}C and U/Th dating in other laboratories. The brown line (CCC-Layer) describes a distinct layer of cryogenic cave carbonates (CCC). Modified from (Colucci et al. 2021).

Table 11 gives an overview of the results of the measured samples from the Leupa Ice Cave. Samples 2,3,5 and 6 do not vary significantly in ^{39}Ar abundance, and thus in the determined age. The measurement of sample number 7 showed significant measurement errors. Thus, only an upper age limit of about 461 years could be determined.

Sample	^{39}Ar abundance [xR$_A$]	Tracer Age [a]
LeupaCave2	0.74 +0.11 -0.11	116 +62 -54
LeupaCave3	0.58 +0.11 -0.10	211 +73 -67
LeupaCave5	0.72 +0.15 -0.14	127 +84 -73
LeupaCave6	0.84 +0.14 -0.15	68 +76 -60
LeupaCave7*	0.38 +0.62 -0.08	376 +85 -376

Table 11: Summary of the measured 39Ar samples from Leupa Ice Cave measured 2019. Samples 2,3,5 and 6 do not vary significantly. *The measurement of sample number 7 was highly problematic in terms of laser stability. Thus, it was only possible to provide a maximum age of ≲ 461 a.

The close range of measured ^{39}Ar concentrations and the absence of a distinct age gradient leads to the conclusion, that the investigated profile of the ice sheet was built up within several decades and is younger than about 117 a before 2018 (a b2018), which is based on the deepest layer with a measured age of 68 a plus its 1σ error margin. The minimum age can be inferred by sample number 5, as it is the highest in the profile. A minimum age of 54 a b2018 can be assumed.

The results of the ^{14}C and the U/Th dating were not available while writing this thesis. Only some preliminary results for the ^{14}C were available, indicating that the carbon in the CCC layer is between about 2500 -3000 years (calBP) old. This dating however, is not significantly dependent on the ice dynamics. The CCC layer originates from water intrusions into the cave, carrying large amounts of dissolved carbonates, which itself mainly come from the rock above the cave. In the simplest interpretation, the ^{14}C dates back to the formation of the carbonates in the first place. Isotopic fractionation effects can, however, bias the ^{14}C content further due to dissolution and precipitation processes (Colucci et al. 2017).

The pollen analysis of the deepest layer found small amounts of the taxon *Zea mays*, i.e. corn. Corn was introduced from the American continent to Europe after 1492, the landing of Christopher Columbus in America.

While pollen analysis can only partially confine the date of ice generation to be after about 1500 and the ^{14}C dating is strongly defined by the carbonate formation, ^{39}Ar can clearly confine the Ice sheet formation to the time period between 117 and 54 a b2018. This range coincides with the end of the Little Ice Age (LIA) and the beginning of the temperature anomaly due to anthropogenic climate warming (IPCC 2021). To further confirm the influence of anthropogenic climate change on the formation of this ice shield, investigations with other tracers might be useful. Especially investigations

with dating tracers capable of dating younger age ranges with higher precision like SF_6, CFCs and ^{85}Kr might be suitable to further elucidate the formation dynamics of the Leupa Ice Cave ice shield.
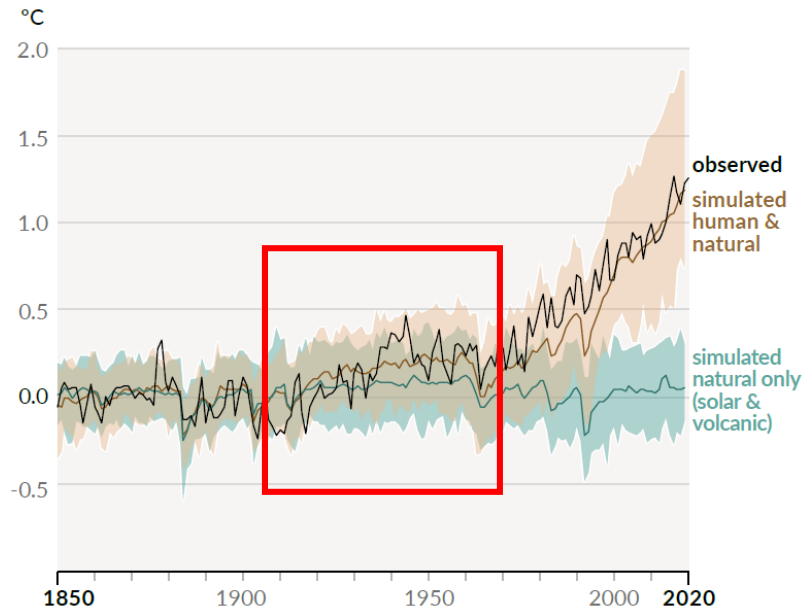

Figure 49: Annual average of the global surface temperature as observed and as simulated omitting anthropogenic contributions (IPCC 2021). Red Box: Probable time period during which the investigated ice sheet was formation in the Leupa ice cave.

6.2. MSM43 ocean cruise

The subpolar North Atlantic is an area strongly affected by climate change (Mertens 2015). Among other aims, the cruise MSM43 was dedicated to investigating the formation rate of the Labrador Sea Water (LSW), an intermediate water mass of low temperature and relatively low salinity. In the Labrador Sea, cold water sinks down and becomes part of the North Atlantic Deep Water (NADW). The LSW formation rate is an important parameter required to determine the influence of the LSW on the Meridional Overturning Circulation (MOC), a crucial component on the Earth's climate system (Feucher et al. 2019).

The aim of the ^{39}Ar measurements was to evaluate the suitability for 39Ar as a tracer for those currents and to evaluate plans of future samplings and ATTA measurements. The measured 39Ar abundances and the resulting determined tracer ages are shown in Table 12.

Sample	^{39}Ar abundance [xR$_A$]	Tracer Age [a]	Depth [m]
MSM43No11	0.75 +0.12 -0.10	112 +56 -58	4540
MSM43No13	0.69 +0.12 -0.10	144 +61 -62	3000
MSM43No14	0.54 +0.09 -0.09	243 +67 -60	1800

Table 12: Summary of the measured 39Ar samples from Maria S. Merian cruise MSM43 sampled 13.06.2015 and measured in 2019.

The measurements show very interesting and counter-intuitive results, as the [39]Ar abundance increases with depth, meaning that the tracer age decreases with depth. Assuming to be in an area with downwards convection (LSW/NADW formation), one would assume the reverse. Therefore, the convective system in this area appears to be more complex and allow younger water to flow below a layer of a higher age. However, our previous experiences with investigating ocean currents with [39]Ar (Ebser et al. 2018b) showed that multi-tracer measurements are necessary to resolve such observations.
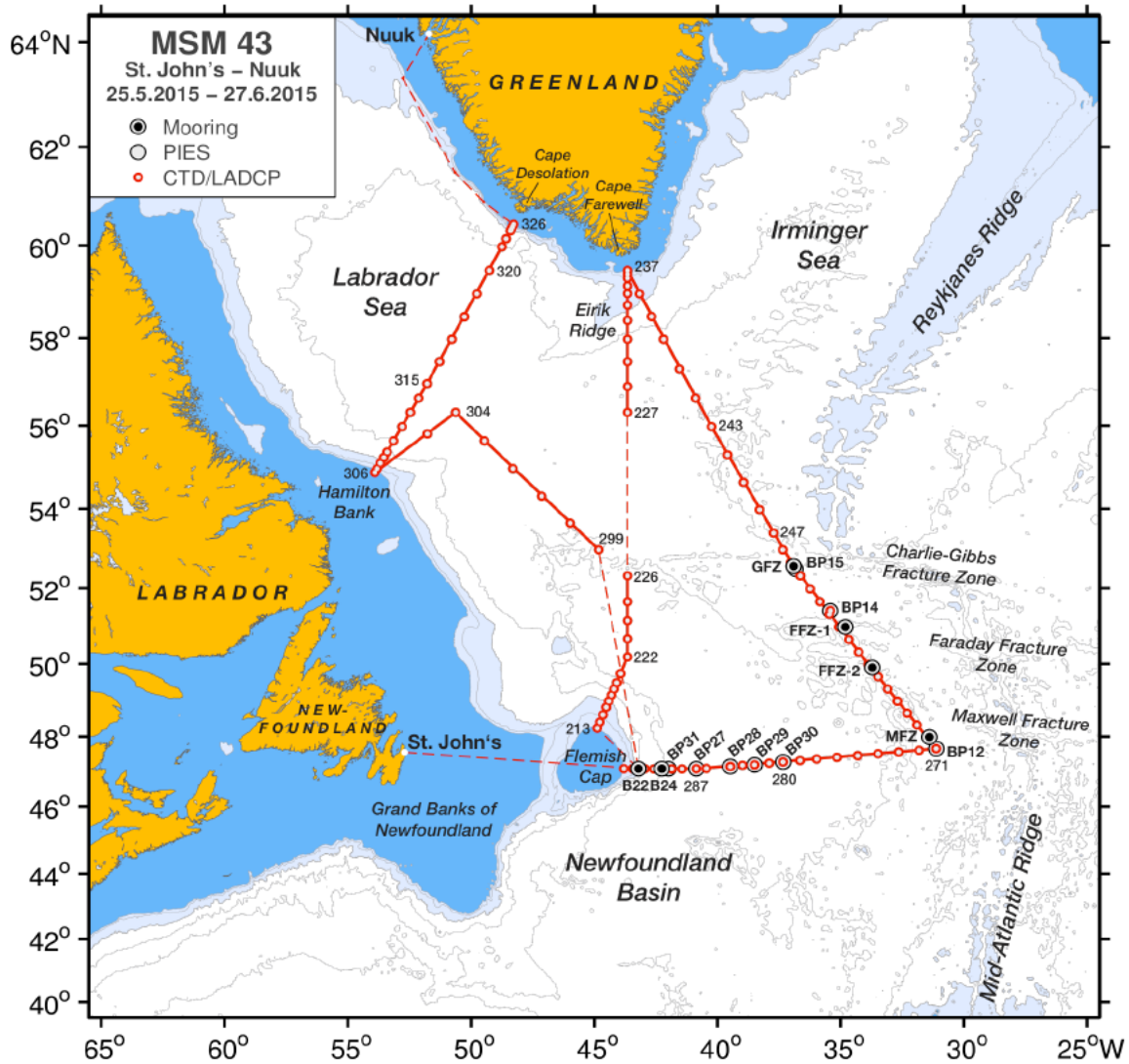

Figure 50: Route of cruise MSM43 of the research vessel Maria S. Merian from 25.05.2015 to 27.06.2015. The samples presented in this work were taken at point 280. MSM43 was part of the project 'NAC and LSW Circulation in the Subpolar North Atlantic' (MSM43 2015; Mertens 2015).

## 6.3. Salalah Plain groundwater study, Oman
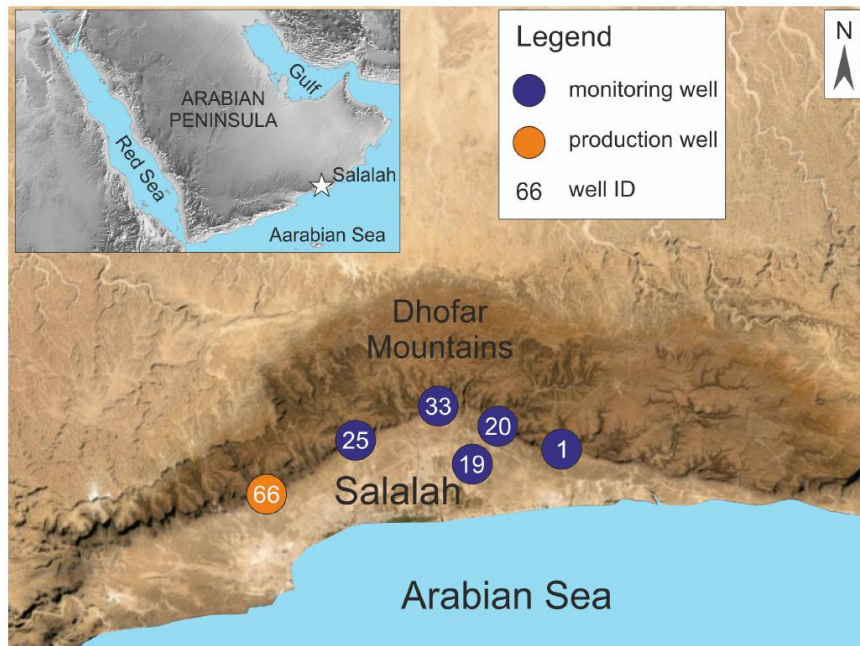
Figure 51: Map of the sampling wells in the Salalah Plain at the foot of the Dhofar Mountains (Rädle et al. 2021).

The groundwater investigations in the Salalah Plain in the southern Oman was mainly conducted by Viola Rädle and Arne Kersting. In 2018, they travelled to Oman together with our collaborators from the group of Thomas Müller from the Helmholtz-Centre for Environmental Research, Leipzig. The ATTA measurements were performed as a part of this PhD project. More detailed results and analysis can be found in (Rädle et al. 2021).

The country of Oman is dominated by hyper-arid sandy land desert. With an annual population growth of 5.4 % per year (mean 2011 - 2020) (Worldbank 2021) and a rapidly growing industrial and agricultural sector, the annual water production in Oman nearly doubled between 2011 and 2019 (NCSI Oman 2021) (see Figure 52).

The Salalah Plain is a crescent shaped enclave south of the Dhofar Mountains at the coast of the Arabian Sea. In the center of the plain lays the city of Salalah which is the second largest city of the sultanate with about 250 000 inhabitants. The main precipitation in this region happens during the Indian monsoon season in the mountain ridge and its surface runoff and groundwater recharge is the most reliable source of water for the city. Due to extensive and continuously growing groundwater abstractions for agricultural irrigation, the aquifer and thus freshwater availability is

endangered by seawater intrusions (Rädle 2019; Bucchignani et al. 2018; Al-Sarmi et al. 2017).
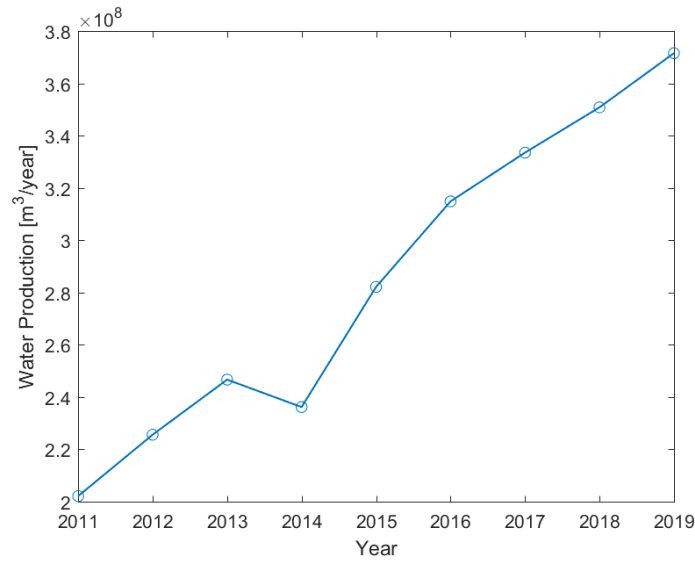

Figure 52: Annual water production in Oman between 2011 and 2019. This data originate from the governmental information portal (NCSI Oman 2021).

To better understand the Salalah Plains groundwater system, a multi-tracer approach was chosen using the following set of tracers: radiogenic ^{4}He, ^{13}C/^{14}C, ^{39}Ar, CFCs and SF6, thereby covering a broad range of ages.

Table 13 shows the results of the ^{39}Ar ATTA measurements. These measurements were performed in April 2019 with reference count rates between 4.4 atoms/h and 6.2 atoms/h (see also Figure 47). All measurements were successful, with all measured duplicates within their error margin. The precision of the measurements ranged from 20 to 10 %.

Sample	^{39}Ar abundance [xR$_A$]	Tracer Age [a]
Oman01A	0.66 +0.10 -0.09	161 +57 -52
Oman19A (1+2)	0.33 +0.07 -0.05	430 +64 -74
Oman20A (1+2)	0.94 +0.11 -0.09	20 +57 -20
Oman25A (1+2)	0.84 +0.11 -0.08	68 +39 -48
Oman33A (1+2)	0.61 +0.08 -0.07	192 +47 -48
Oman58A	0.73 +0.11 -0.11	122 +63 -54
Oman66A	0.70 +0.11 -0.10	138 +60 -56
Oman69A	0.62 +0.10 -0.09	189 +61 -58

Table 13: Summary of all groundwater samples taken from the Salalah Plain. Values shown for sample 19, 20, 25 and 33 are combined from two independent measurements.

Rädle et al. (Rädle et al. 2021) defined the shape of the TTD in two different ways and compared both approaches in the end. One approach was to use an advective dispersive model (compare Introduction 1.3 and Appendix 8.1.4) and the other one

was to use a nonparametric shape-free model, also called age histograms. The evaluation followed Bayesian statistics and a Markov Chain Monte Carlo approach, leading to a likelihood score and an uncertainty evaluation. The measured tracers involved in the TTD estimation were ^{14}C, ^{39}Ar and CFC-11. The remaining tracers showed irregularities in their results, potentially due to contamination or they were not suitable for the TTD estimation. The wells number 58 and 69 also showed strong irregularities and thus are disregarded from the analysis.

Both approaches, the advective dispersive model and the shape-free TTD led to similar results. As the TTD results of the shape-free age histogram approach fit the measurements best, they are presented in Figure 53.
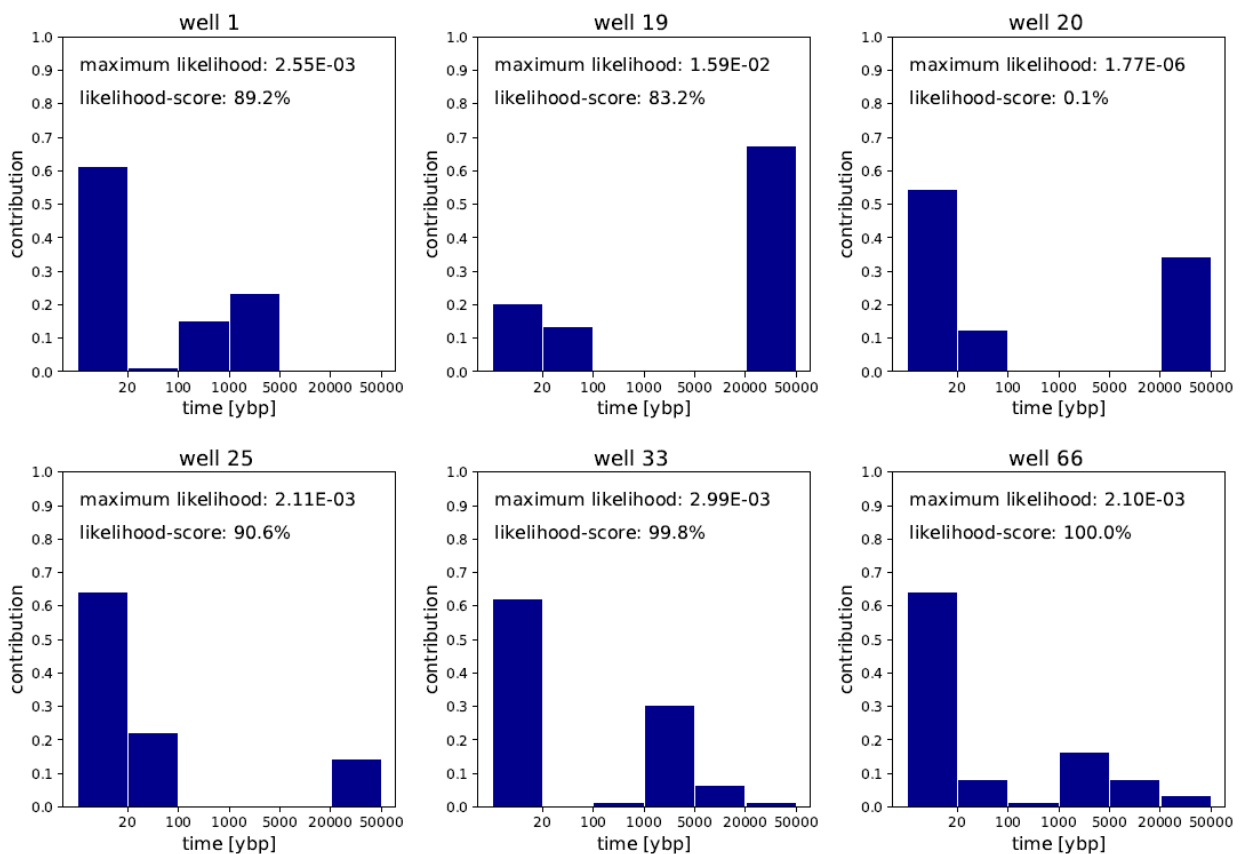

Figure 53: Resulting TTDs using the age histogram approach from (Rädle et al. 2021). The presented likelihood-score results from the division of the likelihood of the model divided by the model-independent likelihood of the exact measured tracer data and is used as a relative measure of how well the model represents the measurement values.

From the TTDs, one can clearly deduce, that the water from the sampled wells was composed of a mixture of a very young groundwater (< 100 years) and an older component. All wells except well 20 could be described by the model featuring a likelihood score of 83 and 100%. In well 19, the older component is dated to be of an age between 20000 and 50000 years and contributes about 70%. In the other wells, the younger component is dominant with a contribution of about 60%.

The hydrological system of the Salalah Plain was previously estimated to feature groundwater ages ranging between decades up to some centuries (Clark et al. 1987). With this new approach of a multi-tracer study and a shape-free age histogram TTD, it was possible to show that the water supply drawn from the studied wells is composed of a mixture of two distinct components, one of which has a high age above 1000 years. These findings can offer valuable information about groundwater renewal in the Salalah Plain, as older groundwater bodies often feature lower flow rates[6]. A larger data set would be necessary for a large-scale assessment of the geo-hydrological system below the Salalah Plain. But it could be shown, that the combined use of the dating tracers CFC-11, ^{39}Ar and ^{14}C can be sufficient to infer a reliable TTD estimation.

---

[6] This conclusion can e.g. be drawn from the determination of the mean age of a box flow model (compare chapter 4.6.4): There, the mean age $\bar{\alpha}$ of a water body is determined by the flowrate and the volume as: $\bar{\alpha} = V/\dot{V}$.

7. Discussion, conclusions and outlook

The work presented in this thesis is the result of four and a half years of working on and with ^{39}Ar ATTA, including its applications to different environmental systems. The aim of these final remarks will be to critically discuss some aspects of the presented work and to find and discuss approaches for improvements and future developments.

7.1. Lake Kivu ATTA

Extensive work has been performed to measure the first ^{39}Ar profile of a lake system. The dynamics of lakes often play out on timescales of days or months, so a meromictic lake with long term dynamics represents an ideal site for ^{39}Ar to be an applicable tracer. With dynamics assumed to happen on timescales of hundreds of years, the strongly stratified Lake Kivu was therefore an ideal system to study with ^{39}Ar ATTA.

In collaboration with partners from the Swiss Federal Institute of Aquatic Science and Technology (EAWAG), a sampling campaign was initiated in early 2018. This campaign was a collaborative effort to investigate the development of Lake Kivu's gas reserves and to assess potential changes in the hazard level that this lake poses. Following this campaign, several new insights on Lake Kivu could be published (Bärenbold et al. 2021; Bärenbold et al. 2020c; Boehrer et al. 2019; Schmid et al. 2019). One of the most interesting findings elucidated the development of Lake Kivu's gas content during the last 50 years (Bärenbold et al. 2020b). It could be shown that the gas concentration in the lake did not change significantly since 1974. When considering today's status quo as a result of a development over the last about 1000 years since the last degassing event (Ross et al. 2014), it is remarkable to see Lake Kivu in seemingly a steady state with only about 60% solute saturation at its maximum. A previously assumed linear gas accumulation dynamic should be significant over 50 years.

The gas accumulation in Lake Kivu is directly coupled to the strong volcanism along the East African Rift, in particular the neighboring volcano Nyiragongo. Since the volcanism of Nyiragongo is dynamic and changing over time, it is possible that the gas accumulation dynamics are underlying similar fluctuations (Tedesco et al. 2007). To better understand the dynamics of the coupled system of gas, volcanism and lake stratification, a ^{39}Ar analysis could provide insights on the long-term dynamics of Lake Kivu's stratification.

The field work and sampling for the analysis presented in this thesis posed significant challenges due to the high gas contents in Lake Kivu, which also led to the loss of most of the samples gathered in 2018. The high amounts of CO_2 and CH_4 in the lake dilute the targeted argon by a factor of up to 100, thus making the sampling process much more vulnerable to leakage. Therefore, an improved sampling setup was developed that decreased the chance of contamination with ambient air. With this improved setup, a second sampling campaign was planned and successfully performed in 2019.

The planning and execution of this second campaign was accomplished as part of this PhD project.

Compared to the samples normally studied with ATTA, the samples of Lake Kivu were very unique due to their high concentrations of CO_2 and CH_4 and the presence of highly corrosive H_2S. An additional getter setup had to be developed in order to chemically remove H_2S and CH_4 with copper wool and hot CuO, respectively. The CO_2 could be removed by freezing it in steel traps at liquid nitrogen temperatures. With these additional measures, pure argon samples of volumes from 0.6 to 1.7 ml$_{STP}$ could be prepared from the lake water samples for ATTA measurements.

Surprisingly, the ATTA measurements of the lake profile showed highly enhanced ^{39}Ar concentrations in the layer between 253 and 360 m. Unfortunately, the measurements of the samples from 280 m deviated significantly with measured ^{39}Ar values between $2.72^{+0.42}_{-0.35}$ R$_A$ and $5.93^{+0.60}_{-0.54}$ R$_A$. The origin of this significant deviation could not be reconstructed. To the best of our knowledge, both measurements were free of errors and no error sources could be observed during sampling either. The most probable source of error is the process of sample preparation. During this process, several vacuum-tight connections are opened and closed when installing the sample container at the separation machine and when replacing used getter material. Even though these connections are helium leak-tested after each change, a flawed connection could have slipped through the control procedures. The risk for such an error could also have been increased further by the additional installations at the sample preparation line. Assuming that an atmospheric contamination is the most probable source of error means that the measurement closer to R$_A$ (here: $2.72^{+0.42}_{-0.35}$ R$_A$) is the flawed one and it could be argued to limit the analysis to using the other, higher measurement value. However, since it is not possible to completely rule out the lower measurement, it was decided to analyze all three possible combinations. Means to determine contamination errors are discussed further below as well.

The analysis of the ^{39}Ar distribution in Lake Kivu was performed with the help of a 1D-simulation of Lake Kivu based on the software package Simstrat (Bärenbold 2020a). This model simulates the water column of Lake Kivu in dependence of several external influences like groundwater inflow, surface water in- and outflow, precipitation, evaporation, microbial methanogenesis among others. All these parameters were adjusted carefully so that Lake Kivu and its development over several hundreds of years could be simulated (Bärenbold 2020a). With this adjusted model, the isotopic abundance of ^{39}Ar could be introduced as an additional property of the inflows. Fitting routines were used to adjust the ^{39}Ar isotopic abundance of the inflow so that the resulting abundance in the water column fits the measurement values.

Shortly before finishing this thesis, an error in the chosen model parameters was discovered. The model and the presented results were achieved by simulating the isotopic abundance ^{39}Ar/Ar as a parameter. This turned out to be imprecise because the total amount of argon solved in the groundwater inflows is not uniform across inflows. In fact, the total argon amount in the water column decreases with depth, down to a value of about 40% at 408 m compared to the surface. We estimated that a

corrected simulation would change the simulation results quantitatively, but qualitative changes are expected to be minor. Even though a new simulation is possible, it would take at least two months of calculation time alone. Therefore, the inaccurate obtained simulation results were presented and discussed in this thesis. An updated simulation will be calculated and published subsequently to this thesis.

Interestingly, the simulation results at hand showed unexpectedly high ^{39}Ar isotopic abundances in two of Lake Kivu's groundwater intrusions. Those abundances are higher than any observations described previously. The origin of these high abundances can likely be suspected in the geogenic production of ^{39}Ar*. Extensive work in this field was done by R. Yokochi and R. Purtschert (Yokochi et al. 2013; Yokochi et al. 2012). Geogenic ^{39}Ar* production can be linked to young rock with high production rates, of which there might be plenty in the East African Rift due to the local volcanic activity. With knowledge about geogenically produced ^{40}Ar*, the groundwater residence times in the ^{39}Ar* and ^{40}Ar* producing rock could also be calculated.

In order to investigate the hydrodynamics of Lake Kivu, the simulation results were used to create a Transit Time Distribution of Lake Kivu. The results were obtained by comparing the measured abundances of ^{39}Ar with a specific set of simulations that assumed ^{39}Ar to be stable instead of radioactive. This approach is not ideal, as it gives a TTD in units of apparent age and not real age. Nevertheless, it showcases the capabilities of a simulation program like Simstrat and gives a very good qualitative description of the dynamics of solutes in Lake Kivu's water column. Improvements can be achieved by introducing a simulated age parameter that increases with every simulation time step and is mixed with the same dynamics as water or the solute of interest. An extension of Simstrat with such a mechanism seems very promising for future studies.

One very important aspect leading to the success of the whole Lake Kivu project was the collaboration with external experts and particularly our local partners in Rwanda. During this project and the planning and execution of two field trips, partnerships were built up with all sides mutually benefitting from the work of each other. Those partnerships are incredibly valuable and it is of personal importance to me to emphasize the significance of keeping them alive in the future.

7.2. Lake Kivu TDG

In this work, an approach to extend the capabilities of a total dissolved gas (TDG) probe was explored. The TDG probe consists of a standard pressure sensor in a small volume, which has a gas permeable membrane towards the water. The gasses dissolved in water diffuse through the membrane until an equilibrium is reached following Henry's law. The resulting pressure is the total dissolved gas pressure. The idea behind this project was that different gas species diffuse through the membrane at different velocities, so that the partial pressures of different gas species could possibly be calculated by fitting the dynamics of the recorded pressure changes with a double limited exponential growth model.

Analyzing the pressure recordings in Lake Kivu showed that this method works, but also exposed some limitations and unresolved irregularities regarding the pressure change dynamics. In order to investigate this method systematically in a controlled environment, a device was constructed to simulate the TDG measurements in Lake Kivu. The experimental setup allowed for a series of measurements with gas phase gasses and water-equilibrated gasses, both in pure form and in mixtures. The processes of gas phase diffusion compared to a solute phase diffusion showed similar results for CO_2 but fundamentally different results for CH_4. It seems that CH_4 in aqueous solution is barely able to penetrate the PTFE membrane, which might be due to hydrogen bond network effects. It could also be shown that the diffusion of CO_2 and CH_4 mixtures from a solute phase through the membrane is a coupled process and that CO_2 seems to function as a catalyst for the CH_4 diffusion. A measurement resembling the measurements in Lake Kivu could be reproduced once.

The experimental results gathered in this work provided interesting insights into the interactions of solute gasses and PTFE membranes, although some questions could not be answered and would require further analysis (e.g. using molecular dynamics simulations). In order to empirically validate the constrained successful measurements at Lake Kivu, the measurement method could be repeated several times, maybe even on other gas carrying meromictic lakes. Such campaigns were planned, but could not be executed due to the Covid-19 pandemic. It could also be worthwhile to send our probe to our local partners at Lake Kivu in order to achieve validation.

Judging from the presented findings, using a TDG probe could still be a promising approach in the search for a precise and easy-to-use method for determining partial pressures. Thus, further work on the validation or on optimization attempts are reasonable and should be pursued.

7.3. Ocean, ice and groundwater

In chapter 6, a summary of those ATTA measurements that were performed during this PhD project and belonged to three additional projects is presented. These three projects give a good impression of the versatility of ^{39}Ar dating in the environmental sciences.

In the Leupa Ice Cave, the formation of its ice sheet could be constrained to a period between the end of the Little Ice Age and the beginning of the anthropogenic climate warming with the performed ATTA measurements. Because this period is close to the limit of the ^{39}Ar dating range at about 50 years, the precision of the dating was not ideal, meaning that for some samples, the tracer age error was close to the determined tracer age (e.g. #5: 127^{+84}_{-73} a and #6: 68^{+76}_{-60} a). For a more precise age determination, a second dating tracer for younger ages would be helpful and should be considered for future projects (e.g. CFCs, SF_6, ^{85}Kr, ^{3}He).

The measurement results for the three ocean samples from the northern Atlantic were performed to explore the potential of an ^{39}Ar sampling in the Labrador Sea for investigating the formation of the North Atlantic Deep Water. An interesting inverted

age profile with younger water below an older layer could be observed. Such inversions can hint at distinct water bodies. During an earlier ocean ventilation study, it was found that for such investigations, the combination with a tracer for younger ages can be crucial as well (Ebser et al. 2018b).

The third campaign presented in this chapter was a multi-tracer groundwater study in the Salalah Plain in southern Oman. In this study, sampling for a variety of tracers was performed to test their suitability for the system. After considering all tracer measurements, three dating tracers were seen fit for analysis to determine a TTD. CFC-11, ^{39}Ar and ^{14}C were successfully used to determine a TTD using two different methods, an advective-dispersive model and a non-parametric shape free age histogram TTD model with six bins. It could be shown that the groundwater system probed by the wells consists of two different water bodies with one featuring a high age > 1000 years, with some wells even higher than 20 000 years. For solid implications regarding the whole groundwater system below the Salalah Plains, some more probing would be advisable. But even as a preliminary result, the discovery of the two different water bodies can give some insights, especially regarding the local water supply increasingly strained by crop irrigation.

All three studies described above show the importance of multi-tracer approaches when investigating environmental systems. Every dating tracer has a sweet spot for precision and especially at the limits of their applicability, the combined use of several tracers is advisable. The second reason for a multi-tracer approach is water body mixing that occurs in the environment and can create complex TTDs. The more measurement values that can be obtained, the more tightly constrained the parameter space describing a TTD becomes and the more information can be inferred.

7.4. ATTA performance

Deciding whether or not a measured sample is contaminated by air or not is a big problem with ^{39}Ar ATTA measurements. A suitable method to check for modern air contamination of old samples would be to look for dating tracers that cover younger ages. Checking samples for ^{85}Kr, CFCs or SF_6 could give an indication of unexpectedly large influences of modern air. However, a younger age contribution could be systematic and not due to contamination, especially for systems with strong mixing.

A very interesting recent development was presented by (Ringena 2021). By equipping the ATTA machine used in this work with a secondary laser system, a dual ATTA machine for the detection of both ^{39}Ar and ^{85}Kr was built. The ability to measure both ^{39}Ar and ^{85}Kr would enable determinations of more complex TTDs. Additionally, the influence of young air on old samples, i.e. possible contaminations, could be explored when in doubt. Measuring both isotopes in the same machine and in the same measurement run offers the advantage of less required preparation and machine time.

Besides the potential influence of contamination during sampling or preparation, the precision of an ATTA measurement is the other major challenge of this method. With its extremely low abundance of ^{39}Ar/Ar = 8.1 x10^{-16}, the atom count rates of ^{39}Ar ATTA

are crucial and often subject to optimization efforts. As described before, the atom count rates during the last five years fluctuated between 2.5 and 7 atoms/h and are currently (August 2021) stagnant at around 4 atoms/h. Optimization by improving alignment of every component of the ATTA machine is a tedious effort, as the signal which needs to be optimized is the very small count rate. However, alternative tools have been developed in the past. The beam imaging tool is a powerful tool to align the atom beam by looking at the ^{40}Ar fluorescence behind the MOT chamber. Collimator and MOL can be aligned very precisely with this beam imaging. To optimize the beam alignment at the MOT, another tool was developed to measure MOT loading rates of the isotope ^{38}Ar. Although both tools work very well, they have limitations. The process of capturing ^{39}Ar is somewhat different compared to the mentioned stable isotopes because ^{39}Ar has a nuclear spin and thus, a hyperfine structure. The influence of the repumper lasers, for example, cannot be optimized by looking at ^{38}Ar and ^{40}Ar. An optimization routine to directly influence the ^{39}Ar count rate can only be achieved by extensively measuring enriched ^{39}Ar sample (e.g. the 10x reference) and slowly changing all parameters, e.g. repumper frequencies. When aiming for a precision of around 10%, each measurement would take 2 hours. Thus, it becomes clear that such an optimization endeavor that includes varying several frequencies would take several weeks to cover the whole parameter space. Nevertheless, maybe this could be a path towards a significantly optimized ATTA.

Metastable argon production might have the highest potential for improving ATTA precision. The process of ionization and electron capture is highly inefficient with an efficiency factor around 2×10^{-3} (Ritterbusch 2013). An alternative metastable generation method could be optical excitation. The group of Zheng-Tian Lu recently published their successful attempt to run a ^{81}Kr ATTA with optical metastable ^{81}Kr generation (Wang et al. 2021). The working principle is to run a gas discharge, equivalent to the 'classical' metastable generation, and using the 124 nm photons produced by this process to generate metastable ^{81}Kr. The presented ^{81}Kr 124 nm lamp is depicted in Figure 54. The gas discharge is separated from the atom beam by a MgF_2 window with a transmissivity of about 70% at 124 nm.
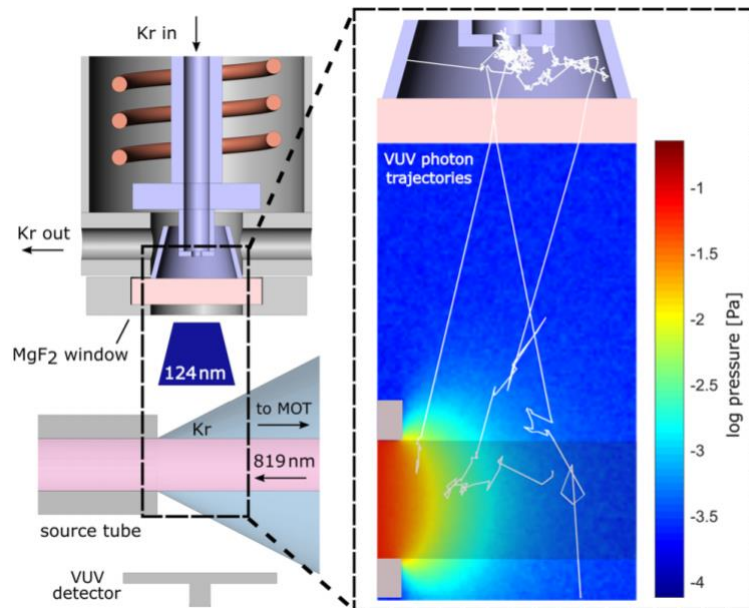
Figure 54: Metastable ^{81}Kr generation by optical excitation. A krypton discharge produces 124 nm photons which are required to drive the transition ($1s_{1(J=0)} \rightarrow 1s_{4(J=1)}$) that is necessary for metastable ($1s_{5(J=2)}$) generation. Figure from (Wang et al. 2021).

The optical excitation provided similar results for their ^{81}Kr ATTA performance compared to the metastable generation by RF-discharge. Wang et al. (2021) claim, however, that this process should be scalable with more 124 nm photons, i.e. more lamps. Notably, the transfer of this innovation to ^{39}Ar is limited by currently available materials. ^{39}Ar would require a window material with a significant transmissivity at 107 nm, which to our knowledge is not available at this time.

7.5. Outlook

During the last six years, the applicability of ^{39}Ar dating with ATTA on environmental systems was extended drastically. By reducing the required sample size down to the range of 0.5 mL$_{STP}$ argon, ^{39}Ar ATTA studies with water samples from remote places like the Atlantic (Ebser et al. 2018b), the Labrador Sea, southern Oman and from the middle of Lake Kivu in Central Africa became feasible. The expansion towards ice samples enabled studies on glacier ice (Feng et al. 2019b) and ice sheets in remote ice caves like Leupa. Ongoing efforts explore the expansion of the system's capabilities to permafrost ground. Developments presented in this thesis explored the feasibility of analyzing difficult samples that contain corrosive or strongly diluting gasses.

A very recent innovation at the Heidelberg ATTA facility is an extension of our laser setup enabling ^{85}Kr dating in the same machine (Ringena 2021). This new method could be the key towards a combined ^{85}Kr and ^{39}Ar measurement of environmental samples during the same measurement run without a significant increase in measurement time. Such an additional measurement can be vital for determining precise age distributions of environmental systems of interest.

Now that several successful innovations have enabled [39]Ar ATTA to expand towards more and more realms of the environment, future developments should focus on increasing the measurement capacity in my opinion. Several steps on this path were already taken by developing a second [39]Ar ATTA facility in Heidelberg (Feng 2019a; Ringena 2021). Other previously taken measures are of smaller scale but nevertheless highly important. Examples for those are the many little upgrades on the machine that are made every week, be it an improved control network or an easier-to-use vacuum setup. Another example in this category would also be the improved and easy-to-use sample analysis software described in this thesis. However, the count rate has the biggest potential to improve measurement capacity, since it is directly proportional to the number of samples that can be measured in a defined time period. The highest achieved count rate in our facility is 7 atoms/h, while count rates around 10 atoms/h could be achieved recently in the facility of the group of Zheng-Tian Lu (Tong et al. 2021). Large optimization potential for the count rate lies in new developments regarding the generation of metastable [39]Ar*. The optical excitation has already been discussed above. Recent developments in our facility led to the design of an innovative RF-discharge source. This source changed the open RF-antenna design into a helical resonator, running with much less RF-power and thus potentially reducing the thermal energy transferred towards the argon atoms. Future investigations during the PhD project of Julian Robertz will determine the effectiveness of this innovative source design.

When the capacity can be increased by a decent amount in the future, it will be interesting to consider which environmental systems would be of the highest interest for a large-scale [39]Ar dating campaign. Among the most important systems could be global ocean circulations like the Gulf Stream. These types of circulations are threatened by the rapidly changing climate and changes in them could affect large parts of our planet and our global society in dramatic ways (IPCC 2021). Thus, large-scale [39]Ar dating campaigns could support efforts to understand and better predict these fragile and highly influential systems.

8. Appendix

8.1. Determination of the apparent age from the mean age
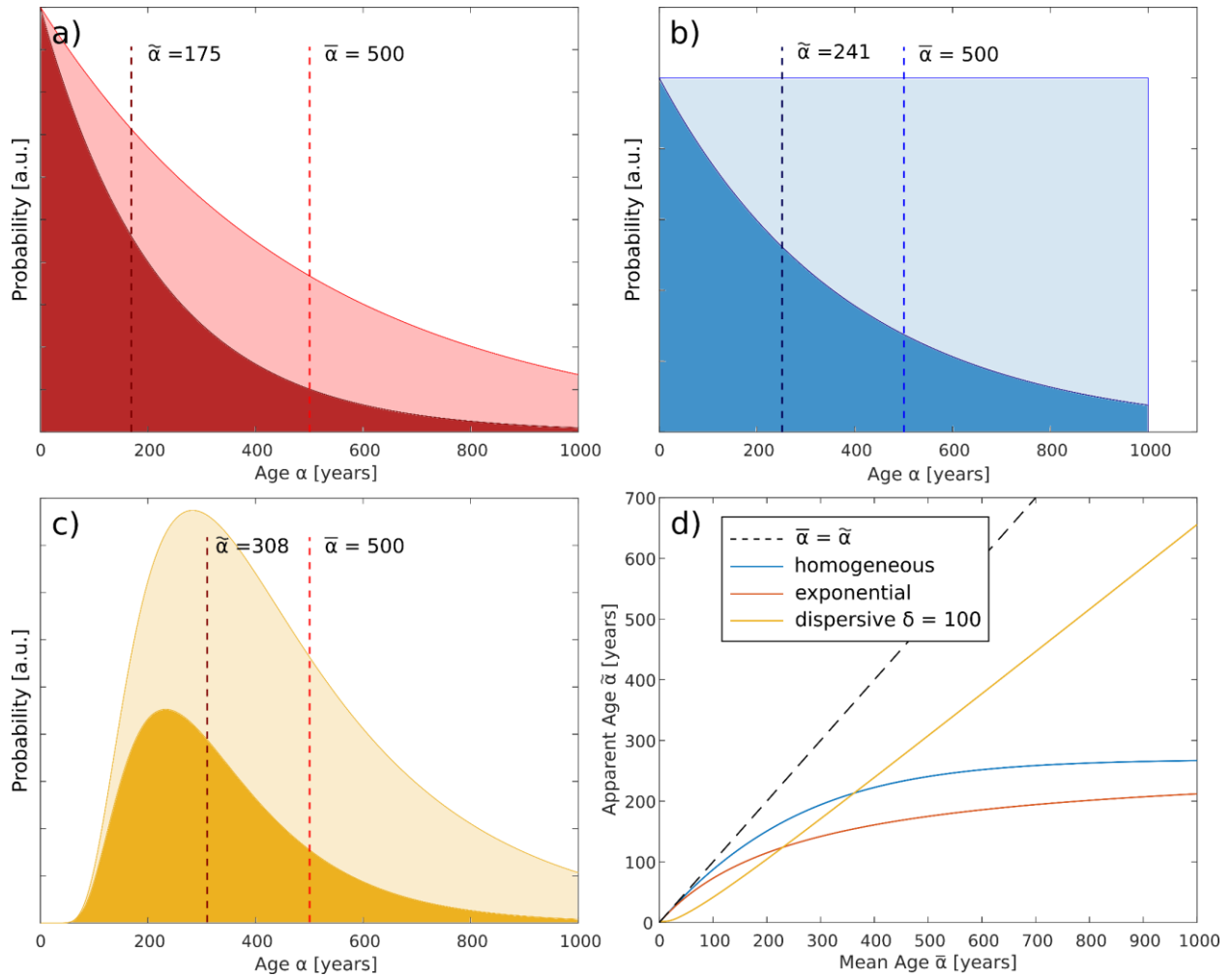

Figure 55: Different TTDs showing the relation between mean age $\bar{\alpha}$ and apparent mean age $\tilde{\alpha}$ for different age distributions. a) Exponential distribution b) Homogeneous distribution c) Advective dispersive model $\delta = 100$. a), b) & c): light color: The age distribution with a mean age of 500 years. Dark color: the same distribution now including a radioactive decay with $T\frac{1}{2}$ = 269 years leading to a different apparent age. d)) Dependence of the apparent age $\tilde{\alpha}$ from the mean age $\bar{\alpha}$ and the shape of the age distribution.

Variables for all calculations:

age: α
mean age: $\bar{\alpha}$
apparent age: $\tilde{\alpha}$
half-life: $T_{1/2}$ $(= 269\ a)$
life-time: τ $\left(= \dfrac{T_{1/2}}{\ln(2)} = 388\ a\right)$

stepfunction: $\theta(0,2\bar{\alpha}) = \begin{cases} 1 \mid 0 \le \alpha \le 2\bar{\alpha} \\ 0 \mid else \end{cases}$

normalization factors: $\gamma, \xi, \varepsilon, \vartheta$

8.1.1. Exponential model

The probability density function of the exponential model P is:

$$P(\alpha, \bar{\alpha}) = \frac{\ln(2)}{\bar{\alpha}} \cdot \exp\left(-\frac{\ln(2) \cdot \alpha}{\bar{\alpha}}\right)$$

According to the radioactive decay, with a new normalisation factor γ, this transforms to:

$$P(\alpha, \bar{\alpha}, \tau) = \gamma \cdot \exp\left(-\frac{\ln(2) \cdot \alpha}{\bar{\alpha}}\right) \cdot \exp\left(-\frac{\ln(2) \cdot \alpha}{T_{1/2}}\right)$$

$$= \gamma \cdot \exp\left(-\frac{\ln(2) \cdot \alpha}{\bar{\alpha}} - \frac{\ln(2) \cdot \alpha}{T_{1/2}}\right) = \gamma \cdot \exp\left(-\alpha \cdot \left(\frac{\ln(2)}{\bar{\alpha}} + \frac{\ln(2)}{T_{1/2}}\right)\right)$$

$$= \gamma \cdot \exp\left(-\alpha \cdot \underbrace{\left(\frac{\ln(2)}{\bar{\alpha}} + \frac{\ln(2)}{T_{1/2}}\right)}_{=\gamma}\right) = \left(\frac{\ln(2)}{\bar{\alpha}} + \frac{\ln(2)}{T_{1/2}}\right) \cdot \exp\left(-\alpha \cdot \left(\frac{\ln(2)}{\bar{\alpha}} + \frac{\ln(2)}{T_{1/2}}\right)\right)$$

$$= P(\alpha, \bar{\alpha}, \tau)$$

The apparent age $\tilde{\alpha}$ is equivalent to the median of this distribution:

$$\int_0^{\tilde{\alpha}} P(\alpha, \bar{\alpha}, \tau)\, d\alpha \equiv \frac{1}{2}$$

$$= \int_0^{\tilde{\alpha}} \gamma \cdot \exp(-\alpha \cdot \gamma)\, d\alpha = [-\exp(-\alpha \cdot \gamma)]_0^{\tilde{\alpha}}$$

$$= 1 - \exp(-\tilde{\alpha} \cdot \gamma) = \frac{1}{2}$$

$$\Leftrightarrow \tilde{\alpha} = \frac{\ln(2)}{\gamma} = \frac{\ln(2)}{\dfrac{\ln(2)}{\bar{\alpha}} + \dfrac{\ln(2)}{T_{1/2}}} = \frac{\bar{\alpha} \cdot T_{1/2}}{\bar{\alpha} + T_{1/2}} = \tilde{\alpha}$$

8.1.2. Homogeneous model

The probability density function of the homogeneous model P is:

$$P(\alpha, \bar{\alpha}) = \frac{1}{2\bar{\alpha}} \cdot \theta(0, 2\bar{\alpha})$$

According to the radioactive decay, with a new normalisation factor ξ[7], this transforms to:

$$P(\alpha, \bar{\alpha}, \tau) = \xi \cdot \exp\left(-\frac{\alpha}{\tau}\right) \cdot \theta(0, 2\bar{\alpha})$$

Normalisation:

$$\int_0^{2\bar{\alpha}} \xi \cdot \exp\left(-\frac{\alpha}{\tau}\right) d\alpha \equiv 1$$

$$= \left[-\xi \cdot \tau \cdot \exp\left(-\frac{\alpha}{\tau}\right)\right]_0^{2\bar{\alpha}} = \xi \cdot \tau \cdot \left(1 - \exp\left(-\frac{2\bar{\alpha}}{\tau}\right)\right)$$

$$\Leftrightarrow \xi = \frac{1}{\tau} \cdot \underbrace{\frac{1}{\left(1 - \exp\left(-\frac{2\bar{\alpha}}{\tau}\right)\right)}}_{=\varepsilon} = \frac{1}{\tau \cdot \varepsilon}$$

Median:

$$\int_0^{\tilde{\alpha}} \frac{1}{\tau \cdot \varepsilon} \cdot \exp\left(-\frac{\alpha}{\tau}\right) d\alpha \equiv \frac{1}{2}$$

$$= \left[-\frac{1}{\varepsilon} \cdot \exp\left(-\frac{\alpha}{\tau}\right)\right]_0^{\tilde{\alpha}} = \frac{1}{\varepsilon} \cdot \left(1 - \exp\left(-\frac{\tilde{\alpha}}{\tau}\right)\right)$$

$$\Leftrightarrow -\frac{\tilde{\alpha}}{\tau} = \ln\left(1 - \frac{\varepsilon}{2}\right)$$

$$\Leftrightarrow \tilde{\alpha} = -\tau \cdot \ln\left(1 - \frac{\varepsilon}{2}\right) = -\tau \cdot \ln\left(1 - \frac{\left(1 - \exp\left(-\frac{2\bar{\alpha}}{\tau}\right)\right)}{2}\right)$$

$$\Leftrightarrow \tilde{\alpha} = -\tau \cdot \ln\left(\frac{1}{2} + \frac{1}{2} \cdot \exp\left(-\frac{2\bar{\alpha}}{\tau}\right)\right)$$

8.1.3. Equal binary mix

The equal binary mixture describes a system with mean age $\bar{\alpha}$ composed of two equally large parts, one with age 0 and one with age $2\bar{\alpha}$. The apparent age $\tilde{\alpha}$ can directly be calculated by looking at the mean tracer abundance $c(\bar{\alpha})$ in a mixture of mean age $\bar{\alpha}$:

---

[7] Congratulations! You found the hidden footnote! Contact me via schmidtmags@gmail.com for a free beer!

$$c(\bar{\alpha}) = \frac{1}{2} + \frac{1}{2} * \exp\left(-\frac{2\bar{\alpha}}{\tau}\right)$$

By calculating the apparent age $\tilde{\alpha}$ from this concentration one gets the equivalent result to the apparent age in the homogeneous model:

$$\tilde{\alpha} = -\tau \cdot \ln\left(\frac{1}{2} + \frac{1}{2} \cdot \exp\left(-\frac{2\bar{\alpha}}{\tau}\right)\right)$$
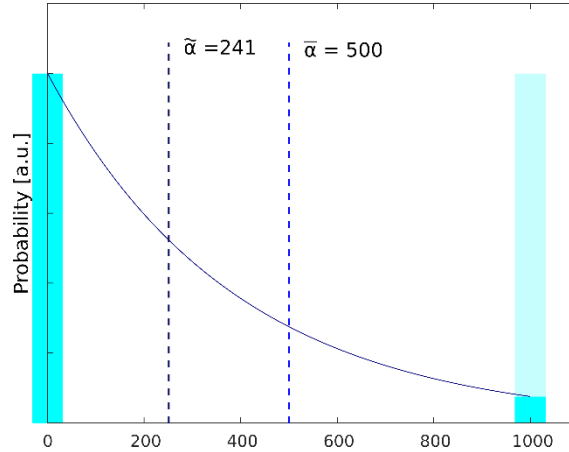

Figure 56: Age versus apparent age for the equal binary mixture, represented by δ functions at age 0 and at age 1000 (= 2$\bar{\alpha}$). The resulting apparent age is equivalent to the one in homogeneous mixture.

8.1.4.   Dispersive model

The probability density function of the advective/dispersive model P with dispersivity factor δ is:

$$P(\alpha, \bar{\alpha}) = \sqrt{\frac{\bar{\alpha}}{4\pi\delta\alpha^3}} \exp\left(-\frac{(\alpha - \bar{\alpha})^2}{4\delta\bar{\alpha}\alpha}\right)$$

The dispersivity factor δ in another convention is defined as the Peclét-Number $Pe = 1/\delta$. Accounting for the radioactive decay, with a new normalisation factor ϑ, this transforms to:

$$P(\alpha, \bar{\alpha}, \tau) = \vartheta \cdot \sqrt{\frac{\bar{\alpha}}{4\pi\delta\alpha^3}} \exp\left(-\frac{(\alpha - \bar{\alpha})^2}{4\delta\bar{\alpha}\alpha}\right) \cdot \exp\left(-\frac{\alpha}{\tau}\right)$$

The normalization and median determination has been done numerically via a MatLab skript.

8.2. Accidents
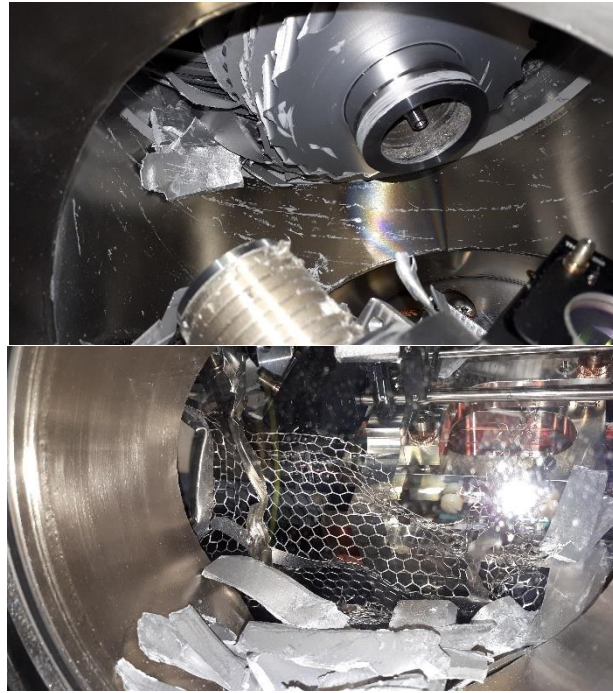
Figure 57: Destroyed TMPs and damaged source chamber and collimator. After a blackout in 2019, the uncontrolled shutdown of the two opposing 2000 l/s TMPs caused both rotors to crash, destroying large parts of the experimental setup.

9. Own Publications

Rädle, Viola; Kersting, A.; Schmidt, Maximilian; Ringena, Lisa; Robertz, Julian; Aeschbach, Werner et al. (2021): Multi-Tracer Groundwater Dating in Southern Oman by Bayesian Modelling (Paper draft). submitted to Water Resources Research. In *Preprint*.

Sprenger, Matthias; Stumpp, Christine; Weiler, Markus; Aeschbach, Werner; Allen, Scott T.; Benettin, Paolo; Schmidt, Maximilian et al. (2019): The Demographics of Water: A Review of Water Ages in the Critical Zone. In *Rev. Geophys.* 57 (3), pp. 800–834. DOI: 10.1029/2018RG000633.

Feng, Zhongyi; Bohleber, Pascal; Ebser, Sven; Ringena, Lisa; Schmidt, Maximilian; Kersting, Arne et al. (2019): Dating glacier ice of the last millennium by quantum technology. In *Proceedings of the National Academy of Sciences of the United States of America* 116 (18), pp. 8781–8786. DOI: 10.1073/pnas.1816468116.

Ebser, Sven; Kersting, Arne; Stöven, Tim; Feng, Zhongyi; Ringena, Lisa; Schmidt, Maximilian et al. (2018): 39Ar dating with small samples provides new key constraints on ocean ventilation. In *Nature communications* 9 (1), p. 5046. DOI: 10.1038/s41467-018-07465-7.

10. Bibliography

Aeschbach, Werner (2015): Aquatische Systeme. Vorlesungsskript.

ALLARD, P. (2002): The January 2002 Eruption of Nyiragongo Volcano (Dem. Repub. Congo) and Related Hazards: Observations and Recommendations. In *Submitted to : Ministry for Foreign Affairs, Paris, France Foreign Office, London, United Kingdom and respective Embassies in Democratic Republic of Congo and Republic of Rwanda*.

Al-Sarmi, Said; Al-Yahyai, Sultan; Al-Maskari, Juma; Charabi, Yassine; Choudri, B. S. (2017): Recent Observed Climate Change Over Oman. In Osman Abdalla, Anvar Kacimov, Mingjie Chen, Ali Al-Maktoumi, Talal Al-Hosni, Ian Clark (Eds.): Water Resources in Arid Areas: The Way Forward. Cham, s.l.: Springer International Publishing (Springer Water), pp. 89–100.

Andrews, J.N; Davis, S.N; Fabryka-Martin, J.; Fontes, J-Ch; Lehmann, B.E; Loosli, H.H et al. (1989): The in situ production of radioisotopes in rock matrices with particular reference to the Stripa granite. In *Geochimica et Cosmochimica Acta* 53 (8), pp. 1803–1815. DOI: 10.1016/0016-7037(89)90301-3.

Apel, H.; Thieken, A. H.; Merz, B.; Blöschl, G. (2004): Flood risk assessment and associated uncertainty. In *Nat. Hazards Earth Syst. Sci.* 4 (2), pp. 295–308. DOI: 10.5194/nhess-4-295-2004.

Balco, Greg (2020): Glacier Change and Paleoclimate Applications of Cosmogenic-Nuclide Exposure Dating. In *Annu. Rev. Earth Planet. Sci.* 48 (1), pp. 21–48. DOI: 10.1146/annurev-earth-081619-052609.

Ballhorn, Michael (2000): Entwicklung von Polymermembranen für die Abtrennung von Kohlendioxid aus Gasströmen. Doktorarbeit. RWTH Aachen, Aachen. Fakultät für Mathematik, Informatik und Naturwissenschaften.

Bärenbold, F. (2020a): Managing Lake Kivu: moving from a steady-state to a dynamic modelling approach. Doktorarbeit. Eidgenössische Technische Hochschule Zürich, Zürich.

Bärenbold, F.; Kipfer, R.; Schmid, M. (2021): Dynamic modelling provides new insights into development and maintenance of Lake Kivu's density stratification. In *Submitted*.

Bärenbold, Fabian; Boehrer, Bertram; Grilli, Roberto; Mugisha, Ange; Tümpling, Wolf von; Umutoni, Augusta; Schmid, Martin (2020b): No increasing risk of a limnic eruption at Lake Kivu: Intercomparison study reveals gas concentrations close to steady state. In *PloS one* 15 (8), e0237836. DOI: 10.1371/journal.pone.0237836.

Bärenbold, Fabian; Schmid, Martin; Brennwald, Matthias S.; Kipfer, Rolf (2020c): Missing atmospheric noble gases in a large, tropical lake: The case of Lake Kivu, East-Africa. In *Chemical Geology* 532, p. 119374. DOI: 10.1016/j.chemgeo.2019.119374.

Barrer, R. M.; Rideal, Eric K. (1939): Permeation, diffusion and solution of gases in organic polymers. In *Trans. Faraday Soc.* 35, p. 628. DOI: 10.1039/tf9393500628.

Bauer, Christian; Gros, Gerolf; Bartels, Heinz (Eds.) (1980): Biophysics and Physiology of Carbon Dioxide. Berlin, Heidelberg: Springer Berlin Heidelberg (Proceedings in Life Sciences).

Benetti, P.; Calaprice, F.; Calligarich, E.; Cambiaghi, M.; Carbonara, F.; Cavanna, F. et al. (2007): Measurement of the specific activity of 39Ar in natural argon. In *Nuclear Instruments and Methods in Physics Research Section A: Accelerators, Spectrometers, Detectors and Associated Equipment* 574 (1), pp. 83–88. DOI: 10.1016/j.nima.2007.01.106.

Beyersdorfer, Stefan (2016): Argon extraction from glacier ice and ocean water for dating with 39Ar - ATTA. Master Thesis. Universität Heidelberg, Heidelberg. Institut für Umweltphysik Heidelberg.

Boehrer, Bertram; Schultze, Martin (2008): Stratification of lakes. In *Rev. Geophys.* 46 (2). DOI: 10.1029/2006RG000210.

Boehrer, Bertram; Tümpling, Wolf von; Mugisha, Ange; Rogemont, Christophe; Umutoni, Augusta (2019): Reliable reference for the methane concentrations in Lake Kivu at the beginning of industrial exploitation. In *Hydrol. Earth Syst. Sci.* 23 (11), pp. 4707–4716. DOI: 10.5194/hess-23-4707-2019.

Brennwald, Matthias S.; Schmidt, Mark; Oser, Julian; Kipfer, Rolf (2016): A Portable and Autonomous Mass Spectrometric System for On-Site Environmental Gas Analysis. In *Environmental science & technology* 50 (24), pp. 13455–13463. DOI: 10.1021/acs.est.6b03669.

Breunig, Emelie (2020): Determining the partial pressures of CO2 and CH4 by using a gas selective membrane. Bachelorarbeit. Universität Heidelberg, Heidelberg. Institut für Umweltphysik Heidelberg.

Bucchignani, Edoardo; Mercogliano, Paola; Panitz, Hans-Jürgen; Montesarchio, Myriam (2018): Climate change projections for the Middle East–North Africa domain with COSMO-CLM at different spatial resolutions. In *Advances in Climate Change Research* 9 (1), pp. 66–80. DOI: 10.1016/j.accre.2018.01.004.

Buizert, Christo; Baggenstos, Daniel; Jiang, Wei; Purtschert, Roland; Petrenko, Vasilii V.; Lu, Zheng-Tian et al. (2014): Radiometric 81Kr dating identifies 120,000-year-old ice at Taylor Glacier, Antarctica. In *Proceedings of the National Academy of Sciences of the United States of America* 111 (19), pp. 6876–6881. DOI: 10.1073/pnas.1320329111.

Chakrabarti, Ramananda; Basu, Asish R.; Santo, Alba P.; Tedesco, Dario; Vaselli, Orlando (2009): Isotopic and geochemical evidence for a heterogeneous mantle plume origin of the Virunga volcanics, Western rift, East African Rift system. In *Chemical Geology* 259 (3-4), pp. 273–289. DOI: 10.1016/j.chemgeo.2008.11.010.

Chen; Li; Bailey; O'Connor; Young; Lu (1999): Ultrasensitive isotope trace analyses with a magneto-optical trap. In *Science (New York, N.Y.)* 286 (5442), pp. 1139–1141. DOI: 10.1126/science.286.5442.1139.

Clark, I. D.; Fritz, P.; Quinn, O. P.; Rippon, P. W.; Nash, H.; Sayyid, Barghash bin Ghalib al Said (1987): Modern and fossil groundwater in an arid environment: A look at the hydrogeology of Southern Oman. In *International Atomic Energy Agency (IAEA)*, pp. 167–187.

Collon, Philippe; Kutschera, Walter; Lu, Zheng-Tian (2004): Tracing noble gas radionuklides in the environment. In *Annu. Rev. Nucl. Part. Sci.* 54 (1), pp. 39–67. DOI: 10.1146/annurev.nucl.53.041002.110622.

Colucci, Renato; Bohleber, Pascal; Festi, D.; Luetscher, Marc; Aeschbach, Werner; Feng, Zhongyi et al. (2021): Little Ice Age cave ice revealed by intercomparison of state-of-the-art ice dating methods (Paper Draft).

Colucci, Renato; Luetscher, Marc; Forte, Emanuele; Vita, Francesca (2017): First alpine evidence of in situ Coarse Croygenic Cave Carbonates (CCCCOARSE). In *Geogr. Fis. Dinam. Quat.* (40), pp. 53–59.

Conti Nibali, V.; Pezzotti, S.; Sebastiani, F.; Galimberti, D. R.; Schwaab, G.; Heyden, M. et al. (2020): Wrapping Up Hydrophobic Hydration: Locality Matters. In *The journal of physical chemistry letters* 11 (12), pp. 4809–4816. DOI: 10.1021/acs.jpclett.0c00846.

Contour Global (2021): KivuWatt. Edited by Contour Global. Available online at https://www.contourglobal.com/asset/kivuwatt.

Descy, Jean-Pierre; Darchambeau, François; Schmid, Martin (2012): Lake Kivu. Dordrecht: Springer Netherlands.

Doepke, Daniel (2017): Modelling the thermal history of onshore Ireland, Britain and its offshore basins using low-temperature thermochronology. PhD Thesis. Trinity College Dublin.

Doevenspeck, Martin (2007): Lake Kivu's Methane Gas: Natural Risk, or Source of Energy and Political Security? In *Africa Spectrum* 2007 (Vol. 42), pp. 95–110.

Dunitz, Jack D.; Taylor, Robin (1997): Organic Fluorine Hardly Ever Accepts Hydrogen Bonds. In *Chrm. Eur. J* (3 No. i).

Ebser, Sven (2018a): Dating of Ice and Ocean Samples Dating of Ice and Ocean Samples with Atom Trap Trace Analysis of 39Ar. Doktorarbeit.

Ebser, Sven; Kersting, Arne; Stöven, Tim; Feng, Zhongyi; Ringena, Lisa; Schmidt, Maximilian et al. (2018b): 39Ar dating with small samples provides new key constraints on ocean ventilation. In *Nature communications* 9 (1), p. 5046. DOI: 10.1038/s41467-018-07465-7.

Feng, Zhongyi (2019a): Quantum technological dating of glacier ice from the last millennium and a new self-contained facility for routine measurements. Doktorarbeit Zhongyi Feng.

Feng, Zhongyi; Bohleber, Pascal; Ebser, Sven; Ringena, Lisa; Schmidt, Maximilian; Kersting, Arne et al. (2019b): Dating glacier ice of the last millennium by quantum technology. In *Proceedings of the National Academy of Sciences of the United States of America* 116 (18), pp. 8781–8786. DOI: 10.1073/pnas.1816468116.

Feucher, Charlène; Garcia-Quintana, Yarisbel; Yashayaev, Igor; Hu, Xianmin; Myers, Paul G. (2019): Labrador Sea Water Formation Rate and Its Impact on the Local Meridional Overturning Circulation. In *J. Geophys. Res. Oceans* 124 (8), pp. 5654–5670. DOI: 10.1029/2019JC015065.

Gauthier-Lafaye, F.; Weber, F.; Ohmoto, H. (1989): Natural fission reactors of Oklo. In *Economic Geology* 84 (8), pp. 2286–2295. DOI: 10.2113/gsecongeo.84.8.2286.

Gerber, Christoph; Vaikmäe, Rein; Aeschbach, Werner; Babre, Alise; Jiang, Wei; Leuenberger, Markus et al. (2017): Using 81Kr and noble gases to characterize and date groundwater and brines in the Baltic Artesian Basin on the one-million-year timescale. In *Geochimica et Cosmochimica Acta* 205, pp. 187–210. DOI: 10.1016/j.gca.2017.01.033.

Gill, Gary (2019): Symbion's Plans for Lake Kivu Energy Production by Gary Gill, Contracts Manager Symbion Energy. presentation and in person conversation to Maximilian Schmidt and David Wachs. Kigali, 2019.

Golemme, Gianni; Santaniello, Anna (2019): Perfluoropolymer/Molecular Sieve Mixed-Matrix Membranes. In *Membranes* 9 (2). DOI: 10.3390/membranes9020019.

Gregorio, S. de; Gurrieri, S.; Valenza, M. (2005): A PTFE membrane for the in situ extraction of dissolved gases in natural waters: Theory and applications. In *Geochem. Geophys. Geosyst.* 6 (9), n/a-n/a. DOI: 10.1029/2005GC000947.

Halbwachs; Tietze; Lorke; Mudaheranwa (2002): Investigations in Lake Kivu (East Central Africa) after the Nyiragongo Eruption of January 2002,. In *European Community Humanitarian Office. Communauté européenne - ECHO 1 rue de Genève* 2002.

Halbwachs, Michel; Sabroux, Jean-Christophe; Kayser, Gaston (2020): Final step of the 32-year Lake Nyos degassing adventure: Natural CO2 recharge is to be balanced by discharge through the degassing pipes. In *Journal of African Earth Sciences* 167, p. 103575. DOI: 10.1016/j.jafrearsci.2019.103575.

Haselmeier, Ralf; Holz, Manfred; Marbach, Wolfgang; Weingaertner, Hermann (1995): Water Dynamics near a Dissolved Noble Gas. First Direct Experimental Evidence for a Retardation Effect. In *J. Phys. Chem.* 99 (8), pp. 2243–2246. DOI: 10.1021/j100008a001.

Horn, Christin; Metzler, Philipp; Ullrich, Karen; Koschorreck, Matthias; Boehrer, Bertram (2017): Methane storage and ebullition in monimolimnetic waters of polluted mine pit lake Vollert-Sued, Germany. In *The Science of the total environment* 584-585, pp. 1–10. DOI: 10.1016/j.scitotenv.2017.01.151.

IPCC (2021): Climate Change 2021, The Physical Science Basis. IPCC AR6 WG1.

Jiang, W. (2021): Upper age limit of cosmogenic 39Ar dating extended to 1,800 years. Goldschmidt 2021. Goldschmidt Virtual 2021, 7/5/2021. Available online at https://2021.goldschmidt.info/goldschmidt/2021/meetingapp.cgi/Paper/5856, checked on 7/29/2021.

Jiang, W.; Williams, W.; Bailey, K.; Davis, A. M.; Hu, S-M; Lu, Z-T et al. (2011): 39Ar detection at the 10(-16) isotopic abundance level with atom trap trace analysis. In *Physical review letters* 106 (10), p. 103001. DOI: 10.1103/PhysRevLett.106.103001.

Kersting, Arne (2018): Dating of groundwater and ocean samples Dating of groundwater and ocean samples with noble gas radioisotopes – sample preparation and field applications. Doktorarbeit. Universität Heidelberg, Heidelberg. Institut für Umweltphysik Heidelberg.

Kling, G. W.; Clark M.A.; et al.; Wagner G.N. (1987): The 1986 Lake Nyos Gas Disaster in Cameroon, West Africa. In *Science* (236).

Kling, G. W.; Evans, W. C.; et al.; Hell, J. V. (2005): Degassing Lakes Nyos and Monoun: Defusing certain disaster. In *Proceedings of the National Academy of Sciences of the United States of America* (102).

Kwon, Young-Oh; Alexander, Michael A.; Bond, Nicholas A.; Frankignoul, Claude; Nakamura, Hisashi; Qiu, Bo; Thompson, Lu Anne (2010): Role of the Gulf Stream and Kuroshio–Oyashio Systems in Large-Scale Atmosphere–Ocean Interaction: A Review. In *Journal of Climate* 23 (12), pp. 3249–3281. DOI: 10.1175/2010JCLI3343.1.

Loosli, H. H. (1983): A dating method with39Ar. In *Earth and Planetary Science Letters* 63 (1), pp. 51–62.

Loosli, H. H.; Heimann, Martin; Oeschger, Hans (1980): Low-Level Gas Proportional Counting in An Underground Laboratory. In *Radiocarbon* 22 (2), pp. 461–469. DOI: 10.1017/S0033822200009772.

Loosli, H. H.; Lehmann, B. E.; Balderer, W. (1989): Argon-39, argon-37 and krypton-85 isotopes in Stripa groundwaters. In *Geochimica et Cosmochimica Acta* 53 (8), pp. 1825–1829. DOI: 10.1016/0016-7037(89)90303-7.

Loosli, H. H.; Möll, H.; Oeschger, Hans; Schotterer, U. (1986): Ten years low-level counting in the underground laboratory in Bern Switzerland. In *Nuclear Instruments and Methods in Physics Research* (B17), pp. 402–405.

Lorke, Andreas; Tietze, Klaus; Halbwachs, Michel; Wüest, Alfred (2004): Response of Lake Kivu stratification to lava inflow and climate warming. In *Limnol. Oceanogr.*, pp. 778–783.

Lu, Z.-T.; Schlosser, P.; Smethie, W. M.; Sturchio, N. C.; Fischer, T. P.; Kennedy, B. M. et al. (2014): Tracer applications of noble gas radionuclides in the geosciences. In *Earth-Science Reviews* 138, pp. 196–214. DOI: 10.1016/j.earscirev.2013.09.002.

MacDonald, Alan; Davies, Jeff; Calow, Roger; Chilton, John (Eds.) (2005): Developing Groundwater. 2.4.5 Volcanic terrains P 23. Rugby, Warwickshire, United Kingdom: Practical Action Publishing.

Mackintosh, Andrew N.; Anderson, Brian M.; Pierrehumbert, Raymond T. (2017): Reconstructing Climate from Glaciers. In *Annu. Rev. Earth Planet. Sci.* 45 (1), pp. 649–680. DOI: 10.1146/annurev-earth-063016-020643.

Mertens, Christian (2015): Short Cruise Report MARIA S. MERIAN MSM 43.

Metcalf, Harold J.; van der Straten, Peter (2002): Laser cooling and trapping. 2nd ed. Heidelberg: Springer.

Moore, Charlotte E. (1971): Atomic energy levels as derived from the analyses of optical spectra: volume I. 1H to 23V.

MSM43 (2015): Expeditionsheft zu den Reisen MSM 41 - 43. In *Institut für Meereskunde Universität Hamburg*.

NASA (1976): U.S. Standart Atmosphere. In *NASA*.

NCSI Oman (2021): Water Production of Oman 2011 - 2019. Edited by Sultanate of Oman, Ministery of Technology and Communication. Available online at https://data.gov.om/OMWTR2016/water, updated on 6/29/2021, checked on 8/22/2021.

Nobel Foundation (2021): Nobel Prizes for Physics. Available online at https://www.nobelprize.org/prizes/lists/all-nobel-prizes-in-physics/, checked on 8/22/2021.

OCHA (2021): DR Congo: Volcano Nyiragongo - May 2021. Available online at https://reliefweb.int/disaster/vo-2021-000059-cod, checked on 9/4/2021.

Oey, L.-Y.; Ezer, T.; Lee, H.-C. (2013): Loop Current, Rings and Related Circulation in the Gulf of Mexico: A Review of Numerical Models and Future Challenges. In : Circulation in the Gulf of Mexico: Observations and Models. Washington, D. C.: American Geophysical Union, pp. 31–56.

Oki, Taikan; Kanae, Shinjiro (2006): Global hydrological cycles and world water resources. In *Science (New York, N.Y.)* 313 (5790), pp. 1068–1072. DOI: 10.1126/science.1128845.

Peeters (1957): Contribution a l'etude de la genese du lac Kivu. Peeters_Bull_Soc_Belg_Geogr_1957_Kivu_formation. In *Bulletin de la Societe Belge d'Etudes Geographiques*.

Pouclet (1975): Histoire des grands lacs de l'Afrique centrale mise au point des connaissances actuelles. In *Rev_Geogr_Phys_Geol_Dyn*.

Pouclet, A.; Bellon, H.; Bram, K. (2016): The Cenozoic volcanism in the Kivu rift: Assessment of the tectonic setting, geochemistry, and geochronology of the volcanic activity in the South-Kivu and Virunga regions. In *Journal of African Earth Sciences* 121, pp. 219–246. DOI: 10.1016/j.jafrearsci.2016.05.026.

Pouclet, André; Bram, Kurt (2021): Nyiragongo and Nyamuragira: a review of volcanic activity in the Kivu rift, western branch of the East African Rift System. In *Bull Volcanol* 83 (2). DOI: 10.1007/s00445-021-01435-6.

Rädle, Viola (2019): Multi-tracer study for groundwater dating in Southern Oman. Masterarbeit. Universität Heidelberg, Heidelberg. Institut für Umweltphysik Heidelberg.

Rädle, Viola; Kersting, A.; Schmidt, Maximilian; Ringena, Lisa; Robertz, Julian; Aeschbach, Werner et al. (2021): Multi-Tracer Groundwater Dating in Southern Oman by Bayesian Modelling (Paper draft). submitted to Water Resources Research. In *Preprint*.

Ringena, Lisa (2021): Demonstration of a Dual Atom Trap Trace Analysis Setup for 39Ar and 85Kr. Doktorarbeit. Universität Heidelberg, Heidelberg. Kirchhoff Institut für Physik.

Ritterbusch, F. (2013): Dating of groundwater with Atom Trap Trace Analysis of 39Ar. Doktorarbeit. Universität Heidelberg, Heidelberg. Kirchhoff Institut für Physik Heidelberg.

Ritterbusch, F.; Ebser, S.; Welte, J.; Reichel, T.; Kersting, A.; Purtschert, R. et al. (2014): Groundwater dating with Atom Trap Trace Analysis of 39 Ar. In *Geophys. Res. Lett.* 41 (19), pp. 6758–6764. DOI: 10.1002/2014GL061120.

Ross, Kelly Ann; Gashugi, Elisée; Gafasi, Augustin; Wüest, Alfred; Schmid, Martin (2015): Characterisation of the subaquatic groundwater discharge that maintains the permanent stratification within Lake Kivu; East Africa. In *PloS one* 10 (3), e0121217. DOI: 10.1371/journal.pone.0121217.

Ross, Kelly Ann; Smets, Benoît; Batist, Marc de; Hilbe, Michael; Schmid, Martin; Anselmetti, Flavio S. (2014): Lake-level rise in the late Pleistocene and active subaquatic volcanism since the Holocene in Lake Kivu, East African Rift. In *Geomorphology* 221, pp. 274–285. DOI: 10.1016/j.geomorph.2014.05.010.

Roth, Kurt (2016): Fundamentals of Environmental Physics. Lecture Notes. v0.4-p.

Sahama, G. (1972): Evolution of the Nyiragongo Magma. In *Journal of Petrology* (14), pp. 33–48.

110

Sander, R. (2015): Compilation of Henry's law constants (version 4.0) for water as solvent. In *Atmos. Chem. Phys.* 15 (8), pp. 4399–4981. DOI: 10.5194/acp-15-4399-2015.

Schmid, M.; Bärenbold, F.; Boehrer, Bertram; Darchambeau, François; Grilli, Roberto; Triest, T.; Tümpling, Wolf von (2019): Intercalibration Campaign for Gas Concentration Measurements in Lake Kivu.

Schmid, Martin; Halbwachs, Michel; Wehrli, Bernhard; Wüest, Alfred (2005): Weak mixing in Lake Kivu: New insights indicate increasing risk of uncontrolled gas eruption. In *Geochem. Geophys. Geosyst.* 6 (7), n/a-n/a. DOI: 10.1029/2004GC000892.

Scholes, Colin (2018): Water Resistant Composite Membranes for Carbon Dioxide Separation from Methane. In *Applied Sciences* 8 (5), p. 829. DOI: 10.3390/app8050829.

Sprenger, Matthias; Stumpp, Christine; Weiler, Markus; Aeschbach, Werner; Allen, Scott T.; Benettin, Paolo et al. (2019): The Demographics of Water: A Review of Water Ages in the Critical Zone. In *Rev. Geophys.* 57 (3), pp. 800–834. DOI: 10.1029/2018RG000633.

Šrámek, Ondřej; Stevens, Lauren; McDonough, William F.; Mukhopadhyay, Sujoy; Peterson, R. J. (2017): Subterranean production of neutrons, 39Ar and 21Ne: Rates and uncertainties. In *Geochimica et Cosmochimica Acta* 196, pp. 370–387. DOI: 10.1016/j.gca.2016.09.040.

Stuart, Finlay M.; Mark, Darren F.; Gandanger, Pierre; McConville, Paul (2016): Earth-atmosphere evolution based on new determination of Devonian atmosphere Ar isotopic composition. In *Earth and Planetary Science Letters* 446, pp. 21–26. DOI: 10.1016/j.epsl.2016.04.012.

Sturchio, N. C.; Du, X.; Purtschert, R.; Lehmann, B. E.; Sultan, M.; Patterson, L. J. et al. (2004): One million year old groundwater in the Sahara revealed by krypton-81 and chlorine-36. In *Geophys. Res. Lett.* 31 (5), n/a-n/a. DOI: 10.1029/2003GL019234.

Symbion (2021): Current Projects - KP1 - Kivu56. Edited by Symbion. Available online at http://www.symbion-power.com/current-projects/.

Tassi, F.; Vaselli, O.; Tedesco, D.; Montegrossi, G.; Darrah, T.; Cuoco, E. et al. (2009): Water and gas chemistry at Lake Kivu (DRC): Geochemical evidence of vertical and horizontal heterogeneities in a multibasin structure. In *Geochem. Geophys. Geosyst.* 10 (2), n/a-n/a. DOI: 10.1029/2008GC002191.

Tedesco, D.; Vaselli, O.; Papale, P.; Carn, S. A.; Voltaggio, M.; Sawyer, G. M. et al. (2007): January 2002 volcano-tectonic eruption of Nyiragongo volcano, Democratic Republic of Congo. In *J. Geophys. Res.* 112 (B9). DOI: 10.1029/2006JB004762.

Tong, Amin L.; Gu, Ji-Qiang; Yang, Guo-Min; Hu, Shui-Ming; Jiang, Wei; Lu, Zheng-Tian; Ritterbusch, Florian (2021): An atom trap system for 39Ar dating with improved precision. In *The Review of scientific instruments* 92 (6), p. 63204. DOI: 10.1063/5.0050620.

Um, Sukkee; Wang, C.-Y.; Chen, K. S. (2000): Computational Fluid Dynamics Modeling of Proton Exchange Membrane Fuel Cells. In *J. Electrochem. Soc.* 147 (12), p. 4485. DOI: 10.1149/1.1394090.

Visser, Ate; Broers, Hans Peter; Purtschert, Roland; Sültenfuß, Jürgen; Jonge, Martin de (2013): Groundwater age distributions at a public drinking water supply well field derived from multiple age tracers (85 Kr, 3 H/ 3 He, and 39 Ar). In *Water Resour. Res.* 49 (11), pp. 7778–7796. DOI: 10.1002/2013WR014012.

Wang, J. S.; Ritterbusch, F.; Dong, X-Z; Gao, C.; Li, H.; Jiang, W. et al. (2021): Optical Excitation and Trapping of ^{81}Kr. In *Physical review letters* 127 (2), p. 23201. DOI: 10.1103/PhysRevLett.127.023201.

Welte, Joachim (2011): Atom Trap Trace Analysis of 39Ar. Doktorarbeit. Universität Heidelberg, Heidelberg. Kirchhoff Institut für Physik Heidelberg.

Wijmans, J. G.; Baker, R. W. (1995): The solution-diffusion model: a review. In *Journal of Membrane Science* (107).

Williams, R. W.; Gill, J. B. (1992): TH isotope and Useries disequilibria in some alkali basalts. In *GEOPHYSICAL RESEARCH LETTERS* 19 (2), pp. 139–142.

Worldbank (2021): Population growth (annual %) - Oman. Edited by Worldbank. Available online at https://data.worldbank.org/indicator/SP.POP.GROW?locations=OM, checked on 8/22/2021.

Yechieli, Yoseph; Yokochi, Reika; Zilberbrand, Michael; Lu, Zheng-Tian; Purtschert, Roland; Sueltenfuss, Jürgen et al. (2019): Recent seawater intrusion into deep aquifer determined by the radioactive noble-gas isotopes 81Kr and 39Ar. In *Earth and Planetary Science Letters* 507, pp. 21–29. DOI: 10.1016/j.epsl.2018.11.028.

Yokochi, R.; Sturchio, N. C.; Purtschert, R.; Jiang, W.; Lu, Z.-T.; Mueller, P. et al. (2013): Noble gas radionuclides in Yellowstone geothermal gas emissions: A reconnaissance. In *Chemical Geology* 339, pp. 43–51. DOI: 10.1016/j.chemgeo.2012.09.037.

Yokochi, Reika; Sturchio, Neil C.; Purtschert, Roland (2012): Determination of crustal fluid residence times using nucleogenic 39Ar. In *Geochimica et Cosmochimica Acta* 88, pp. 19–26.

Zhang, Hong; Weber, Stephen G. (2012): Teflon AF Materials. In *Topics in current chemistry* 308, pp. 307–337. DOI: 10.1007/128_2011_249.

# 11.	Acknowledgements

The last four and a half years were an amazing time full of curiosity, adventure and wonder and it is due to an amazing group of people that I could finish this work. I want to express my deep gratitude for this support.

First of all, I have to thank my supervisors Werner Aeschbach and Markus Oberthaler. They were not only supervisors, but also mentors and sources of great support. Thank you for your trust and for creating an environment in which I could be sure of your constant backing, especially during the hard times a PhD can bring along.

Werner, thank you for introducing me to the fascinating world of hydrogeology. During my time in your group, I was able to get a deeper understanding of the interconnections that are ubiquitous in environmental systems. Your trust in me, letting me plan and execute those trips to Lake Kivu, was exceptional.

Markus, thank you for showing me the huge and amazing world of atom optics. The amount of skills I learned while caring for our beloved ATTA machine is vast. Thank you for your constant availability and your support in all our troubles.

I also want to thank Prof. André Butz for generously offering his valuable time for reviewing my thesis.

All of the work and notably the life in the lab and in the field could not have been possible without the fantastic crew of my dear PhD companions, to whom I am deeply grateful. Lisa and Julian, working and living with you made the daily struggle in the ATTA lab so much more bearable and more often than not a real pleasure. David, our trip to Rwanda was amazing and you were a great travel companion. Yannis, your easygoing attitude and your perfectly prepared samples were always highly appreciated.

Big thanks go out to my former colleagues as well. Arne, thank you for introducing me to field work and the IUP labs. Zhongyi, thank you for your tutoring even when you had to explain the lock in amplifiers for the third time or more. Sven, the things I learned while seeing you work on the ocean campaign were priceless and accompanied me all the way.

A certain consistency is necessary for the success of all the experiments in the matterwave group. This consistency is certainly due in great part to Helmut Strobl. Helmut, thank you so much for always being there and for your perseverance whenever lab equipment challenged us.

I was lucky to be connected with some great collaboration partners, which enabled me to unite so many different disciplines in this project. Bertram, thank you so much for your support and your interest in my work. Your expertise and your open ear really helped me to get a deeper understanding for Lake Kivu. Martin, I highly appreciated your scientific and logistic support in both the Lake Kivu trips. Without your expertise and your openness to welcome me in this endeavor, my work could not have been the same. Fabian, master of Simstrat! Our joined work on Lake Kivu was a great